CALCULATION OF BETA-DECAY RATES IN HEAVY DEFORMED NUCLEI
AND IMPLICATIONS FOR THE ASTROPHYSICAL r PROCESS

Thomas R. Shafer

A dissertation submitted to the faculty at the University of North Carolina at Chapel Hill in partial
fulfillment of the requirements for the degree of Doctor of Philosophy in the Department of Physics and
Astronomy.

Chapel Hill
2016

Approved by:

Jonathan Engel

Charles Evans

Carla Fröhlich

Christian Iliadis

John Wilkerson

ABSTRACT

Thomas R. Shafer: Calculation of Beta-decay Rates in Heavy Deformed Nuclei
and Implications for the Astrophysical r Process
(Under the direction of Jonathan Engel)

The rapid neutron-capture process (r process) is responsible for synthesizing approximately half of the heavy elements in the solar system, but after decades of work the astrophysical site where it occurs is unknown. Because a very large number of heavy, neutron-rich nuclei are populated during the r process, theoretical efforts to locate the r-process site require a tremendous amount of nuclear physics input. However, most nuclei populated during the r process are very neutron-rich and unstable, and many r-process nuclei cannot be studied experimentally. As a result, the basic properties of a large number of heavy, deformed, short-lived nuclei must be calculated with reliable nuclear models.

β-decay half-lives are among the most important properties that affect r-process abundances. In this work we present a new, efficient method for calculating β-decay half-lives of heavy, deformed nuclei: the proton-neutron finite amplitude method (pnFAM). We apply the pnFAM to calculate half-lives of nuclei that demonstrate the strongest effects on r-process abundances in the $A \simeq 80$ and $A \simeq 160$ mass regions, including even-even, odd-A, and odd-odd nuclei. We find that our calculations result in half-lives very similar to those reported in previous studies, with correspondingly small effects on r-process abundances.

For Martha,
Mom, & Dad.

ACKNOWLEDGEMENTS

TABLE OF CONTENTS

LIST OF TABLES

LIST OF FIGURES

LIST OF ABBREVIATIONS AND SYMBOLS

A Number of nucleons in the nucleus

DFT   Density functional theory

EDF   Energy-density functional

EFA   Equal-filling approximation

FAM   Finite amplitude method

HFB   Hartree-Fock-Bogoliubov

N Number of neutrons in the nucleus

pnFAM   Proton-neutron finite amplitude method

QRPA   Quasiparticle random-phase approximation

REE   Rare-earth element

RPA   Random-phase approximation

TDDFT   Time-dependent density functional theory

TDHFB   Time-dependent Hartree-Fock-Bogoliubov

Z Number of protons in the nucleus

CHAPTER 1:   INTRODUCTION AND MOTIVATION

Nucleosynthesis, the set of processes responsible for forming the atomic nuclei in matter, is a fundamentally important research area; it has also proven tremendously challenging to understand in full. Because nucleosynthesis occurs in and near stars, its study is interdisciplinary: beginning with the seminal work of Burbidge *et al.* [1] and Cameron [2] nearly sixty years ago, efforts to understand these stellar processes have required both nuclear physics and astrophysics—theoretical calculations alongside laboratory experimentation and astronomical observation.

Among the processes required to produce the elements in nature [1, 2], those responsible for nuclei heavier than iron have proven especially challenging to unravel. In this work we provide new nuclear physics calculations—β-decay half-lives of heavy, deformed, neutron-rich nuclei—in an effort to better understand the astrophysical origins of these heavy elements. In particular, we examine nucleosynthesis via the rapid neutron-capture process (r process), which forms approximately half of the nuclei heavier than iron (see, e.g., the reviews [3–5]). In this introductory chapter we summarize the basics of r-process nucleosynthesis and the importance of improved β-decay half-lives (and improved nuclear physics input in general) to theoretical r-process studies.

Section 1.1:   The origin of the heavy elements

Since the 1950s [1, 2] it has been understood that nuclei are formed in and near stars by a variety of processes. This nuclear material can subsequently be expelled in a variety of catastrophic processes including supernovae [2]. However, even the most massive stars can only produce nuclei as heavy as Fe (with $Z = 26$ protons) in their cores; the formation of heavier nuclei is prohibited by both nuclear and astrophysical considerations (see Ref. [3] and references therein). The bulk of the nuclear material (and there are of course many nuclei heavier than Fe, cf. Fig. 1.1) must be made by other means.

The early work of Burbidge *et al.* [1] and Cameron [2] identified two main processes for nucleosynthesis beyond Fe: the slow neutron-capture process (s process) and the rapid neutron-capture process (r process). Beside these two n-capture processes, which make up essentially 100% of the nuclei heavier than Fe [4], a third process, the p process (see, e.g., the review [7]), forms relatively proton-rich nuclei via proton capture that cannot be made in the other processes. (There are also further proton-capture processes; for example, the rp process [8].) More recently, an additional "light element primary process" (LEPP) [9] has been suggested,
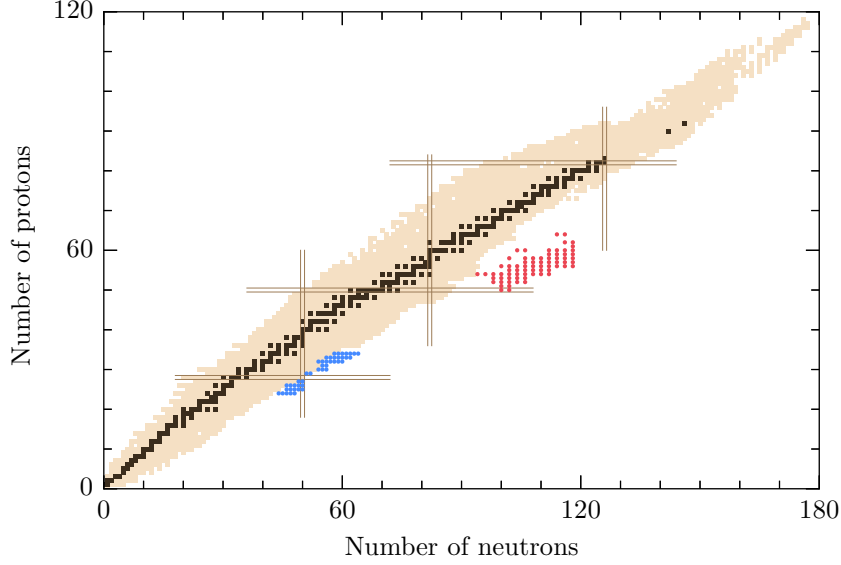
Figure 1.1: The nuclear landscape. Nuclei with experimentally-measured half-lives are shaded light, and "stable" nuclei with half-lives $T_{1/2} > 109$ yr are shaded dark. The $N = 50, 82$, and 126 and $Z = 28, 50$, and 82 shell closures are marked with solid lines. The r-process nuclei with $A \simeq 80$ (blue circles) and $A \simeq 160$ (red circles) studied in this work are also highlighted past the neutron-rich edge of the experimental measurements. The experimental data are from NUBASE2012 [6].

and another new process, the νp process [10–12] (which leverages the large neutrino fluxes in core-collapse supernovae (CCSNe) to create additional neutrons), has been introduced and suggested to be a candidate LEPP. These new processes do not change the overall picture of abundances dominated by neutron capture.

Focusing on the n-capture processes specifically, the s process (which operates through neutron capture that occurs less frequently than β decay, on a time scale of 10–100 years [2]) forms neutron-rich nuclei near the valley of β stability. The r process operates on much shorter time scales ($\tau \sim 1$ s) and is necessary for producing heavier neutron-rich nuclei that cannot be made in the s process [1, 2]. Many nuclei can of course be formed in varying proportions by both processes (see Ref. [13] and references therein), though a few elements are understood to be nearly pure s- or r-elements (e.g., Eu is an r-element [14]).

The s process is the better understood n-capture process (see the review [15] as well as Ref. [3] and references therein), and calculated s-process abundances (e.g., Ref. [14]) are typically used to obtain r-process residuals via "solar minus s-process" calculations [16, 17] (also see Refs. [3, 4, 13] and references therein). The r process, on the other hand, has many important questions still unanswered [4], not the least of which is its astrophysical site.

Section 1.2: The r process

The basic r-process mechanism was initially described in detail by Burbidge *et al.* [1] and also by Cameron [2], occurring in regions with both a large neutron fluxes and high temperatures $T \sim 10$ GK. In this

"canonical" or "hot" r process (described in many places, see, e.g., Refs. [3, 4, 18]), neutron capture takes place on very short time scales, much shorter than β decay (usually written $\tau_n \ll \tau_\beta$), as a result of the large number of free neutrons. Lighter seed nuclei (e.g., Fe isotopes) that are produced during the r process and then exposed to this neutron flux will quickly capture neutrons and form extremely neutron-rich isotopes.

Depending on the conditions, these heavy isotopes may be so neutron-rich as to approach the neutron drip line (at which point no additional neutrons may be bound to the nucleus). At the high temperatures described in Ref. [1], however, the r process can reach a statistical equilibrium between neutron capture and its reverse reaction, photo-dissociation. This $(n, \gamma) \rightleftarrows (\gamma, n)$ equilibrium ensures that somewhat lighter nuclei are populated instead, as high-energy photons remove the most weakly-bound neutrons from the most neutron-rich isotopes.

After a long time relative to the n-capture time scale τ_n, the r process will have formed many neutron-rich, β-unstable isotopes. Eventually (on the β-decay time scale, $\sim$ 1–1000 ms) these unstable isotopes will begin to decay, gaining relative stability by moving towards the valley of β stability by one unit: $(Z, N) \rightarrow (Z+1, N-1)$. The decay products will then repeat the capture-and-decay process as long as free neutrons are still available. In this way the r process forms very short-lived, neutron-rich isotopes of the heavy elements ($Z \gg 26$) very quickly, over just a few seconds. The most neutron-rich scenarios (for example, that of a neutron star merger [4]) can form such heavy nuclei that fission plays a role as well. This can lead to fission cycling, in which fission products themselves experience the r process, perhaps eventually leading to additional fissions.

Eventually, the r process begins to wind down as neutron capture and photo-dissociation fall out of equilibrium [18]. As this happens, β decay begins to take place on approximately the same time scale as (or faster than) neutron capture and photo-dissociation—the latter processes occur less frequently either due to lack of neutrons or lowered temperatures [19]. The β-unstable material formed during the $(n, \gamma) \rightleftarrows (\gamma, n)$ equilibrium then decays towards stability, and β decay competes with neutron capture and photo-dissociation for some time. This competition can affect final abundance patterns before n-capture and photo-dissociation freeze out completely, leaving the material to β decay to stability (see, e.g., Ref. [20]).

We have sketched the basics here, but the full r-process picture seems more complex than only the "canonical" one. For example, the $(n, \gamma) \rightleftarrows (\gamma, n)$ equilibrium proposed in Refs. [1, 2] need not exist: Wanajo [21] introduced a relatively low-temperature condition in which the (γ, n) reactions do not play a serious role (the "cold" r process). Neutron star mergers (NSMs) are candidate r-process sites that similarly do not demonstrate such high temperatures (see Ref. [4] and references therein). In these lower-temperature cases the r process populates neutron-rich nuclei closer to the drip line.

1.2.1: Abundance features

The fast neutron capture described above is responsible for the hallmark r-process abundance features: sizable increases in the amounts of nuclear material with the mass numbers $A = 80$, 130, and 195 [1, 2]. These features are important as an r-process signature, and theoretical calculations must be able to reproduce them.

The large abundances at these mass numbers are explained by filled neutron shells in a nuclear shell model, corresponding to the "magic" numbers $N = 50$, 82, and 126 [22] (also see Refs. [1, 2] and additional references therein). Closed neutron shells have reduced n-capture cross-sections, and, if captured, an additional neutron is not very bound [22]. These nuclei also tend to have long β-decay half-lives [18] and are often called r-process "waiting points." As nuclear material moves up the nuclear chart to larger values of Z during the r process, reduced n-capture cross-sections for closed-shell nuclei act to trap nuclear material. (In fact the s process forms similar features at the slightly larger mass numbers $A \simeq 90$, 138, and 208 [1, 2].) These abundance peaks are formed during the main phase of the r process, i.e., during the $(n, \gamma) \rightleftarrows (\gamma, n)$ equilibrium if one persists.

In addition to the three primary r-process abundance peaks, there is also a fourth, somewhat smaller, peak in the region of the rare-earth elements (REEs) with $A \simeq 165$. Understanding the formation of this REE abundance peak has been a challenge, as summarized in Refs. [18, 19] and references therein: Burbidge *et al.* [1] suggested the REE peak was formed during the r process as a consequence of nuclear deformation; and Cameron [2] hypothesized it was due to fission, though this was later deemed unlikely [23]. (Fission seems to have re-emerged as a potential driver [24] of, or at least as a contributor [19] to, the REE peak.)

Surman and Engel [18] demonstrated nicely that the REE peak is, in fact, caused by a local maximum in the nuclear shape deformation, but not during the main phase of the r process. Rather, at least for a hot r process, the peak is only formed at late times after neutron capture and photo-dissociation have fallen out of equilibrium; changes in nuclear shape deformation weakly mimic a shell closure. Refs. [19, 20] also found this effect, and Ref. [20] further demonstrated that the REE peak could also be formed during a cold r process without a prolonged $(n, \gamma) \rightleftarrows (\gamma, n)$ equilibrium, albeit via a slightly different mechanism. Because of the unique dynamics that govern the formation of the REE peak, its formation can provide additional insight into the r process [19, 20].

1.2.2: The search for the r-process site

Even after sixty years, the identification of an r-process site producing the abundances described above has not been accomplished. As discussed in the review [4], the challenge of identifying the r-process site is immense: the effort requires both nuclear physics and astrophysics, but the contributions from both fields still contain large uncertainties.

The uncertainties in nuclear physics input stem from both the neutron richness of the nuclei involved in the r process and the sheer number of nuclei that are involved to make the heavy elements. Because the r process forms so many nuclei, accurate and precise abundance calculations for different astrophysical sites require nuclear physics input for a tremendous number of nuclei including masses, reaction rates, and fission barriers [25] (see also a summary in Ref. [4]). The neutron-richness of r-process nuclei also means that few-to-none of these key properties can be measured in current-generation experiments for the most neutron-rich nuclei [4].

As a result, astrophysical calculations must rely on nuclear physics input derived from separate nuclear physics calculations. These calculations of nuclear properties have their own uncertainties that are potentially compounded by extrapolation to regions of high neutron-excess (see Ref. [3] and references therein). Recent work by Mumpower and collaborators has demonstrated that typical uncertainties in nuclear masses [25] as well as neutron-capture and β-decay rates [26] remain a serious hindrance to precise predictions of r-process abundances (see also Ref. [27] and references therein).

Setting aside the nuclear physics component, the astrophysical picture is even less clear [4]. It now seems likely that there is a distinction between r-process scenarios that form the elements above and below $A \simeq 140$ [28], and these processes have been named the "main" and "weak" r processes, respectively. This classification may not be set in stone (see, e.g., the reviews [5, 13] and references therein), but is supported by (1) the "robust" nature of observed main r-process abundances and (2) the scatter in weak r-process abundances (see, e.g., the reviews [5, 13, 29–31]). It has also been demonstrated over time that observational data can described by a phenomenological two- or three-component r-process model [32–39].

However, the challenge of identifying the astrophysical sites corresponding to the weak and main r process remains. The neutrino-driven wind (NDW) of a core-collapse supernova has long been investigated as a potential r-process site, but modeling these supernovae is extremely complicated (see, e.g., the review [40]). As increasingly-sophisticated models become available, the NDW no longer appears to be a strong candidate for a main r process and in fact seems more likely to be proton-rich than neutron-rich (see, e.g., the recent review [31] and references therein).

On the other hand, neutron star mergers remain intriguing candidates for a main r process. Despite concerns regarding the compatibility of NSMs with observations in metal-poor stars [41], r-process calculations with NSMs seem extremely robust (e.g., Refs. [24, 42–44]) in their production of realistic abundances for the main r process, including the REE peak. Very recent measurements of ^{244}Pu seem to strongly support neutron star mergers as an r-process source and also to exclude core-collapse supernovae [45]. Thielemann has subsequently suggested that neutron star mergers are "probably a dominant event in recent galactic history," [46] though perhaps magnetorotational core-collapse supernovae [47, 48] may need to be included in

the picture to explain early r-process abundances.

Indeed, many astrophysical scenarios still seem possible. Combinations of core-collapse supernovae, magnetorotational core-collapse supernovae, and neutron star mergers can produce solar abundances [49]; neutron star mergers and magnetorotational supernovae can similarly describe galactic Eu abundances [50]; and perhaps magnetorotational core-collapse supernovae can explain both the main and weak r processes [48]. Disentangling this knot will clearly require the continued effort of astrophysics and nuclear physics working in concert.

Section 1.3:   The importance of β decay in r-process calculations

As discussed above, r-process studies require a tremendous amount of nuclear physics input, and many different nuclear inputs play a role. β decay in particular plays a key role by determining (1) how quickly nuclear material moves through the waiting points and (2) final abundances distributions as material decays back towards stability. This second effect has been shown to be particularly important in the formation of the REE abundance peak, where the interplay of β decay and neutron capture after the $(n, \gamma) \rightleftarrows (\gamma, n)$ equilibrium has ended builds up the peak [18, 20]. This suggests that accurate modeling of β decay is particularly important for rare-earth nuclei, although recent neutron star merger calculations indicate the REE peak is actually quite robust for different β-decay half-life calculations [42].

As with other critical r-process inputs, it is important to improve our understanding of the β decay of neutron-rich nuclei. The uncertainties present in typical calculations remain large enough to seriously affect resulting uncertainties in r-process calculations [26, 27], and as the reach of β-decay experiments has increased it has been found that many theoretical calculations predict too-long β-decay half-lives for nuclei near closed shells. Changes in these half-lives modify computed r-process abundances (see, e.g., Refs. [51–53] and references therein). For example, speeding up β-decay half-lives near $N = 126$ has been shown to affect the $A = 195$ r-process peak in neutron star merger calculations and bring calculations closer to solar observations [24], and Eichler *et al.* [53] have found similar effects when increasing β-decay rates for nuclei with $Z > 80$. Caballero *et al.* [51] have also studied the effect of reduced β-decay half-lives near magic numbers, while Madurga *et al.* [54] have measured shorter half-lives for Zn and Ga isotopes than those predicted by Möller *et al* [55] and produced new calculations that yield significant effects on r-process abundances for nuclei heavier than $A = 140$.

Perhaps the standard set of β-decay half-lives in use today is that of Möller *et al.* [55] from more than a decade ago, while the REACLIB database[1] [56] still includes β-decay half-lives that are thirty years old [57]. In addition to many recent smaller-scale β-decay calculations, however, new large-scale calculations are

---

[1]`https://groups.nscl.msu.edu/jina/reaclib/db/`

beginning to become available: Marketin *et al.* [58, 59] have recently computed the half-lives of more than 5,400 neutron-rich nuclei (although these calculations do not treat nuclear shape deformation), and Mustonen and Engel [60] have computed half-lives of nearly 1,400 even-even nuclei using the method detailed and applied in following chapters.

In this work we present new β-decay half-lives in both the REE peak region ($A \simeq 165$) and the weak r-process region ($A \simeq 80$), shown in Fig. 1.1. Our calculations are both self-consistent (ground states and β transitions are calculated with the same nuclear interaction) and microscopic (nucleons are the only degrees of freedom). The microscopic nature of these calculations is important to increase confidence in predictions for very neutron-rich nuclei (see, e.g., the discussion in Ref. [4]). Our calculations incorporate both pairing correlations and nuclear shape deformation, but our method (called the proton neutron finite amplitude method, or pnFAM [61]) remains efficient enough to allow β-decay calculations across the entire nuclear chart as presented in Ref. [60].

We have calculated rare-earth β-decay half-lives to (1) compare our new calculations to the standard ones of Möller *et al.* [55] and (2) examine the consequences for the r process in the REE peak region. The overall speed of β decays in the rare-earth region, for example, can determine the overall abundance in the rare-earth peak [62]. Unlike the REE peak, $A \simeq 80$ abundances appear to be formed by a variety of processes (see, e.g., Refs. [5, 31] and references therein). With the new calculations presented here, we examine the impact of β-decay half-lives on r-process calculations in this lighter mass region. In this way we hope to shed light on the r-process contribution to these abundances.

In this work we also present an extension of the pnFAM that enables the calculation of β-decay half-lives for both singly and doubly odd nuclei (when referring to both classes collectively, we simply call them 'odd' nuclei). This extension is incorporated into both our $A \simeq 165$ and $A \simeq 80$ calculations, and will allow the inclusion of odd nuclei in future microscopic calculations across the nuclear chart without serious difficulty.

1.3.1: Outline of this work

This dissertation is organized as follows: We begin with an overview of β decay and our treatment in Chapter 2 (with further details in Appendix A) as well as nuclear shape deformation in Chapter 3 (again, with more details in Appendix B). In Chapter 4 we review density functional theory and linear response theory, the foundations of our method. Then in Chapters 5 and 6 we describe the pnFAM, including our recent extension to odd nuclei. Additional details of the derivation are presented in Appendix C. Finally, we describe our calculations in the REE and $A \simeq 80$ regions in detail in Chapters 7 and 8. We conclude with a brief discussion in Chapter 9.

CHAPTER 2: β DECAY IN NUCLEI

In this chapter we briefly review nuclear β decay and demonstrate how we calculate half-lives (or, equivalently, decay rates) from nuclear matrix elements of the weak interaction. β decay is unique among typical nuclear radiation (α, β, and γ), a product of the weak nuclear force [63], and provided the first demonstration of a fundamental interaction that does not exhibit mirror (or, parity) symmetry. Besides the obvious applications of β decay to nuclear radioactivity, its discovery also led to the proposition and subsequent discovery of the (nearly) massless neutrino [63, 64] which remains the subject of large-scale experimental efforts.

The simplest example of β decay is that of a free neutron [63–65], with a half-life of approximately 10 minutes [66], in which the neutron decays into a proton, electron, and antineutrino (β^- decay):

$$n \to p + e^- + \bar{\nu}_e. \tag{2.1}$$

The decay is energetically possible since the neutron is more massive than the proton-electron-neutrino combination by approximately 782 keV/c^2 [66]. Alongside β^- decay are two related β-decay processes: proton decay (β^+ decay)

$$p \to n + e^+ + \nu_e, \tag{2.2}$$

and electron capture

$$e^- + p \to n + \nu_e. \tag{2.3}$$

Neither of the decays (2.2) or (2.3) are allowed for free particles at rest since the proton mass (and the combined mass of the proton and electron in Eq. (2.3)) is less than that of the neutron. Inside the nucleus, however, the interactions among the nucleons that make up the nuclear binding energy significantly affect the stability of the constituent nucleons. These interactions allow nuclear β^+ decay and electron capture to occur in some cases and significantly affect β-decay half-lives in general. In many nuclei near the "valley of stability" (dark shaded squares in Fig. 1.1), for example, β^- decay is either energetically impossible [63] or strongly suppressed. In regions with large neutron excesses (as in r-process nuclei), the nuclear half-life may fall well below that of the free neutron, into the millisecond range. And on the proton-rich side of the β-stability valley, nuclear β^+ decay becomes possible as the number of protons increases. We focus on β^-

decay in this work since the r-process abundances of interest depend on the half-lives of neutron rich nuclei.

The nuclear equivalent of the β decay of a free neutron (2.1) is the process

$$(Z, N) \rightarrow (Z + 1, N - 1) + e^- + \bar{\nu}_e, \tag{2.4}$$

i.e. one of the N neutrons in the nucleus decays, resulting in a nucleus with $Z+1$ protons and $N-1$ neutrons. The energy balance in the β-decay process (2.4) is written[1] [64]

$$M_i(Z, N) = M_f(Z + 1, N - 1) + m_e + Q, \tag{2.5}$$

where M_i and M_f are the initial and final nuclear masses, and m_e is the electron mass. In the limit of very large initial and final nuclear masses and zero neutrino mass (both very good approximations in β decay [65]), the Q value is the kinetic given to the emitted leptons [64]. Values for $M(Z, N)$ must either be taken from experiment or calculated. Calculations must account for both the masses of the nucleons themselves and the nuclear binding energy.

For decays to the ground state of the daughter (final) nucleus, the Q value is given the symbol Q_β. To calculate the total β-decay half-life we must also account for decays to all the energetically allowed excited states in the daughter nucleus. These states have excitation energies E_x with respect to the ground state of the daughter, and the Q values for these decays are smaller than Q_β by the excitation energy [64]:

$$Q_x = Q_\beta - E_x. \tag{2.6}$$

Section 2.1:   Allowed and forbidden β decay

Nuclear β decay is often described as being either "allowed" or "forbidden," with these classifications being named according to the relative rarity of decay—forbidden decays occur much less often than allowed decays. This classification arises naturally from the matrix elements of the weak nuclear interaction, which can be demonstrated by considering a schematic version of β decay. In this section, we follow the presentation of Refs. [64, 67].

Because the weak nuclear interaction is, in fact, weak compared to the strong nuclear and Coulomb interactions inside the nucleus, a first-order perturbation theory treatment of its effect on the nucleus is acceptable and results in Fermi's "golden rule" [63, 64, 67] for the decay rate λ (the probability of a nucleus

---

[1]Following Ref. [65], in this chapter we mostly use "natural" units where $\hbar = c = m_e = 1$.

to decay per unit time [63]):

$$\lambda = \frac{2\pi}{\hbar} \left| M_{fi} \right|^2 \rho(E_f). \tag{2.7}$$

The decay rate is inversely related to the half-life: $\lambda = \ln 2/T_{1/2}$. Up to some constants, the decay rate is the product of (1) the square of a matrix element M_{fi}, which describes the β-decay the nucleus, and (2) a phase space factor $\rho(E_f)$, which counts the number of final states the emitted leptons can decay into as a function of their total energy E_f.

The matrix element M_{fi} is the amplitude for a nucleus in the state $|i\rangle$ to β decay to the daughter state $|f\rangle$ as in Eq. (2.5) and can be written approximately as [64, 67]

$$M_{fi} = \int \Psi_f^*(\mathbf{r}) \, \varphi_e^*(\mathbf{r}) \, \varphi_\nu^*(\mathbf{r}) \, \hat{V}(\mathbf{r}) \, \Psi_i(\mathbf{r}) \, \mathrm{d}^3\mathbf{r}, \tag{2.8}$$

where Ψ_i and Ψ_f are the initial- and final-state nucleon wave functions. The emitted leptons are described by plane waves:[2]

$$\varphi_e(\mathbf{r})\varphi_\nu(\mathbf{r}) \propto e^{i\mathbf{q}\cdot\mathbf{r}}, \tag{2.9}$$

with $\mathbf{q} \equiv \mathbf{p}_e + \mathbf{p}_\nu$ their total momentum. The overlap of the lepton wave functions with the nucleus is quite small [64]—the nuclear radius is typically approximated by $R \approx 1.2A^{1/3}$ fm [67], so $R \approx 5.6$ fm when $A = 100$. As a result, a $Q = 1$ MeV decay gives $qR \approx 0.04$, and a 10 MeV decay has $qR \approx 0.3$. Expanding the lepton wave functions in powers of $\mathbf{q} \cdot \mathbf{r}$ gives a series of matrix elements,

$$\begin{aligned} M_{fi} &= \int \Psi_f^*(\mathbf{r}) \left[1 - i\mathbf{q} \cdot \mathbf{r} - \ldots \right] \hat{V}_{\mathrm{weak}}(\mathbf{r}) \, \Psi_i^*(\mathbf{r}) \, \mathrm{d}\mathbf{r} \\ &= M_{fi}^{\mathrm{a}} + M_{fi}^{\mathrm{ff}} + \ldots, \end{aligned} \tag{2.10}$$

that involve only the nuclear wave functions, the weak interaction, and powers of $\mathbf{q} \cdot \mathbf{r}$. Since the decay rate depends on M^2, the contribution of the second term in Eq. (2.10) is reduced by a factor between 10 and 1000 (approximately) relative to the first, all else being equal. The first term describes allowed decays, and the second describes "first-forbidden" decays.

In allowed β decay the leptons are emitted without orbital angular momentum, and the parity of the daughter nucleus is the same as the parent ($\pi_i = \pi_f$, or $\pi = +1$) [64]. Despite not possessing orbital angular momentum, the leptons may still carry nonzero *total* angular momentum J depending on whether the lepton spins are anti-aligned ($J = 0$) or aligned ($J = 1$). Allowed transitions must correspondingly change the

---

[2]In a rigorous derivation the emitted leptons must be treated relativistically since $m_\nu \approx 0$. Even in a decay with $Q = 1$ MeV the emitted electron may have velocities as large as $v = p/E \approx 0.9c$ [68, 69].

angular momentum of the nucleus by zero or one unit to conserve angular momentum—"Fermi" transitions do not change the angular momentum of the nucleus ($\Delta J = 0$) or its parity ($\pi = +1$), but their "Gamow-Teller" counterparts can change the total angular momentum by zero or one unit without changing the parity of the nuclear wave function: $\Delta J^\pi = 0^+$ or 1^+.

First-forbidden decays are more complicated, but they follow the general rules outlined above. The lepton spins still either align or anti-align, but in these decays the leptons carry off $L = 1$ unit of angular momentum as well, changing the parity of the nuclear wave function. The total angular momentum carried by the leptons is then the vector sum of their spin angular momentum ($S = 0$ or 1) and orbital angular momentum ($L = 1$), and it can take the values $J^\pi = 0^-$, 1^-, or 2^-.

If we continued with this expansion, each additional term would be reduced in magnitude by approximately qR, increase the lepton orbital angular momentum by 1 unit, and flip the parity of the nucleus again. Such transitions are called second, third, and fourth forbidden, etc. Since qR is fairly small, the positive-parity allowed transitions will usually provide the dominant contribution to the decay rate. There are regions of the nuclear chart, however, where either qR is not small or the allowed transitions are suppressed enough (e.g., transitions between certain major shells in a nuclear shell model [70]) for first-forbidden decays to be non-negligible. Our r-process calculations involve both moderately neutron-rich ($A \simeq 80$) and very neutron-rich ($A \approx 160$) nuclei, so we include both allowed and first-forbidden decays in our calculations.

Section 2.2:   The total β-decay half-life

In the previous section we sketched how to calculate the β-decay rate for a single transition from parent to daughter nucleus (2.7). The total nuclear β-decay rate, however, must include all energetically-allowed transitions to the daughter. The final states of these transitions, including both the ground state and excited states of the daughter nucleus, may have either positive or negative parity $\pi_f = \pm 1$ and a variety of angular momenta J_f. As a result, the total β-decay rate is not usually composed only from allowed or forbidden transitions, but includes contributions from both types.

The total allowed-plus-first-forbidden β-decay rate for a nucleus with Z protons is calculated by summing over individual contributions and is derived in Ref. [65]:

$$\lambda = \frac{\ln 2}{\kappa} \sum_{J^\pi} \sum_{N_f} \int_1^{W_0(N_f)} C_{J^\pi}(N_f, W_e)\, F(Z+1, W_e)\, p_e W_e (W_0 - W_e)^2 \, \mathrm{d}W_e. \tag{2.11}$$

The constant $\kappa = (6147.0 \pm 2.4)$ s is determined from surveys of superallowed β decays [71], and we adopt the convention of Ref. [65] in which only the constant κ is dimension-full; all quantities in the integral are dimensionless including the momentum $p_e \to p_e/m_e$ and energy $W_e \equiv E_e/m_e$ of the electron. The total rate

(2.11) incorporates both allowed and first-forbidden transitions, with angular momentum and parity J^π, by including all energetically-allowed transitions to final states N_f with angular momentum and parity $J_f^{\pi_f}$ compatible with the initial nucleus and the angular momentum and parity of the decay.

The contribution of individual transitions to final states N_f involve both (1) the shape factor $C_{J^\pi}(N_f, W_e)$ built up from energy-dependent combinations of nuclear matrix elements and (2) factors of the electron energy and momentum weighted by a "Fermi function" $F = F_0 L_0$ that accounts for the effect of the nuclear charge on the emitted electron [64]. The maximum decay energy for each transition is $W_0 = 1 + (Q_\beta - E_{N_f})/m_e$, i.e., only excitations with energies below the Q value are included (cf. Eq. (2.5)).

Detailed expressions for the shape factors C are provided in Appendix A along with definitions of the Fermi and Coulomb functions F_0 and L_0 mentioned above. Most of the remainder of this work describes how we calculate the products of nuclear matrix elements that appear in the shape factors.

CHAPTER 3:   NUCLEAR SHAPE DEFORMATION

As we saw in the previous chapter, β-decay half-life calculations require energy-dependent combinations of nuclear matrix elements. The actual calculation of these matrix elements will be described in Chapters 5 to 8, but first we discuss the connection between our calculations and the properties of real nuclei measured in the laboratory. As discussed in the introduction, r-process nuclei tend to be heavy, neutron-rich, and deformed (non-spherical). It turns out that our calculations break the rotational symmetry of the nuclear Hamiltonian for deformed shapes, and we must (at least approximately) restore this symmetry.

Section 3.1:   Deformation and angular momentum symmetry breaking

The total angular momentum of the nucleus is a conserved quantity [72, 73]—the nuclear Hamiltonian commutes with the total angular momentum operator $\mathbf{J}$, and nuclear stationary states have well-defined total angular momentum J and z-projection M that are constants of the motion. Spherical nuclei are especially simple since they are invariant under rotations. We know, however, that many nuclei do not have spherical shapes; these nuclei possess (at least approximately) the characteristic $J(J+1)$ excitation spectra of a quantum rigid rotator [67, 73–75] described by the Hamiltonian [73]

$$\hat{H}_{\mathrm{rot}} \sim \frac{\hbar^2}{2\mathscr{I}}\mathbf{J}^2. \tag{3.1}$$

The appearance of rotational spectra suggests these nuclei rotate collectively (i.e., all the nucleons in the nucleus rotate together) with total angular momentum J, which is not possible for spherical nuclei (spherical systems do not change under rotation and cannot exhibit collective rotation [74]). This is true even for deformed nuclei with $J = 0$ in their ground states; these nuclei will have excited states with higher values of J and excitation energies derived from Eq. (3.1).

Because a deformed nucleus does not have spherical symmetry, we can define a new coordinate system attached to the nucleus, the "intrinsic" coordinate frame. Our calculations, which describe internal properties of the nucleus and do not account for the orientation of the nucleus in a laboratory system, are performed in this intrinsic frame. With nonzero deformation the intrinsic nuclear state $|\phi\rangle$ is no longer an angular momentum eigenfunction; our calculations break the rotational symmetry (the intrinsic frame defines a preferential coordinate system for the nucleus). To calculate β-decay matrix elements between angular

momentum-conserving states as in Chapter 2 we must, at least approximately, restore the angular momentum symmetry of the state $|\phi\rangle$.

3.1.1: Angular momentum projection and the collective rotor model

The proper way to obtain angular momentum eigenstates from a deformed state $|\phi\rangle$ is to project out the desired components: $|JM\rangle = \hat{P}_{JM}|\phi\rangle$. As detailed in Ref. [72], the symmetry-restored state obtained in this manner is given by[1]

$$|JM\rangle \sim \sum_K g_K \int d\boldsymbol{\Omega}\, \mathscr{D}^J_{MK}(\boldsymbol{\Omega})\hat{R}(\boldsymbol{\Omega})|\phi\rangle, \tag{3.2}$$

where K enumerates the z projections of angular momentum in the state $|\phi\rangle$, the vector $\boldsymbol{\Omega} = (\phi, \theta, \psi)$ represents the three Euler angles, $R(\boldsymbol{\Omega}) = e^{-i\phi J_z} e^{-i\theta J_y} e^{-i\psi J_z}$ is the rotation operator, and $\mathscr{D}^J_{MK}(\boldsymbol{\Omega}) = \langle JM|R(\boldsymbol{\Omega})|JK\rangle^*$ is a Wigner D function; the latter three quantities are defined using the conventions in Ref. [76]. Equation (3.2) defines the angular momentum eigenstate $|JM\rangle$ as an average over all possible orientations $\boldsymbol{\Omega}$ of the intrinsic state weighted by the amplitude $\mathscr{D}^J_{MK}(\boldsymbol{\Omega})$.

The application of the states (3.2), e.g., minimizing the energy to find the ground state, is a difficult task. The problem can be simplified if we approximate the intrinsic nuclear state $|\phi\rangle$ as being strongly deformed and pointing in a specific direction $|\boldsymbol{\Omega}\rangle$ [72]. Then the symmetry-restored wave function is approximately given by the inner product

$$\langle\boldsymbol{\Omega}|JM\rangle \propto \sum_K g_K \mathscr{D}^J_{MK}(\boldsymbol{\Omega}), \tag{3.3}$$

and is simply proportional to the rotation matrix elements $\mathscr{D}^J_{MK}(\boldsymbol{\Omega})$.

The result (3.3) suggests the collective rotor model of Bohr and Mottelson [74, 76] (hereafter the "collective model") can be applied as an approximation to full angular momentum projection [72]. The model is typically used to represent the collective rotation of a deformed nucleus by coupling the intrinsic nuclear wave function ϕ to a rotation wave function which describes the orientation of the nucleus in the laboratory coordinate system: $\Psi_{JMK}(\boldsymbol{\Omega}) \sim \mathscr{D}^J_{MK}(\boldsymbol{\Omega})\phi_K$. States of this kind are solutions of the Hamiltonian [74]

$$\hat{H}_{\text{coll}} = \hat{H}_{\text{intr}} + \hat{H}_{\text{rot}}, \tag{3.4}$$

neglecting any coupling between rotations and intrinsic excitations. The Hamiltonian (3.4) thus incorporates both intrinsic excitations of the nucleus ($\hat{H}_{\text{intr}}$, the Hamiltonian used in our deformed calculations) and rotational excitations ($\hat{H}_{\text{rot}}$) in the lab frame. The collective model is particularly simple because we can

---

[1]Ref. [72] uses a different convention for the rotation operator and D functions than we do (we follow Ref. [74]). We have attempted to translate the results in this section to keep the notation consistent.

calculate the intrinsic-frame nuclear states directly and express the corresponding lab-frame states analytically later.

Section 3.2: Matrix elements and transition strengths in the collective rotor model

Lab-frame nuclear wave functions and matrix elements in the collective model can be taken directly from Ref. [74], incorporating the fact that our intrinsic nuclear states described in Chapters 5 and 6 are (1) axially symmetric (invariant under rotations about the intrinsic z axis) and (2) reflection symmetric (invariant when rotated by $180°$ about an axis perpendicular to the intrinsic z axis) [77, 78]. Axial symmetry guarantees the z projection of angular momentum K in the intrinsic frame is a constant of the motion and equal to the projection M in the laboratory coordinate system. The reflection symmetry requires intrinsic states $\phi_{K>0}$ to be singly degenerate with partner states $\phi_{\overline{K}<0} = \hat{R}_y(\pi)\,\phi_K$ related by a $180°$ rotation. We present the primary expressions for matrix elements and transition strengths following Ref. [74] below, but include more details in Appendix B.

The lab-frame wave functions built up from our intrinsic wave functions ϕ_K are[2]

$$\Psi_{J,M=K,K=0}(\mathbf{\Omega}) = \left(\frac{2J+1}{8\pi^2}\right)^{1/2} \mathscr{D}_{00}^J(\mathbf{\Omega})\,\phi_{K=0}, \tag{3.5a}$$

$$\Psi_{J,M=K,K>0}(\mathbf{\Omega}) = \left(\frac{2J+1}{16\pi^2}\right)^{1/2} \left\{\mathscr{D}_{KK}^J(\mathbf{\Omega})\phi_K + (-1)^{J-K}\mathscr{D}_{K,-K}^J(\mathbf{\Omega})\,\phi_{\overline{K}}\right\}, \tag{3.5b}$$

and couple the intrinsic nuclear states to D functions as seen above in the approximate symmetry restoration. Because of the intrinsic axial symmetry, these wave functions always have $M = K$, and the reflection symmetry of the intrinsic states dictates that we can only construct a single lab-frame wave function for each pair of intrinsic states ϕ_K and $\phi_{\overline{K}}$ [74]. These lab-frame solutions are grouped into "rotation bands" with different values of the total angular momentum $J \geq K$ anchored to intrinsic states ϕ_K. The lowest-energy state in a band, $\Psi_{J=K,K}(\mathbf{\Omega})$, is called the "band head."

The quantities required for our β-decay calculations, described in Chapter 2, involve the products of reduced matrix elements $\langle J_f\,K_i\,||\,\hat{O}_\lambda\,||\,J_i\,K_i\rangle$ in the laboratory coordinate system.[3] These reduced matrix element are obtained from full matrix elements between the states (3.5) via the Wigner-Eckart theorem [76, 79]:

$$\langle J_f\,M_f\,K_f\,|\,\hat{O}_{\lambda\mu}\,|\,J_i\,M_i\,K_i\rangle = \frac{(\,J_i\,M_i\,\lambda\,\mu\,|\,J_f\,M_f\,)}{\sqrt{2J_f+1}}\langle J_f\,K_f\,||\,\hat{O}_\lambda\,||\,J_i\,K_i\rangle. \tag{3.6}$$

---

[2]We use a slightly different phase convention than Ref. [74] for our rotation operator, which produces the phase factor $(-)^{J-K}$.

[3]We include the labels K in reduced matrix elements since it is an intrinsic property of the nuclear wave function. The spin reduction simply removes the M-dependence of the matrix element which happens to be equal to K for axially symmetric nuclei.

Specifically, we need the squares of lab-frame matrix elements, called the transition strength B:

$$B(\hat{O}_\lambda; J_i K_i \to J_f K_f) = \frac{1}{2J_i + 1} \left| \langle J_f\, K_f \,||\, \hat{O}_\lambda \,||\, J_i\, K_i \rangle \right|^2, \tag{3.7}$$

and products of matrix elements, which we call cross-terms X, between operators $\hat{O}^{(1)}$ and $\hat{O}^{(2)}$:

$$X(\hat{O}_\lambda^{(1)}, \hat{O}_\lambda^{(2)}; J_i K_i \to J_f K_f) = \frac{1}{2J_i + 1} \langle J_f\, K_f \,||\, \hat{O}_\lambda^{(1)} \,||\, J_i\, K_i \rangle \langle J_f\, K_f \,||\, \hat{O}_\lambda^{(2)} \,||\, J_i\, K_i \rangle^*. \tag{3.8}$$

For transitions from even-even nuclei, which have $J = 0$ (and $K = 0$) in their ground states, these quantities are very simple to express in terms of quantities in the intrinsic coordinate system; the final-state angular momentum J_f must equal that of the operator λ, and the lab-frame transition strength is proportional to the strength calculated in the intrinsic frame:

$$B(\hat{O}_\lambda; 0\,0 \to \lambda\,K_f) = \Theta_K^2 \mathcal{B}^{\mathrm{intr}}(\hat{O}_{\lambda, K=K_f}; K_i = 0 \to K_f), \qquad \Theta_K = \begin{cases} 1, & K_f = 0, \\ \sqrt{2}, & K_f > 0 \end{cases}. \tag{3.9}$$

The intrinsic strength $\mathcal{B}^{\mathrm{intr}}(\hat{O}_{\lambda K}; K_i \to K_f) \equiv \left| \langle K_f \,|\, \hat{O}_{\lambda K} \,|\, K_i \rangle \right|^2$ depends only on quantities expressed in the intrinsic frame and is calculated using the methods in Chapters 5 and 6. The fact that the cross-terms involve matrix elements of two different operators does not change the result (3.9), and the lab-frame cross-terms X (3.8) can be written in terms of intrinsic-frame quantities $\mathfrak{X}(\hat{O}_{\lambda K}^{(1)}, \hat{O}_{\lambda K}^{(2)}; K_i \to K_f)$.

Expressions for B and X in odd nuclei, which have $J \neq 0$ in their ground states, are more complicated since the final-state angular momentum can take on a range of values $|J_i - \lambda| \leq J_f \leq J_i + \lambda$. If, however, we make the zeroth-order approximation that the rotational motion does not contribute significantly to the energy of the nucleus, then all the final states $|J_f\,K_f\rangle$ in a rotation band will be degenerate. The sum over all final states in a band will thus enter the β-decay calculation together, and this sum does have a simple form, similar (though not identical) to that worked out in Ref. [80]:

$$\sum_{J_f = |J_i - \lambda|}^{J_i + \lambda} B(\hat{O}_\lambda; J_i K_i \to J_f K_f) = \mathcal{B}^{\mathrm{intr}}(\hat{O}_{\lambda, K=K_f - K_i}; K_i \to K_f)$$

$$+ \mathcal{B}^{\mathrm{intr}}(\hat{O}_{\lambda, K=K_f + K_i}; \overline{K}_i \to K_f), \tag{3.10}$$

with equivalent results for the cross-terms X. The second term in Eq. (3.10) is new compared to Eq. (3.9) and arises from the interference between $K > 0$ and $\overline{K} < 0$ wave functions in Eq. (3.5b). Its contribution incorporates transitions from the angular momentum-reversed state $\phi_{\overline{K}}$ when allowed by conservation of

angular momentum (i.e. when $\left|K_i + K_f\right| \leq \lambda$).

Section 3.3: β-decay half-lives of axially-deformed nuclei

With the expressions (3.9) and (3.10), which connect lab-frame β-decay transition strengths to their intrinsic-frame counterparts, we can write down the total β-decay rate solely in terms of intrinsic quantities. Recalling Eq. (2.11), the total rate is calculated as a sum over all the contributions from energetically-allowed decays to states in the daughter nucleus:

$$\lambda = \frac{\ln 2}{\kappa} \sum_{J^\pi} \sum_{J_f} \sum_{N(J^\pi, J_f)} \int_1^{W_0(N)} C_{J^\pi}(B_{N,J_f}, X_{N,J_f}) f(W_0(N), W_e) \, \mathrm{d}W_e, \tag{3.11}$$

where J^π is the angular momentum and parity of the various allowed and forbidden transitions, J_f is the final-state angular momentum of the daughter nucleus, N enumerates energetically-accessible final states, and f contains the remaining energy dependent factors. The shape factors $C_{J^\pi}(B_{N,J_f}, X_{N,J_f})$ were described in detail in Chapter 2; they are comprised of energy-dependent combinations of lab-frame transition strengths B and cross-terms X.

Our calculation of the β-decay rate for even-even and odd nuclei is simplified by the approximation mentioned above, i.e., the rotational excitation energies which depend on J_f and J_i can be neglected relative to the energies E_K of the intrinsic excitations. With this approximation, the sum over J_f can be taken inside the integral (3.11), and the shape factor C can be expressed very simply in terms of intrinsic transition strengths and cross-terms defined in Eqs. (3.9) and (3.10).

We calculate the total decay rate by summing over the contributions of energetically allowed intrinsic excitations $N(\Delta K)$ between rotation bands either with $K_i = K_f$ ($\Delta K = 0$) or $K_i \neq K_f$ ($\Delta K \neq 0$) as long as $K_f \geq 0$ (Eq. (3.5b)). This sum is performed for each type of decay we consider (1^+, 0^-, etc.), and the total gives the decay rate, expressed in terms of intrinsic nuclear quantities:

$$\lambda = \frac{\ln 2}{\kappa} \sum_{J^\pi} \sum_{\Delta K = -J}^{J} \sum_{N(\Delta K)} \int_1^{W_0(N)} \mathcal{C}_{J^\pi, \Delta K}(\mathcal{B}_N^{\mathrm{intr}}, \mathcal{X}_N^{\mathrm{intr}}) f(W_0(N), W_e) \, \mathrm{d}W_e. \tag{3.12}$$

The intrinsic shape factor $\mathcal{C}_{J^\pi, \Delta K}^{\mathrm{intr}}(\mathcal{B}^{\mathrm{intr}}, \mathcal{X}^{\mathrm{intr}})$ has the same form as its lab-frame counterpart but includes the necessary ΔK-dependent factors (cf. Eq. (3.9)) multiplying the intrinsic transition strengths and cross-terms.

CHAPTER 4: DENSITY FUNCTIONAL THEORY AND THE LINEAR RESPONSE OF THE NUCLEUS

Any realistic nuclear β-decay calculation must take into account the strong interactions among nucleons when calculating energies, angular momenta, parities, etc. of the states that contribute to the decay. In the this chapter we provide an introduction to density functional theory, often applied in atomic physics and nowadays also in nuclear physics, which provides a self-consistent way to account for the strong interactions between nucleons using only local nuclear densities: the usual density in coordinate space $\rho(\mathbf{r})$, the spin density, and a variety of other local densities that include derivatives. We also briefly review linear response theory—the foundation for our β-decay calculations—which allows the calculation of excited-state properties by considering the effect of external fields on the nuclear density.

The nuclear strong interactions are extremely complicated, and until, e.g., *ab initio* techniques can be extended across the nuclear chart there are a plethora of phenomenological effective nuclear interactions available for use [72]. These effective interactions are often applied to nuclear physics calculations within the framework of self-consistent mean-field (SCMF) models such as the Hartree-Fock (HF) approximation (or the Hartree-Fock-Bogoliubov approximation if pairing correlations are considered). SCMF models have the advantages of (1) simplifying calculations by treating the nucleons as independent particles in a potential and (2) building the central potential up microscopically from two-body interactions among the nucleons. Although these models are relatively simple to apply, their solutions are approximations to the exact states of the nucleus, and they still rely on Hamiltonians constructed from phenomenological interactions. It is common to find interactions that, for example, depend on the nuclear density ρ (e.g., the popular Skyrme interactions that we use and discuss below), and it isn't especially clear what a density-dependent Hamiltonian actually means [81].

Kohn-Sham density functional theory (KS-DFT) provides a more appealing way to calculate nuclear properties than do mean field models, since it guarantees the possibility of finding the *exact* ground-state energy and density of a system while still solving mean-field-type equations. The foundation of KS-DFT is a pair of theorems proved by Hohenberg and Kohn (HK) [82] and Kohn and Sham (KS) [83]. The theorem of Hohenberg and Kohn, originally proved for electronic systems in an external potential, guarantees a method for finding the exact ground-state energy and density. The energy of a system placed in an external potential

$v_\text{ext}(\mathbf{r})$ can be written solely as functional of the density,

$$E[\rho] = \int v_\text{ext}(\mathbf{r})\rho(\mathbf{r}) \, \mathrm{d}\mathbf{r} + F[\rho(\mathbf{r})], \tag{4.1}$$

and the minimum value of this functional, for all densities $\rho(\mathbf{r})$ that have the correct number of particles $\int \rho(\mathbf{r}) \, \mathrm{d}\mathbf{r} = N$, is the exact ground-state energy of the system *if* we know the correct functional $F[\rho(\mathbf{r})]$. The density that minimizes $E[\rho(\mathbf{r})]$ is then also the exact ground-state density.

Kohn and Sham demonstrated the density that minimizes the functional (4.1) can be obtained from an auxiliary, simple system of non-interacting particles that solve Schödinger equations of the type [84]

$$-\frac{1}{2}\nabla^2\psi_i(\mathbf{r}) + \int v_\text{KS}(\mathbf{r}, \mathbf{r}')\psi_i(\mathbf{r}') \, \mathrm{d}\mathbf{r}' = E_i\psi_i(\mathbf{r}). \tag{4.2}$$

The Kohn-Sham potential v_KS in Eq. (4.2) is defined as a functional derivative of the exchange-correlation part of the energy density functional (EDF),

$$v_\text{KS} \equiv \delta E_\text{xc}[\rho]/\delta\rho, \tag{4.3}$$

where the EDF has been separated into a kinetic energy piece $T[\rho]$ and a piece that describes the correlations among nucleons: $E[\rho] = T[\rho] + E_\text{xc}[\rho]$. Since the KS equations (4.2) describe a system of independent particles, the ground-state density simply corresponds to that of a Slater determinant: $\rho(\mathbf{r}) = \sum_{i=1}^{A} |\psi_i(\mathbf{r})|^2$. It is in this sense (the treatment of independent particles orbiting in an average field) that Kohn-Sham DFT behaves just like a mean-field theory.

Kohn-Sham DFT is superior to SCMF models in principle, since it can yield the exact ground state energy and density [84] while SCMF models can only provide mean-field approximations to these quantities. Unfortunately the HK and KS theorems do not offer guidance regarding the form of the functional $E[\rho]$. Even when it has been worked out that the HK and KS theorems carry over into nuclear physics [85], we do not have nuclear EDFs from *ab initio* methods as in electronic systems [86]; the functionals in common use are still phenomenological. The two most commonly-used non-relativistic functionals are the Skyrme and Gogny functionals (see the review article [86]). We prefer Skyrme functionals since they depend only on nuclear densities that are local in coordinate space (the energy functional takes the form $E[\rho] = \int H(\mathbf{r}) \, \mathrm{d}\mathbf{r}$): Skyrme functionals produce results more quickly than non-local or finite-range methods (which require additional integrations) and are simpler to implement.

Section 4.1:   The Skyrme energy-density functional

As mentioned above, Skyrme functionals are built up from combinations of local nuclear densities and have the form

$$E_{\text{Sk}}[\rho] = \int H_{\text{Sk}}(\mathbf{r}) \, d\mathbf{r}, \qquad H_{\text{sk}}(\mathbf{r}) = H_{\text{Sk}}[\rho(\mathbf{r}), \dots]. \tag{4.4}$$

Modern Skyrme functionals are, by constructions, at least quadratic in local densities (additional density dependence may be introduced, corresponding to density-dependent interactions) and are built up from the usual density $\rho(\mathbf{r})$, the spin density $\mathbf{s}(\mathbf{r})$, and local combinations of up to two powers of derivatives of these densities in a variety of combinations [87, 88]. The nuclear densities, besides being local in coordinate space, also depend on spin and isospin.

The functional (4.4) is often split into different pieces [86, 89] formed from distinct combinations of nuclear densities:

$$E_{\text{Sk}}[\rho] = \sum_{T=0,1} \int \left[H_T^{\text{even}}(\mathbf{r}) + H_T^{\text{odd}}(\mathbf{r}) \right] \, d\mathbf{r}. \tag{4.5}$$

The labels T and "even/odd" describe the types of nuclear densities that make up the $H_T(\mathbf{r})$. Terms with $T = 0$ are built up from densities that are independent of the nucleon charge (isoscalar densities), and terms with $T = 1$ are built up from densities that depend on the isospin (isovector densities).

Terms labeled "even" are formed from densities that are even under the action of the time reversal operator (e.g., $\hat{T}\hat{O}\hat{T}^{-1} = \hat{O}$), which among other things reverses the angular momentum [90]. The usual nuclear density $\rho(\mathbf{r})$ is the simplest example of a time-even density. The "odd" terms are formed from densities that are odd under time reversal; for example, the spin density $\mathbf{s}(\mathbf{r})$ is proportional to the spin operator $\boldsymbol{\sigma}$ and changes sign when acted upon by $\hat{T}$. Each of the terms $H_T^{\text{even/odd}}$ are parameterized with a number of coupling constants C_T, and the Skyrme EDF contains approximately 30 couplings altogether.

We should mention that the Skyrme functional (4.4) is actually a generalization of Skyrme's original two-body effective interaction [91, 92]—a local ($v \propto \delta(\mathbf{r}_1 - \mathbf{r}_{1'})\delta(\mathbf{r}_2 - \mathbf{r}_{2'})$), contact ($v \propto \delta(\mathbf{r}_1 - \mathbf{r}_2)$) [72], density-dependent interaction with approximately a dozen parameters [86, 88]. In fact, one can obtain an effective two-body Skyrme interaction from E_{Sk} by taking two functional derivatives: $v_{\text{Sk}} \sim \delta^2 E_{\text{Sk}}[\rho]/\delta\rho^2$. The large number of parameters in both the Skyrme EDF and the interaction has allowed a large, diverse set of fits to nuclear data over the decades. All these parameterizations have essentially the basic functional form of Eq. (4.4), but can differ dramatically in their reproduction of nuclear data in various situations.

In practical applications the Skyrme functional is flexible enough (containing roughly twice as many adjustable parameters as the Skyrme interaction) to either mimic a Skyrme interaction (in which case the couplings constants of the EDF are related to the parameters of the two-body interaction) or abandon the

constraints of an interaction entirely (the coupling constants are directly fit to data) [86]. In either case the functional can be applied in the Kohn-Sham DFT formalism as an approximation to the nuclear EDF [86, 93],

$$E[\rho] = T[\rho] + E_{\mathrm{Sk}}[\rho] + \ldots, \tag{4.6}$$

to calculate ground-state properties. Properties of excited states can subsequently be obtained with time-dependent density functional theory and linear response theory, described below.

Section 4.2: Time-dependent DFT

The density functional theory outlined above describes the static properties of nuclei, e.g., the ground-state energy and density of the nucleus. Expectation values of observables in the ground state can also be calculated with the nuclear density: $\langle \hat{O}(\mathbf{r}) \rangle = \mathrm{Tr}\, \hat{O}\rho$. Along the same lines, we can calculate transitions to excited states either in the same nucleus (like-particle excitations) or in neighboring nuclei (charge-changing excitations) using the time-dependent version of DFT.

The time-dependent density functional theory (TDDFT) is obtained with the proof of a time-dependent version of the HK theorem by Runge and Gross [94] that allows for a corresponding time-dependent version of the Kohn-Sham equations [84]:

$$i\frac{\partial}{\partial t}\psi_i(\mathbf{r},t) = -\frac{1}{2}\nabla^2\psi_i(\mathbf{r},t) + v_{\mathrm{KS}}(\mathbf{r},t)\psi_i(\mathbf{r},t). \tag{4.7}$$

If we treat the time-dependent KS potential $v_{\mathrm{KS}}(\mathbf{r},t)$ in the adiabatic approximation, meaning the time-dependence of the functional enters only through the nuclear density [84] $E[\rho(t)]$, then we can calculate time-dependent properties self-consistently. That is, we can use the same Skyrme EDF to model both the ground state and excited states of the nuclear system. The adiabatic approximation essentially means that the functional has no memory—it is local in time [84]. Ref. [84] suggests that, since $v_{\mathrm{KS}} = \delta E/\delta\rho$ is first used to find the ground state, the adiabatic approximation could work in situations involving small time-dependent changes to the density—i.e., the regime of linear response, where we investigate small time-dependent oscillations of the density around the ground state.

Now, in a similar way as the static Kohn-Sham DFT behaves like a static mean-field theory, the TDDFT behaves like time-dependent mean-field theory. For example in Ref. [84] the system described with time-dependent DFT obeys independent-particle Schrödinger equations (4.7), and the time-dependent density is that of a Slater determinant: $\rho(\mathbf{r},\mathbf{r}',t) = \sum_{i=1}^{A}\psi_i(\mathbf{r},t)\psi_i^*(\mathbf{r}',t)$. These are the same properties as in, e.g., the time-dependent Hartree-Fock (TDHF) theory as presented in Ref. [72]. If the single-particle wave functions

are solutions of Eq. (4.7), then the density obeys the non-linear TDHF equation

$$i\dot{\rho}(t) = [h[\rho(t)], \, \rho(t)],$$ (4.8)

where $h[\rho] = \delta E[\rho]/\delta\rho$ is the time-dependent Kohn-Sham mean field. Note, however, that TDDFT is still not a mean field theory [84]: in principle we can still obtain the exact time-dependent density $\rho(t)$ (up to errors due to the adiabatic approximation) if we knew the exact functional $E[\rho]$.

Section 4.3: Linear response theory

To actually calculate excitations of the nucleus, we apply linear response theory to calculate the first-order changes in the nuclear density caused by a weak external field $f(t)$. These (presumably small) changes in the density contain the information necessary for calculating transition probabilities to excited states [72]. Linear response theory is discussed in detail in, e.g., Chapter 8 of Ref. [72] and Chapter 10 of Ref. [95]; we review the essentials here, following these references.

The linear response approximation to TDDFT is a technique for solving the TDHF equation (4.8), which depends in a complicated way on the density $\rho(t)$, under the influence of a weak perturbing field $f(t) \propto \eta \ll 1$. Since $f(t)$ is weak, we can expand Eq. (4.8) to first order in the parameter η, expecting that any induced time-dependence in the nuclear density is also $\mathcal{O}(\eta)$, i.e. $\rho(t) \approx \rho_0 + \eta\delta\rho(t)$. This expansion yields the commutator equation

$$i\delta\dot{\rho}(t) = [h_0, \, \delta\rho(t)] + [\delta h(t) + f(t), \, \rho_0],$$ (4.9)

where $h_0 = \delta E[\rho]/\delta\rho|_{\rho=\rho_0}$ is the ground-state Kohn-Sham mean field, and

$$\delta h(t) = \frac{\delta h}{\delta\rho} \cdot \delta\rho(t) = \left.\frac{\delta^2 E}{\delta\rho^2}\right|_{\rho=\rho_0} \cdot \delta\rho(t)$$ (4.10)

is the first-order correction to the mean field. We have also used the fact that $[h_0, \, \rho_0] = 0$ for the ground-state solution [95]. Solutions $\delta\rho(t)$ of Eq. (4.9) are simpler to compute in the frequency domain, where one assumes a simple sinusoidal time-dependence for the external field: $f(t) = f(\omega)e^{-i\omega t} + f^\dagger(\omega)e^{i\omega t}$. It is then reasonable that the perturbed density has the same form as $f(t)$ (it must also be Hermitian):

$$\delta\rho(t) = \delta\rho(\omega)e^{-i\omega t} + \delta\rho^\dagger(\omega)e^{i\omega t}.$$ (4.11)

The goal of the linear response calculation is to determine the response function $\mathscr{R}$ from Eq. (4.9) which,

in turn, gives the solutions $\delta\rho(\omega)$:

$$\delta\rho_{ij}(\omega) = \sum_{kl} \mathscr{R}_{ij,kl}(\omega) f_{kl}(\omega). \tag{4.12}$$

The response function $\mathscr{R}(\omega)$ has simple poles at the natural excitation frequencies of the nucleus—even a small field with frequency $\omega = \Omega_\nu$, corresponding to an eigenfrequency of the system, is enough to place the nucleus in the excited state $|\nu\rangle$ [72]. As a result the response function allows for direct calculation of the strength function $S_F(\omega)$, which contains the transition probabilities to excited states:

$$\begin{aligned}
S_F &= -\frac{1}{\pi}\operatorname{Im}\operatorname{Tr} f^\dagger(\omega)\delta\rho(\omega) \\
&= -\frac{1}{\pi}\operatorname{Im}\sum_{kk'll'} f_{kl}^*(\omega)\mathscr{R}_{kl,k'l'}(\omega)f_{k'l'}(\omega) \\
&= \sum_\nu |\langle\nu|f|0\rangle|^2 \,\delta(\omega - \Omega_\nu).
\end{aligned} \tag{4.13}$$

Our β-decay strength functions are calculated in the same way as Eq. (4.13). The goal of the calculations is thus to compute our version of $\delta\rho(\omega)$, which contains the transition strengths required for nuclear β-decay.

CHAPTER 5:   THE PROTON-NEUTRON FINITE AMPLITUDE METHOD

In this chapter and the next we describe the proton-neutron finite amplitude method—a technique we have developed and applied to compute β-decay half-lives. The finite amplitude method (FAM) is a recent numerical advance in nuclear structure theory. Combining the linear response approximation with numerical differentiation, the FAM yields a tremendous speedup for calculations of nuclear transition strengths. In fact, while traditional calculations (using, e.g., the matrix version of the random phase approximation (RPA) or its extension to systems with pairing correlations, the quasiparticle RPA) scale like $\mathcal{O}(N^2)$–$\mathcal{O}(N^3)$ with the size of the basis, FAM applications scale more-or-less linearly with the size of the calculation, $\mathcal{O}(N)$ [96]. By adapting the FAM to calculate the charge-changing nuclear transitions (neutron to proton or vice versa) involved in β decay, we have produced a method enabling large-scale calculations of weak decays across the entire nuclear chart.

The FAM was originally presented in 2007 [97] for spherical nuclei without pairing correlations (i.e., using time-dependent HF theory), and it has been adapted and extended numerous times since its introduction. We have introduced our own version of the method [61] that is based on the work of Ref. [98], which extended the FAM to nuclear systems with pairing correlations. Our adaptation of the FAM allows us to calculate charge-changing excitations of arbitrary J_z in deformed nuclei.

Our extension, the "proton-neutron finite amplitude method" or "pnFAM", was developed in collaboration with M. T. Mustonen, a postdoctoral research associate at UNC from 2012 to 2015. Together we built the computer program PNFAM to carry out β-decay calculations. We have published a paper which describes the program and contains an introductory application [61], and recently M. T. Mustonen has applied the PNFAM program to study fine properties of the Skyrme energy density functionals we employ [60]. In a nice demonstration of the speed of the FAM, he also calculated β-decay rates of a large number of even-even nuclei across the nuclear chart.

This chapter, describing the pnFAM for even-even nuclei, presents original research performed by the author in collaboration with M. T. Mustonen. In practice, the author and M. T. Mustonen divided the development workload roughly evenly: M. T. Mustonen worked out much of the main formalism presented and expounded upon here, while the author spent significant effort implementing the charge-changing Skyrme EDF, following the work of M. Bender [99, 100] and Perlińska *et al.* [88], as well as the β-decay formalism presented previously. These are not strict distinctions, however, and the programming workload was distributed fairly

evenly. In Chapter 6 we will present an extension of the pnFAM, derived by the author, which enables the calculation of β-decay half-lives of odd nuclei. We have restricted our presentation of the FAM in this chapter to essentially the main points. Further details are presented in Appendix C.

Section 5.1:   Mean field theory with pairing correlations: the HFB approximation

Since our pnFAM technique is intended to be applicable across the nuclear chart, the inclusion of nuclear pairing correlations in the ground state and in our β-decay calculations is essential. With these pairing correlations included, our FAM solutions (which we will describe in Sec. 5.2) are obtained by solving the time-dependent Hartree-Fock-Bogoliubov (HFB) equations in the linear response approximation [98].

In a similar way as Hartree-Fock (HF) theory provides a mean-field description for a system of non-interacting particles, the HFB approximation incorporates nuclear pairing correlations by describing a system of non-interacting *quasiparticles* [72]. It will be helpful to review the main points of the HFB here before moving on to describe the FAM. Thorough presentations of the HFB are provided in textbooks, particularly Chapter 7 in each of Refs. [72] and [95], and we borrow primarily from these two texts.

The quasiparticles introduced in the HFB are related to the "usual" single-nucleon states by a Bogoliubov transformation, specified in terms of two complex matrices $U_{k\mu}$ and $V_{k\mu}$ that connect the particle states (hereafter with Latin indices) to the quasiparticle ones (Greek indices):

$$
\begin{aligned}
\alpha_\mu &= \sum_i \left(U_{k\mu}^* c_k + V_{k\mu}^* c_k^\dagger \right), \\
\alpha_\mu^\dagger &= \sum_i \left(V_{k\mu} c_k + U_{k\mu} c_k^\dagger \right).
\end{aligned}
\tag{5.1}
$$

The $c^\dagger$'s and c's are the creation and annihilation operators for single-particle states, and the $\alpha^\dagger$'s and α's are the corresponding operators for the quasiparticles. The transformations (5.1) can conveniently be written in matrix form,

$$
\begin{pmatrix} c \\ c^\dagger \end{pmatrix} = \mathbb{W} \begin{pmatrix} \alpha \\ \alpha^\dagger \end{pmatrix}, \qquad \mathbb{W} = \begin{pmatrix} U & V^* \\ V & U^* \end{pmatrix},
\tag{5.2}
$$

and the matrix $\mathbb{W}$ is unitary ($\mathbb{W}\mathbb{W}^\dagger = \mathbb{W}^\dagger\mathbb{W} = 1$). It also preserves the fermionic character of the nucleons through the usual anticommutation relations among the quasiparticle creation and annihilation operators:

$$
\left\{ c_i^\dagger, c_j \right\} = \delta_{ij} \xrightarrow{\ \mathbb{W}\ } \left\{ \alpha_\mu^\dagger, \alpha_\nu \right\} = \delta_{\mu\nu}.
\tag{5.3}
$$

The HFB ground state $|\phi\rangle$ is defined as the vacuum for the quasiparticles, $\alpha_\mu|\phi\rangle = 0$, but *not* for the bare particles: $c_k|\phi\rangle \neq 0$. The inclusion of pairing correlations via the introduction of quasiparticles

introduces a new type of density, the pairing tensor κ, alongside the usual nuclear density ρ. These densities are represented by matrices built up from the U and V matrices:

$$\rho_{ij} = \langle\phi\,|\,c_j^\dagger c_i\,|\,\phi\rangle = (V^* V^T)_{ij}, \tag{5.4a}$$

$$\kappa_{ij} = \langle\phi\,|\,c_j c_i\,|\,\phi\rangle = (V^* U^T)_{ij}. \tag{5.4b}$$

The density ρ is Hermitian, κ is antisymmetric, and the two densities are often combined to form a very useful matrix called the generalized density:

$$\mathcal{R} = \begin{pmatrix} \langle\phi\,|\,c_j^\dagger c_i\,|\,\phi\rangle & \langle\phi\,|\,c_j c_i\,|\,\phi\rangle \\ \langle\phi\,|\,c_j^\dagger c_i^\dagger\,|\,\phi\rangle & \langle\phi\,|\,c_j c_i^\dagger\,|\,\phi\rangle \end{pmatrix} = \begin{pmatrix} \rho_{ij} & \kappa_{ij} \\ -\kappa_{ij}^* & 1 - \rho_{ij}^* \end{pmatrix}. \tag{5.5}$$

The HFB generalized density is required to satisfy the requirement $\mathcal{R}^2 = \mathcal{R}$ in the same way that the density of independent particles without pairing correlations is required to satisfy $\rho^2 = \rho$. In fact, many aspects of mean field theory without pairing correlations (including linear response theory described in Chapter 4) can be easily adapted to include pairing by substituting $\rho \to \mathcal{R}$ and working in this new larger basis [72].

The property $\mathcal{R}^2 = \mathcal{R}$ is easy to demonstrate by introducing a new bit of technology: we can transform the generalized density $\mathcal{R}_{ij}$ from the particle basis to the quasiparticle basis ($\mathbb{R}_{\mu\nu}$) by transforming the c's to α's using the matrix $\mathbb{W}$:

$$\mathbb{R} = \mathbb{W}^\dagger \mathcal{R} \mathbb{W} = \begin{pmatrix} 0 & 0 \\ 0 & 1 \end{pmatrix}, \tag{5.6}$$

where 1 represents the identity matrix. This transformation between single-particle matrices (calligraphic font) and quasiparticle matrices (outlined font) with the matrix $\mathbb{W}$ simplifies our description of the pnFAM equations. It is of special importance here since it shows that the columns of $\mathbb{W}$ diagonalize $\mathcal{R}$ [72]. Clearly $\mathbb{R}^2 = \mathbb{R}$, and the unitary of $\mathbb{W}$ ensures this is the case for $\mathcal{R}$ as well.

Having defined the HFB ground state wave function and the corresponding generalized density, the total energy is determined through the minimization procedure [95]

$$\delta\Big\{ E[\rho, \kappa] - \lambda(\mathrm{Tr}\,\rho - N) - \mathrm{Tr}[\Lambda(\mathcal{R}^2 - \mathcal{R})] \Big\} = 0. \tag{5.7}$$

The parameters λ and $\Lambda_{kk'}$ in Eq. (5.7) are Lagrange multipliers which (1) constrain the average particle number to the chosen value N and (2) ensure the system obeys the restriction $\mathcal{R}^2 = \mathcal{R}$. In Eq. (5.7) the energy is now a functional of both ρ and κ (or, of $\mathcal{R}$ or the U and V matrices), and it has been shown for

26

similar systems [101–103] that a variational procedure can produce Kohn-Sham-type equations for essentially the matrices $U_{k\mu}$ and $V_{k\mu}$. The solution of (5.7) yields the HFB equation for the ground state solution,

$$[\mathcal{H}[\mathcal{R}],\, \mathcal{R}] = 0, \tag{5.8}$$

where $\mathcal{H}[\mathcal{R}] = \mathcal{H}[\rho, \kappa]$ is the HFB Hamiltonian matrix defined via the expression $\delta E = \frac{1}{2}\operatorname{tr}\mathcal{H}\delta\mathcal{R}$ [95]:

$$\mathcal{H}[\mathcal{R}] = \begin{pmatrix} h_{ij} - \lambda & \Delta_{ij} \\ -\Delta_{ij}^* & -(h_{ij}^* - \lambda) \end{pmatrix}. \tag{5.9}$$

The matrix $\mathcal{H}$ is composed from both the usual single-particle mean field $h_{ij}[\rho, \kappa] = \delta E[\rho, \kappa]/\delta\rho_{ji}$ (which is Hermitian since E is real and $\rho = \rho^\dagger$) and the pairing field $\Delta_{ij}[\rho, \kappa] = \delta E[\rho, \kappa]/\delta\kappa_{ij}^*$ (which is antisymmetric since $\kappa = -\kappa^T$). In practice the energy functional $E[\rho, \kappa]$ is usually divided into two separate functionals, $E = E_{\text{Sk}}[\rho] + E_{\text{pair}}[\rho, \kappa]$, which are specified separately and determine the mean field and the pairing field.

Solutions of Eq. (5.8) are obtained when $\mathcal{H}$ and $\mathcal{R}$ are mutually diagonal. Since U and V diagonalize $\mathcal{R}$ by definition [Eq. (5.6)] one needs only to choose $U_{k\mu}$ and $V_{k\mu}$ such that they also diagonalize $\mathcal{H}$:

$$\begin{pmatrix} h - \lambda & \Delta \\ -\Delta^* & -(h^* - \lambda) \end{pmatrix}_{ij} \begin{pmatrix} U \\ V \end{pmatrix}_{j\mu} = E_\mu \begin{pmatrix} U \\ V \end{pmatrix}_{i\mu}. \tag{5.10}$$

The ground-state mean field in the quasiparticle basis, $\mathbb{H}_0 = \mathbb{W}^\dagger\mathcal{H}\mathbb{W}$, is therefore diagonal and has the energies of the quasiparticles as the eigenvalues of the upper-left submatrix:

$$\mathbb{H}_0 = \begin{pmatrix} E & 0 \\ 0 & -E \end{pmatrix}, \qquad E = \begin{pmatrix} E_1 & 0 & \cdots \\ 0 & E_2 & \cdots \\ \vdots & \vdots & \ddots \end{pmatrix}. \tag{5.11}$$

5.1.1: HFB calculations with both protons and neutrons

HFB calculations of real nuclei must incorporate both protons and neutrons into their solutions (5.10). In practice one solves two sets of HFB equations simultaneously: one for neutrons with matrices $\mathcal{R}_n$, $\mathcal{H}_n$, etc., and another for protons. The two solutions are coupled by the density functional, which depends on both $\rho_n(\mathbf{r})$ and $\rho_p(\mathbf{r})$ (and also the pairing tensors κ). The density functional that describes protons must also include a term accounting for the Coulomb repulsion among the protons, E_{Coul}.

The most straightforward way to obtain the generalized density for a nucleus with both protons and

neutrons is to combine their respective single-particle states into one set: $[\,c\,]^\dagger \equiv (c_n^\dagger \; c_p^\dagger \; c_n \; c_p)$. We find, however, that the related basis $[\,c\,]^\dagger \equiv (c_n^\dagger \; c_n \; c_p^\dagger \; c_p)$ with neutrons and protons treated separately is more helpful in deriving the pnFAM. In this basis, neglecting the possibility of quasiparticle wave functions that are admixtures of proton and neutron wave functions, we can define a new Bogoliubov supermatrix

$$\mathbb{W} = \begin{pmatrix} \mathbb{W}^{(n)} & 0 \\ 0 & \mathbb{W}^{(p)} \end{pmatrix}, \tag{5.12}$$

with the previously-defined Bogoliubov transformation matrices (5.2) occupying the diagonal blocks. In this basis we can also introduce enlarged generalized densities and HFB mean fields:

$$\mathcal{R} = \begin{pmatrix} \mathcal{R}^{(n)} & \mathcal{R}^{(pn)\dagger} \\ \mathcal{R}^{(pn)} & \mathcal{R}^{(p)} \end{pmatrix}, \qquad \mathcal{H} = \begin{pmatrix} \mathcal{H}^{(n)} & \mathcal{H}^{(pn)\dagger} \\ \mathcal{H}^{(pn)} & \mathcal{H}^{(p)} \end{pmatrix}, \tag{5.13}$$

where the matrices $\mathcal{H}$ are defined as before in Eq. (5.9).

In a typical HFB solution that neglects proton-neutron-mixed wave functions completely, the matrix $\mathcal{R}^{(pn)} = 0$, and the generalized density is block diagonal. Similarly, $\mathcal{H}^{(pn)} = 0$ and the Hamiltonian matrix is block-diagonal as well. The static HFB solution $[\mathcal{H}, \mathcal{R}] = 0$ thus corresponds to the pair of solutions mentioned at the beginning of this section:

$$[\mathcal{H}^{(n)}, \mathcal{R}^{(n)}] = 0, \qquad [\mathcal{H}^{(p)}, \mathcal{R}^{(p)}] = 0. \tag{5.14}$$

We will see that our pnFAM calculations build up the proton-neutron blocks of $\mathcal{R}$ and $\mathcal{H}$; these components of the density and the Hamiltonian matrix will describe the time-dependent oscillations of the nucleus into the excited states which are occupied in β decay.

5.1.2: The ground state solver HFBTHO

Our HFB ground state calculations are carried out using the code HFBTHO, described in Refs. [77, 78], that is slightly modified to interface with our program, PNFAM. The HFBTHO solver provides ground-state solutions for deformed nuclei under the restrictions of time-reversal symmetry, axial symmetry, and reflection symmetry.

Time-reversal symmetry is particularly essential for calculations without spherical symmetry: the time reversal operator reverses angular momentum, connecting degenerate partner states with opposite J_z values. In this way it plays a similar role as spherical symmetry by reducing the number of distinct states which must be treated computationally. The time-reversal symmetry also dictates the form of the U and V matrices [104]

and allows all ground state quantities to be handled without requiring complex numbers [77, 78, 88]. Alongside time-reversal symmetry, the requirement of axial symmetry allows angular integrals to be treated analytically, leaving only double integrals in ρ and z to be handled computationally. Imposing reflection symmetry (i.e., symmetry under a rotation by $180°$ about the x or y axes) allows for integration only over the range $z \in [0, z_{\mathrm{max}}]$.

HFBTHO solves the HFB equations in an harmonic oscillator basis by iterative diagonalization, updating ρ and κ in each iteration until a stable minimum in the energy surface is reached. The solver can calculate the Kohn-Sham mean field $h[\rho]$ from fairly general Skyrme EDFs [78], and uses simple Skyrme-type pairing functionals (i.e. those corresponding to local, contact interactions) to calculate the pairing field Δ. When convergence is reached, we extract and store essential ground-state properties for use in our FAM calculations. In particular, we export the U and V matrices for both protons and neutrons, the quantum numbers of the single-particle basis states, and wave functions and their derivatives. We also export the coupling constants of the EDFs used by HFBTHO in order to verify self-consistency automatically.

Section 5.2:   Overview of the finite amplitude method

As the pnFAM is an extension of the usual finite amplitude method, its derivation follows that of the like-particle FAM, particularly Refs. [98, 105]. (We are also grateful to M. Kortelainen, who shared notes from the parallel development of a new like-particle FAM program [104, 106] that were helpful regarding time reversal, HFBTHO, and the cylindrical geometry of the intrinsic nuclear frame.) M. T. Mustonen worked out most of the original proton-neutron theory [61, 107], and the derivation presented here follows his work. This formulation is somewhat different from the usual treatment in terms of time-dependent quasiparticles $\alpha_\mu^\dagger(t)$, e.g., in Ref. [98]; it is more like the presentation of Ref. [105].

Along the same lines as the original quasiparticle FAM [98], our charge-changing implementation is derived from the linear response of an HFB-type mean field (we have previously reviewed linear response theory in Chapter 4). We generalize the time-dependent HFB to density functional theory and calculate the energy as a functional of the densities $\rho(t)$ and $\kappa(t)$. This is also the context for other FAM calculations, e.g., those of Refs. [98, 105]. Within the adiabatic approximation, the energy is a function of time solely through the densities: $E = E[\rho(t), \kappa(t)]$. The functional dependence of E on the densities is preserved between the ground state and subsequent FAM calculations.

In the time-dependent version of the HFB we must solve the matrix equation

$$i\dot{\mathcal{R}}(t) = [\mathcal{H}[\mathcal{R}(t)] + \mathcal{F}(t), \, \mathcal{R}(t)] \tag{5.15}$$

for the time-dependent generalized density $\mathcal{R}(t)$ under the restriction $\mathcal{R}^2(t) = \mathcal{R}(t)$ [95]. The matrix $\mathcal{R}(t)$ is the time-dependent extension of its static counterpart $\mathcal{R}_0$, and the matrix $\mathcal{F}(t)$ is built up from nuclear matrix elements of some time-dependent external field $\hat{F}(t)$. The linear response approximation to Eq. (5.15) follows from the usual assumption that the field is weak and proportional to a small parameter $\eta \ll 1$. In this limit the time-dependent generalized density can be written as $\mathcal{R}(t) \approx \mathcal{R}_0 + \eta \delta \mathcal{R}(t)$, and the approximation linearizes the TDHFB equation to $\mathcal{O}(\eta)$:

$$i\delta\dot{\mathcal{R}}(t) = [\mathcal{H}_0, \, \delta\mathcal{R}(t)] + [\delta\mathcal{H}(t) + \mathcal{F}(t), \, \mathcal{R}_0]. \tag{5.16}$$

We find that Eq. (5.16) is simply the quasiparticle generalization of the linear response equation (4.9), which did not include pairing correlations. The matrix $\delta\mathcal{H}(t)$ appearing in (5.16) contains the first-order effects of $\delta\mathcal{R}(t)$ on the HFB Hamiltonian $\mathcal{H}[\mathcal{R}]$, and as a result (5.16) must be solved iteratively. The determination of $\delta\mathcal{H}(t)$ takes up the bulk of the computation time in the FAM. With an appropriate choice of basis, the remaining terms are either trivial or remain constant during the iterative procedure.

The main advantage of the FAM is its efficiency compared to the standard technique for obtaining the excited states of a mean field with pairing, the matrix quasiparticle random-phase approximation (QRPA). It is well known that one can obtain the RPA equations from time-dependent Hartree-Fock theory [72, 95, 108], and it is easy to show [61, 72, 95, 97, 98, 107] that the matrix QRPA equations, in which one must explicitly construct and diagonalize a large Hamiltonian matrix formed from the matrix elements of the of nuclear interaction, follow from the linear response equation (5.16). The connection between the two techniques can be demonstrated by expanding $\mathcal{H}[\mathcal{R}(t)]$ from Eq. (5.15) in a Taylor series to first order in η:

$$\mathcal{H}[\mathcal{R}(t)] \approx \mathcal{H}[\mathcal{R}_0] + \eta \frac{\delta\mathcal{H}}{\delta\mathcal{R}}\bigg|_{\mathcal{R}=\mathcal{R}_0} \cdot \delta\mathcal{R}(t) \equiv \mathcal{H}_0 + \eta\delta\mathcal{H}(t). \tag{5.17}$$

The QRPA Hamiltonian matrix requires calculating the $\mathcal{O}(N^2)$ quantities $\delta\mathcal{H}/\delta\mathcal{R}$, but the FAM obtains them implicitly—evaluating $\delta\mathcal{H}(t)$ numerically via finite difference [97]:

$$\delta\mathcal{H}(t) \equiv \frac{\delta\mathcal{H}}{\delta\mathcal{R}}\bigg|_{\mathcal{R}=\mathcal{R}_0} \cdot \delta\mathcal{R}(t) = \frac{\mathcal{H}[\mathcal{R}_0 + \eta\delta\mathcal{R}(t)] - \mathcal{H}[\mathcal{R}_0]}{\eta}. \tag{5.18}$$

In principle, solving the FAM equations therefore requires only one additional mean field calculation per iteration, using the updated density $\mathcal{R}_0 + \eta\delta\mathcal{R}(t)$ in place of $\mathcal{R}_0$. Even in practical applications where many individual FAM solutions are required, essentially any reasonable number of solution results in a much faster calculation than would be obtained with the usual matrix QRPA technique. In practical calculations one usually obtains $\delta\mathcal{R}$ in the frequency domain, which provides solutions for the nuclear response at specific

excitation energies $\hbar\omega$.

5.2.1: Differences between the charge-changing and like-particle FAM

Formally, the main differences between the charge-changing and like-particle versions of the FAM arise from the fundamental difference in character of the external field driving the nuclear excitations. Charge-changing solutions are driven by a time-dependent external field which has the strange property of stimulating neutrons to turn into protons and vice versa. With an external field of this type, $\delta\mathcal{R}^{(pn)}(t)$ is of primary importance. Since we are only interested in charge-changing excitations of the nucleus we do not consider any like-particle FAM motion.[1] If the ground-state solution does not allow proton-neutron-mixed wave functions (as HFBTHO does not), then the charge-changing generalized density $\mathcal{R}_0^{(pn)} \equiv 0$ in the ground state and is purely time-dependent in the pnFAM, stimulated by the external field:

$$\mathcal{R}^{(pn)}(t) = \eta\delta\mathcal{R}^{(pn)}(t) = \eta \begin{pmatrix} \delta\rho_{pn}(t) & \delta\kappa_{pn}(t) \\ -\delta\kappa_{pn}^*(t) & -\delta\rho_{pn}^*(t) \end{pmatrix}. \tag{5.19}$$

As in the like-particle FAM, these density oscillations generate time dependence in the Hamiltonian matrix: $\mathcal{H}[\mathcal{R}(t)] \approx \mathcal{H}_0 + \eta\delta\mathcal{H}(t)$. Because $\mathcal{R}_0^{(pn)}$ vanishes in the ground state solution, so does $\mathcal{H}_0^{(pn)}$ since it is linear in $\mathcal{R}$ for Skyrme functionals [61]. This actually provides a nice simplification in charge-changing calculations: the factor η which multiplies $\delta\mathcal{R}(t)$ and appears in $\delta\mathcal{H}(t)$ cancels out of the finite difference equation (5.18), and we can calculate $\delta\mathcal{H}(t)$ directly without even resorting to finite difference:

$$\delta\mathcal{H}^{(pn)}(t) = \begin{pmatrix} \delta h_{pn}(t) & \delta\Delta_{pn}(t) \\ -\delta\Delta_{pn}^*(t) & -\delta h_{pn}^*(t) \end{pmatrix}. \tag{5.20}$$

The mean field $\delta h_{pn}(t)$, pairing field $\Delta_{pn}(t)$, etc. can be calculated directly in terms of $\rho_{pn}(t)$, $\kappa_{pn}(t)$, and the static densities $\rho_0^{(n)}$ and $\rho_0^{(p)}$ without directly introducing a numerical value for η [61].

Besides the obvious structural differences between the charge-changing and like-particle versions of the FAM (working with $\delta\mathcal{R}^{(pn)}$ instead of $\delta\mathcal{R}^{(n)}$ and $\delta\mathcal{R}^{(p)}$), the calculation of $\delta\mathcal{H}(t)$ is the second major difference between the two techniques. In the pnFAM, this calculation is in one way easier and in another way more difficult than in the like-particle FAM: since the numerical factor η never appears in our final equations [61], we have no need to tune it as did the authors of Ref. [98]. On the other hand, we could not easily adapt a ground-state solver like HFBTHO to carry out charge-changing calculations since the corresponding (isovector)

---

[1] A combined charge-changing/like-particle FAM could find the natural excitation energies and transitions for each mode, and if we allowed for proton-neutron-mixed wave functions in the ground state then a like-particle external field could possibly excite charge-changing modes and vice versa.

part of the Skyrme functional is not fully implemented for ground state calculations with time reversal symmetry. As a result we wrote our program essentially from scratch.

Section 5.3: Solution of the pnFAM equations in the quasiparticle basis

We conclude this chapter by summarizing the derivation of the pnFAM equations and the iterative procedure followed to solve them. We then discuss how to obtain β-decay rates in the pnFAM framework. Additional details are presented in Appendix C.

The pnFAM equations are most simply derived from the linear response equation (5.16) by transforming to the quasiparticle basis using the combined proton-neutron Bogoliubov transformation (5.12), e.g.,

$$\mathbb{R} = \mathbb{W}^\dagger \mathcal{R} \mathbb{W} = \begin{pmatrix} \mathbb{W}^{(n)\dagger} & 0 \\ 0 & \mathbb{W}^{(p)\dagger} \end{pmatrix} \begin{pmatrix} \mathcal{R}^{(n)} & \mathcal{R}^{(pn)\dagger} \\ \mathcal{R}^{(pn)} & \mathcal{R}^{(p)} \end{pmatrix} \begin{pmatrix} \mathbb{W}^{(n)} & 0 \\ 0 & \mathbb{W}^{(p)} \end{pmatrix} = \begin{pmatrix} \mathbb{R}^{(n)} & \mathbb{R}^{(pn)\dagger} \\ \mathbb{R}^{(pn)} & \mathbb{R}^{(p)} \end{pmatrix}. \tag{5.21}$$

The linear response equation then takes the form

$$i\delta\dot{\mathbb{R}}(t) = [\mathbb{H}_0,\, \delta\mathbb{R}(t)] + [\delta\mathbb{H}(t) + \mathbb{F}(t),\, \mathbb{R}_0]. \tag{5.22}$$

Because the generalized density $\mathbb{R}(t)$, Hamiltonian matrix $\mathbb{H}(t)$, and external field $\mathbb{F}(t)$ are all Hermitian (we define $\mathbb{F}(t)$ to be Hermitian), the lower-left and upper-right blocks of these matrices, which contribute to charge-changing calculations, are related by Hermitian conjugation. As a result, the pnFAM equations can be derived using only the proton-neutron (lower-left) blocks of the quasiparticle matrices.

To solve Eq. (5.22) for $\delta\mathbb{R}^{(pn)}(t)$, we need several different quantities. The ground-state generalized density $\mathbb{R}_0$ (5.6) and Hamiltonian matrix $\mathbb{H}_0$ (5.11) are diagonal in the quasiparticle basis and determined by HFBTHO at the ground state. $\mathbb{F}(t)$ is formed from matrix elements of the external field and is an input for the calculation; its form drives the form of the resulting solutions. Finally, $\delta\mathbb{H}(t)$ is the time-dependent change in the Hamiltonian matrix and is calculated at each iteration as a functional of the generalized density $\mathbb{R}_0 + \eta\delta\mathbb{R}(t)$. Because the HFB generalized density is required to have $\mathbb{R}^2(t) = \mathbb{R}(t)$ at all times, the time-dependent change in the generalized density is restricted and must take the form [105]

$$\delta\mathbb{R}^{(pn)}(t) = \begin{pmatrix} 0 & X_{\pi\nu}(t) \\ -X_{\pi\nu}^*(t) & 0 \end{pmatrix}, \tag{5.23}$$

i.e., it is formed from a matrix $X_{\pi\nu}(t)$ where π and ν are proton and neutron quasiparticle matrix indices, respectively. By evaluating the commutators in Eq. (5.22), the linear response equation generates a single set

of time-dependent pnFAM equations,

$$i\dot{X}_{\pi\nu}(t) = (E_\pi + E_\nu)X_{\pi\nu}(t) + \delta H_{\pi\nu}^{20}(t) + F_{\pi\nu}^{20}(t), \tag{5.24}$$

where $F_{\pi\nu}^{20}(t)$ is a proton-neutron matrix element of the external field, $X_{\pi\nu}(t)$ is the change in the proton-neutron density, and $\delta H_{\pi\nu}^{20}(t)$ is the change in the proton-neutron mean field. E_π and E_ν are quasiparticle energies calculated by HFBTHO in the ground state solution.

To obtain a corresponding set of equations which depend on the energy of the nuclear excitation, we make the usual choice of a sinusoidal external field [61, 98, 105]. This choice requires the introduction of six new time-independent matrices multiplying factors $e^{\pm i\omega t}$:

$$X_{\pi\nu}(t) = X_{\pi\nu}(\omega)e^{-i\omega t} + Y_{\pi\nu}^*(\omega)e^{i\omega t}, \tag{5.25a}$$

$$\delta H_{\pi\nu}^{20}(t) = \delta H_{\pi\nu}^{20}(\omega)e^{-i\omega t} + \delta H_{\pi\nu}^{02*}(\omega)e^{i\omega t}, \tag{5.25b}$$

$$F_{\pi\nu}^{20}(t) = F_{\pi\nu}^{20}e^{-i\omega t} + F_{\pi\nu}^{02*}e^{i\omega t}. \tag{5.25c}$$

Inserting these ansatzes into the time-dependent pnFAM equation (5.24), we obtain the corresponding energy-dependent pnFAM equations [61]:

$$X_{\pi\nu}(\omega)[(E_\pi + E_\nu) - \omega] + \delta H_{\pi\nu}^{20}(\omega) = -F_{\pi\nu}^{20}, \tag{5.26a}$$

$$Y_{\pi\nu}(\omega)[(E_\pi + E_\nu) + \omega] + \delta H_{\pi\nu}^{02}(\omega) = -F_{\pi\nu}^{02}. \tag{5.26b}$$

The pnFAM equations are coupled by the functional dependence of the mean field ($\delta H^{20}(\omega)$ and $\delta H^{02}(\omega)$) on the nuclear density ($X(\omega)$ and $Y(\omega)$). They are solved iteratively by applying the proton-neutron Bogoliubov transformation (5.12) to compute new densities ρ and κ from $X(\omega)$ and $Y(\omega)$, which are then used to calculate new mean fields h and pairing fields Δ. These new fields are finally transformed back to the quasiparticle basis, forming new matrices $\delta H^{20}(\omega)$ and $\delta H^{02}(\omega)$ and new solutions $X(\omega)$ and $Y(\omega)$, and the process repeats.

5.3.1: Strength functions, cross-terms, and β-decay half-lives

By solving the pnFAM equations in the quasiparticle basis for $X_{\pi\nu}(\omega)$ and $Y_{\pi\nu}(\omega)$,

$$X_{\pi\nu}(\omega) = -\frac{\delta H_{\pi\nu}^{20}(\omega) + F_{\pi\nu}^{20}}{(E_\pi + E_\nu) - \omega}, \qquad Y_{\pi\nu}(\omega) = -\frac{\delta H_{\pi\nu}^{02}(\omega) + F_{\pi\nu}^{02}}{(E_\pi + E_\nu) + \omega}, \tag{5.27}$$

we obtain the response function of the nucleus to the external field $\mathbb{F}(t)$. We can then define the strength function [72, 97, 98] (cf. Eq. (4.13)):

$$S_F(F;\omega) = -\frac{1}{\pi}\text{Im}\sum_{\pi\nu}\left[F_{\pi\nu}^{20*}X_{\pi\nu}(F;\omega) + F_{\pi\nu}^{02*}Y_{\pi\nu}(F;\omega)\right] = -\frac{1}{\pi}\text{Im Tr}\,\mathbb{F}^{(pn)\dagger}\delta\mathbb{R}^{(pn)}(\omega), \tag{5.28}$$

where $X(\omega)$ and $Y(\omega)$ are computed with an external field generated by the same operator $\hat{F}$ used in the trace. We may also define the pnFAM version of the cross-terms from Chapter 3 by first computing the nuclear response to an operator $\hat{F}$ and subsequently computing the strength function for another operator $\hat{G}$ [61]:

$$S_F(G;\omega) = -\frac{1}{\pi}\text{Im}\sum_{\pi\nu}\left[G_{\pi\nu}^{20*}X_{\pi\nu}(F;\omega) + G_{\pi\nu}^{02*}Y_{\pi\nu}(F;\omega)\right]. \tag{5.29}$$

In the absence of any residual interaction ($\delta\mathbb{H}\to 0$), the strength function has simple poles at the elementary two-quasiparticle excitations of the ground state. One can also show [61, 107, 109, 110] that the total strength function has poles at the normal-mode frequencies of the interacting system:

$$S_F(F;\omega) = -\frac{1}{\pi}\text{Im}\sum_{N}\left(\frac{\left|\langle N\,|\,\hat{F}\,|\,0\rangle\right|^2}{\omega - E_N} - \frac{\left|\langle N\,|\,\hat{F}^\dagger\,|\,0\rangle\right|^2}{\omega + E_N}\right). \tag{5.30}$$

If we move the excitation frequency off the real axis $\omega \to \omega + i\gamma$ to avoid these poles we obtain the familiar Lorentzian strength distribution from Eq. (5.30) [107, 109, 110]:

$$S_F(F;\omega,\gamma) = \frac{\gamma}{\pi}\sum_{N}\left(\frac{\left|\langle N\,|\,\hat{F}\,|\,0\rangle\right|^2}{(\omega - E_N)^2 + \gamma^2} - \frac{\left|\langle N\,|\,\hat{F}^\dagger\,|\,0\rangle\right|^2}{(\omega + E_N)^2 + \gamma^2}\right). \tag{5.31}$$

Because the PNFAM does not produce discrete transition strengths and excitation energies, we cannot directly apply the equations in Chapters 2 and 3 for the total β-decay rate. Instead, as presented in Ref. [61], we take advantage of the fact that the β-decay strength functions $S_F(F;\omega)$ and $S_F(G;\omega)$ have simple poles at the excitation frequencies of the system by applying the calculus of residues. Contour integration methods were first applied to the FAM by Hinohara *et al.* [109, 110].

By folding in analytic approximations to the energetic factors which enter decay-rate computations (the Fermi function F_0 in particular, see Chapter 2 and Appendix A) and computing the β-decay shape factors along a contour chosen to include all excited states compatible with the maximum β-decay energy (Fig. 5.1), we can compute the total β-decay rate for each class of allowed and forbidden transition ($J^\pi = 1^+$, 0^-, 1^-, and 2^-) and each value of the intrinsic angular momentum projection $0 \leq K \leq J$. The total rate is then

34

summed up from these various contributions,

$$\lambda = \sum_{J^\pi} \sum_{K=0}^{J} \lambda_{J^\pi}(K), \tag{5.32}$$

which are given by [61]

$$\lambda_{J^\pi}(K) = -\frac{\ln 2}{\kappa} \frac{1}{2\pi} \mathrm{Im} \sum_i \oint_C p_i(z) \, \mathcal{S}_i(J^\pi, K; z) \, \mathrm{d}z. \tag{5.33}$$

The index i enumerates the various analytic approximations to different energetic factors (as many as six different factors can contribute, as in Ref. [111]), and $\mathcal{S}_i(J^\pi, K; z)$ is an energy-dependent and K-dependent combination of transition strengths and cross-terms which make up a particular type of decay. The quantities $\mathcal{S}$ are essentially the same as the shape factors $\mathcal{C}^{\mathrm{intr}}$ from Chapter 3, and their relation to the pnFAM strength functions and cross-terms are given in the appendix of Ref. [61].
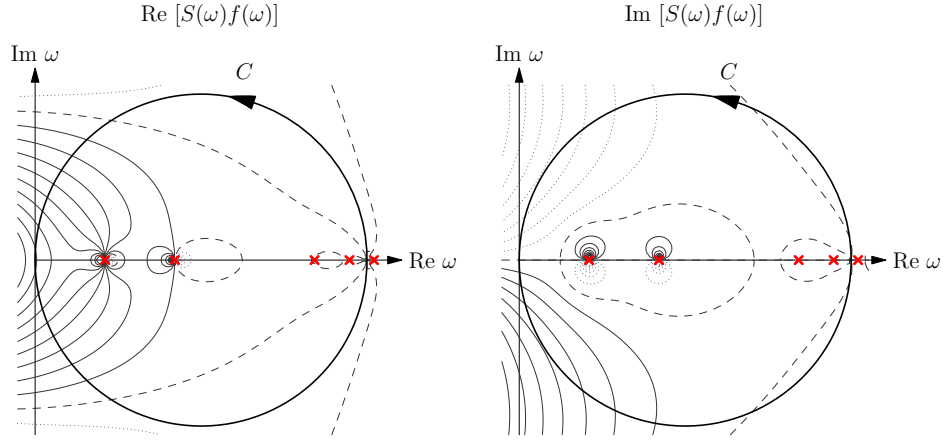
Figure 5.1: Schematic demonstration of the contour C used to compute the total β-decay half-life. The contour is defined in the complex ω plane such that it includes all the poles (marked with red crosses) that are energetically allowed to contribute. This figure demonstrates to behavior of both the real and imaginary parts of the strength function $S(\omega)$ folded with an analytic approximation to the phase space factor $f(\omega)$ as described in Ref. [61]. Reprinted figure with permission from M. T. Mustonen, T. Shafer, Z. Zenginerler, and J. Engel, Phys. Rev. C **90**, 024308 (2014) [61]. Copyright 2014 by the American Physical Society.

CHAPTER 6: β DECAY OF ODD NUCLEI WITH THE PNFAM

In the previous chapter we introduced the proton-neutron finite amplitude method for computing the charge-changing nuclear transitions that enter into β-decay calculations. The pnFAM is based on the time-dependent HFB approximation (TD-HFB) and assumes the nucleus is composed of even numbers of protons and neutrons—the HFB ground state $|\phi\rangle$ is the vacuum to a set of quasiparticles $\alpha_\mu^\dagger$ with the single-particle density $\rho_{ij} = (V^* V^T)_{ij}$. Even-even nuclei make up only about one quarter of the total number of nuclei, so an extension of the pnFAM to odd nuclei (N and/or Z odd) is of great interest [112]. We will show here that the foundations of the pnFAM (linear response theory and the TD-HFB) are general enough to allow just such an extension.

Although 75% of all nuclei have an odd number of either protons or neutrons, there are relatively few calculations of their properties relative to their even-even neighbors. This is a result of the very nature of odd nuclei—because they are built up of odd numbers of nucleons, calculations are especially difficult. As mentioned in Sec. 5.1.2, calculations of nuclear ground states and excited states are tractable as a result of conserved angular momentum and time reversal symmetries. Odd nuclei break these key symmetries, so both the number of states and the number of matrix elements that enter into calculations greatly increase [112].

This increased computational burden requires compromises in the studies that *do* include odd nuclei: at least for large-scale applications, the methods used with even-even nuclei are not feasible. HFB ground state calculations without time reversal or axial symmetry are possible with solvers such as HFODD [113], but these calculations are computationally expensive [77]. Similarly, many calculations of β-decay rates at the QRPA level (which have been around for decades, e.g., Ref. [80]) are still built up from schematic, not self-consistent interactions that are simpler to apply. Another interesting approach we have seen recently is to approximate the mean field of an odd nucleus by the mean field of the neighboring even-even nucleus while constraining the calculation to have the correct odd particle number [58]. This approach allows for calculations of the properties of odd systems within the usual time-even HFB+QRPA (or FAM) formalism.

We have worked out a solution that provides a rigorous way to microscopically calculate the charge-changing properties of odd nuclei approximately while preserving the time reversal symmetry and axial symmetry of the ground state solution. This extension of the pnFAM is based on the equal filling approximation (EFA) [114, 115] to the HFB ground state of an odd nucleus and follows immediately from TD-HFB and linear response equations similar to those in Chapter 5. In the remainder of this chapter we briefly discuss the

equal filling technique for determining the ground state properties of odd nuclei before deriving new pnFAM equations from this approximation.

Section 6.1:   Ground states of odd nuclei and the equal filling approximation

There are many techniques for approximately calculating ground state properties of odd nuclei. These include self-consistent quasiparticle blocking in the HFB [72, 112, 115], where the odd-mass HFB ground state is a one-quasiparticle excitation of an even-even core $\alpha_{\Lambda_0}^\dagger |\phi\rangle$; particle-vibration coupling [116–118] which perturbatively couples the odd nucleon to an even-even core; and simple even-even HFB calculations constrained to an odd number of particles [58]. Of these techniques quasiparticle blocking is the closest match to the even-even methods described in the previous chapter, both for ground state properties and charge-changing transitions derived with linear response theory.[1]

In the quasiparticle blocking approximation (or just "blocking approximation"), the HFB energy is minimized with a set of trial ground states that consist of one-quasiparticle excitations of an even-even core: $|\phi'\rangle = \alpha_{\Lambda_0}^\dagger |\phi\rangle$. The minimization procedure self-consistently determines the properties of the quasiparticles, including the state $\alpha_{\Lambda_0}^\dagger$, in a similar way as in the even-even HFB. The resulting normal and pairing densities (cf. (5.4)) have additional contributions from the one-quasiparticle excitation $\alpha_{\Lambda_0}^\dagger$ [112, 115]:

$$
\begin{aligned}
\rho'_{ij} &= (V^* V^T)_{ij} + U_{i\Lambda_0} U^*_{j\Lambda_0} - V^*_{i\Lambda_0} V_{j\Lambda_0}, \\
\kappa'_{ij} &= (V^* U^T)_{ij} + U_{i\Lambda_0} V^*_{j\Lambda_0} - V^*_{i\Lambda_0} U_{j\Lambda_0}.
\end{aligned}
\tag{6.1}
$$

Formally there are few differences between the even-even and odd calculations, but as mentioned previously the state $|\phi'\rangle$ is not time-even. As a result, the blocking approximation encounters the difficulties described above for odd systems and, without time-reversal symmetry, we cannot calculate properties of these states with a time-even solver such as HFBTHO.

Equal-filling is a clever approximation to quasiparticle blocking that preserves time-reversal symmetry. The EFA replaces the blocking trial state $\alpha_{\Lambda_0}^\dagger |\phi\rangle$ with a mixed state whose density operator is built up equally from the states $|\alpha_{\Lambda_0}^\dagger\rangle$ and $|\alpha_{\bar{\Lambda}_0}^\dagger\rangle$ [112, 115]. Expectation values of one-body operators (e.g., the nuclear density) calculated with the EFA density operator have the form [112]

$$
\langle \hat{M}\rangle^{\mathrm{EFA}} = \frac{1}{2}\left(\langle\phi|\,\alpha_{\Lambda_0} \hat{M} \alpha_{\Lambda_0}^\dagger\,|\phi\rangle + \langle\phi|\,\alpha_{\bar{\Lambda}_0} \hat{M} \alpha_{\bar{\Lambda}_0}^\dagger\,|\phi\rangle \right),
\tag{6.2}
$$

---

[1] Even though the treatment of odd-mass nuclei in the quasiparticle blocking approximation follows naturally from the even-even HFB, this technique is not without problems. It has been shown that standard Skyrme energy-density functionals introduce spurious self-interactions both for single nucleons [119] and for the mean field [116]. These self interactions produce incorrect values for the polarization energy in odd-mass nuclei [116], but it is not clear that they play any role in linear response calculations.

and look like the average of expectation values in the blocked states $\alpha^\dagger_{\Lambda_0}|\phi\rangle$ and $\alpha^\dagger_{\bar{\Lambda}_0}|\phi\rangle$. As a result, the normal and pairing densities in the blocking approximation (6.1) are replaced by the EFA quantities:

$$
\begin{aligned}
\rho^{\text{EFA}}_{ij} &= (V^*V^T)_{ij} + \frac{1}{2}\left(U_{i\Lambda_0}U^*_{j\Lambda_0} + U_{i\bar{\Lambda}_0}U^*_{j\bar{\Lambda}_0} - V^*_{i\Lambda_0}V_{j\Lambda_0} - V^*_{i\bar{\Lambda}_0}V_{j\bar{\Lambda}_0}\right), \\
\kappa^{\text{EFA}}_{ij} &= (V^*U^T)_{ij} + \frac{1}{2}\left(U_{i\Lambda_0}V^*_{j\Lambda_0} + U_{i\bar{\Lambda}_0}V^*_{j\bar{\Lambda}_0} - V^*_{i\Lambda_0}U_{j\Lambda_0} - V^*_{i\bar{\Lambda}_0}U_{j\bar{\Lambda}_0}\right).
\end{aligned}
\tag{6.3}
$$

The authors of Ref. [112] demonstrated the EFA produces the usual HFB equations (with the densities ρ^{EFA} and κ^{EFA}) through a minimization procedure like we described in Chapter 5. They accomplished this formally with a statistical density operator, e.g., [114]

$$
\hat{\rho} = |\phi\rangle\langle\phi| + \sum_\mu \alpha^\dagger_\mu|\phi\rangle p_\mu\langle\phi|\alpha_\mu + \frac{1}{2!}\sum_{\mu\nu}\alpha^\dagger_\mu\alpha^\dagger_\nu|\phi\rangle p_\mu p_\nu\langle\phi|\alpha_\nu\alpha_\mu + \dots,
\tag{6.4}
$$

where the numbers p_μ are "probabilities" of various quasiparticle excitations, such as $\alpha^\dagger_{\Lambda_0}$, being present in the mixture described by $\hat{\rho}$. The EFA is obtained, for a singly-odd nucleus, with the density operator (6.4) by choosing $p_{\Lambda_0} = p_{\bar{\Lambda}_0} = 1$ and all other $p_\mu = 0$. An odd-odd nucleus is described by excitations of one neutron state and one proton state: $p_{\Lambda_\nu} = p_{\bar{\Lambda}_\nu} = p_{\Lambda_\pi} = p_{\bar{\Lambda}_\pi} = 1$. Ref. [112] demonstrated that this mixed-state description of the EFA produces the usual HFB equations $[\mathbb{H}, \mathbb{R}] = 0$:

$$
\begin{pmatrix} h^{\text{EFA}} & \Delta^{\text{EFA}} \\ -\Delta^{\text{EFA}*} & -h^{\text{EFA}*} \end{pmatrix}\begin{pmatrix} U & V^* \\ V & U^* \end{pmatrix} = \begin{pmatrix} E & 0 \\ 0 & -E \end{pmatrix}\begin{pmatrix} U & V^* \\ V & U^* \end{pmatrix}.
\tag{6.5}
$$

The HFB equations may then be solved in the usual way, and the energy is calculated with the EFA densities: $E = E[\rho^{\text{EFA}}, \kappa^{\text{EFA}}]$. This is encouraging from a DFT perspective. We can apply our Skyrme functionals directly with these new time-even densities, which is essentially how HFBTHO applies the EFA to odd nuclei [78].

Although the equal-filling approximation has been applied for some time [112], Refs. [112] and [115] have provided formal justification and computational verification for the procedure. Examining the problem in a computational way, the EFA is only useful if it constitutes a good approximation to the full quasiparticle blocking approximation, and Ref. [115] demonstrates this is certainly true. Quasiparticle energies computed in the EFA deviate from their counterparts in blocking calculations by only about 50 keV with a spread of 100–150 keV. Further, the authors of Ref. [115] noted that the time-even parts of the densities ρ and κ are the same in the two approximations, and so the "EFA density matrices...[correspond] to the time-even functional in which the time-odd polarizations exerted by the odd particle are dynamically switched off". This seems a like reasonable approximation, then, since many ground state quantities are either unaffected or

somewhat affected by time-odd fields [115]. The EFA only completely misses out on properties such as the spin polarization of the nucleus; it takes into account, at least partially, effects that are not exclusively odd under time reversal [112].

Section 6.2:   Excited states of odd nuclei

Many β-decay calculations that treat odd nuclei with the QRPA make a distinction between the "valence" nucleon (the quasiparticle $\alpha^\dagger_{\Lambda_0}$) and the even-even core $|\phi\rangle$. From this point of view, excitations of the core can be treated in more-or-less the usual way, and excitations of the valence nucleon can be computed separately, considering the particle-core interaction perturbatively—see Refs. [80, 120–126], for example. (Refs. [116–118, 127] have also studied both the static and time-dependent polarization of the nucleus due to the influence of an additional nucleon.)

These treatments cleanly separate the contributions of the core and valence nucleon, only mixing the two to first order in the nuclear residual interaction (obtained in DFT from the second derivative of the energy functional: $V[\rho] = \delta^2 E[\rho]/\delta\rho^2$). Linear response theory applied directly to the state $\alpha^\dagger_{\Lambda_0}|\phi\rangle$ or the EFA ensemble would provide a more holistic viewpoint: if we determine the mean field density $\mathbb{R}_0$ of an odd nucleus, whether in the blocking or equal filling approximations, linear response should provide the dynamics of the entire nucleus, including both the valence nucleon and the core. It may also include small additional effects (for example the effect of the even-even core on the valence nucleon) that seem to be neglected in the treatment of, e.g., Refs. [117, 118]. Further, if we find an HFB solution $\mathbb{R}_0$ for an odd nucleus, we should be able to—in principle—calculate the linear response about as easily as we calculated the ground state; this is the essential improvement provided by the FAM.

The connection of the equal filling approximation to a quantum statistical ensemble is the key to our pnFAM calculations of β decay. In an ensemble, expectation values are calculated as traces in Fock space [112, 114, 128], giving the HFB generalized density as:

$$\mathbb{R}_0 = \frac{1}{\mathcal{Z}} \begin{pmatrix} \mathrm{Tr}\,\hat{\rho}\alpha^\dagger\alpha & \mathrm{Tr}\,\hat{\rho}\alpha\alpha \\ \mathrm{Tr}\,\hat{\rho}\alpha^\dagger\alpha^\dagger & \mathrm{Tr}\,\hat{\rho}\alpha\alpha^\dagger \end{pmatrix}, \tag{6.6}$$

where $\mathcal{Z} = \mathrm{Tr}\,\hat{\rho}$. The authors of Ref. [112] noted that the EFA versions of the normal and pairing densities (6.3) for a singly-odd nucleus can be obtained from an HFB generalized density $\mathbb{R}_0$ with the form

$$\mathbb{R}_0^{\mathrm{EFA}} = \begin{pmatrix} f & 0 \\ 0 & 1-f \end{pmatrix}, \qquad f_{\mu\nu} = \delta_{\mu\nu}\left(\frac{p_\mu}{1+p_\mu}\right) = \delta_{\mu\nu} \begin{cases} \frac{1}{2}, & \mu \in \{\Lambda_0, \bar{\Lambda}_0\}, \\ 0, & \mathrm{otherwise.} \end{cases} \tag{6.7}$$

39

An essential point of Ref. [112] is that this statistical framework and the resulting generalized density are, mathematically, a restricted version of the well-known finite-temperature HFB theory [128]. In the EFA, the factors f_μ that represent quasiparticle occupation probabilities [128, 129] must be fixed by hand—in finite-temperature HFB the f_μ are functions of the temperature and are determined during the variation [128].

The main advantage of connecting the EFA to the mathematics of ensembles and the finite-temperature HFB is that finite-temperature linear response theory is well-studied (see, e.g., Refs. [129–137]) and has even been applied to hot β-decay calculations (for example, Refs. [138, 139]). Our derivation of the EFA version of the pnFAM equations follows roughly Refs. [129] and [95], adapting their presentations to our needs.

Ref. [129] describes the linear response in detail for systems with a Hamiltonian acting on states; this formalism is not directly applicable in the framework of DFT, but many of their main points carry over to our application. Even better, the text [95] derives the time-dependent HFB equations for systems described by a statistical operator like that of Eq. (6.4), showing they have the same form as the equations we derived in the previous chapter. As a result, we must solve Eq. (5.22) as before,

$$i\delta\dot{\mathbb{R}}(t) = [\mathbb{H}_0,\, \delta\mathbb{R}(t)] + [\delta\mathbb{H}(t) + \mathbb{F}(t),\, \mathbb{R}_0], \tag{5.22}$$

only now the matrices appearing in (5.22) are computed with the EFA density operator. Our extension of pnFAM to odd nuclei, then, requires two main adjustments: (1) we should use the ground state EFA solutions $\mathbb{H}_0^{\text{EFA}}$ and $\mathbb{R}_0^{\text{EFA}}$ acquired from HFBTHO in place of their even-even counterparts, and (2) the calculation of $\delta\mathbb{R}(t)$ should be reformulated as the trace of a time-dependent version of $\hat{\rho}^{\text{EFA}}$ in Eq. (6.4).

6.2.1: The pnFAM equations for odd nuclei

As shown in Ref. [112], the EFA ground state solution still satisfies the HFB equation $[\mathbb{H}_0^{\text{EFA}}, \mathbb{R}_0^{\text{EFA}}] = 0$. The equal filling approximation changes the character of $\mathbb{R}_0$ slightly (6.7), but the Hamiltonian matrix $\mathbb{H}_0^{\text{EFA}}$ assumes its standard form (5.11), with one-quasiparticle energies along the diagonal. As in the even-even case, HFBTHO does not consider mixed proton-neutron wave functions.

The proton-neutron generalized density $\mathbb{R}^{(pn)}$ is calculated by tracing with the density operator $\hat{\rho}^{\text{EFA}}$, as in Eq. (6.6). Its time dependence can be calculated by following the evolution of $\hat{\rho}^{\text{EFA}}(t)$, which is a result of a time-dependent external field $\hat{F}(t)$:

$$\hat{\rho}^{\text{EFA}}(t) \approx \hat{\rho}_0^{\text{EFA}} + \eta\delta\hat{\rho}^{\text{EFA}}(t). \tag{6.8}$$

Because the generalized density $\mathbb{R}^{\text{EFA}}(t)$ is no longer projective (cf. Eq. (6.7), $\mathbb{R}^2 \neq \mathbb{R}$), the time-dependent proton-neutron generalized density is no longer block-antidiagonal; $\delta\mathbb{R}^{(pn)}(t)$ is formed from two matrices (cf.

Eq. (5.23)):

$$\delta\mathbb{R}^{(pn)}(t) = \begin{pmatrix} P_{\pi\nu}(t) & X_{\pi\nu}(t) \\ -X_{\pi\nu}^*(t) & -P_{\pi\nu}^*(t) \end{pmatrix}. \tag{6.9}$$

Putting everything together and calculating the value of the commutators (5.22), being careful to account for the factors f_μ in the EFA generalized density, gives the time-dependent EFA pnFAM equations:

$$i\dot{X}_{\pi\nu}(t) = (E_\pi + E_\nu)X_{\pi\nu}(t) + (1 - f_\nu - f_\pi)(F_{\pi\nu}^{20}(t) + \delta H_{\pi\nu}^{20}(t)), \tag{6.10a}$$

$$i\dot{P}_{\pi\nu}(t) = (E_\pi - E_\nu)P_{\pi\nu}(t) + (f_\nu - f_\pi)(F_{\pi\nu}^{11}(t) + \delta H_{\pi\nu}^{11}(t)). \tag{6.10b}$$

The indices π and ν correspond to proton and neutron indices, respectively. Eqs. (6.10) are applicable to neutron-odd nuclei $(f_\nu = \frac{1}{2}(\delta_{\nu\Lambda_\nu} + \delta_{\nu\bar{\Lambda}_\nu}))$, proton-odd nuclei $(f_\pi = \frac{1}{2}(\delta_{\pi\Lambda_\pi} + \delta_{\pi\bar{\Lambda}_\pi}))$, and doubly-odd nuclei (both sets can have nonzero values).

To solve Eqs. (6.10) at a specific nuclear excitation energy $\hbar\omega$, we introduce the frequency-dependent ansatzes

$$P_{\pi\nu}(t) = P_{\pi\nu}(\omega)e^{-i\omega t} + Q_{\pi\nu}^*(\omega)e^{i\omega t}, \tag{6.11a}$$

$$X_{\pi\nu}(t) = X_{\pi\nu}(\omega)e^{-i\omega t} + Y_{\pi\nu}^*(\omega)e^{i\omega t}. \tag{6.11b}$$

Taking the appropriate time derivatives in Eqs. (6.10) yields the energy-dependent pnFAM equations implemented in our program:

$$X_{\pi\nu}(\omega)[(E_\pi + E_\nu) - \omega] = -(1 - f_\nu - f_\pi)[F_{\pi\nu}^{20} + \delta H_{\pi\nu}^{20}(\omega)], \tag{6.12a}$$

$$Y_{\pi\nu}(\omega)[(E_\pi + E_\nu) + \omega] = -(1 - f_\nu - f_\pi)[F_{\pi\nu}^{02} + \delta H_{\pi\nu}^{02}(\omega)], \tag{6.12b}$$

$$P_{\pi\nu}(\omega)[(E_\pi - E_\nu) - \omega] = -(f_\nu - f_\pi)[F_{\pi\nu}^{11} + \delta H_{\pi\nu}^{11}(\omega)], \tag{6.12c}$$

$$Q_{\pi\nu}(\omega)[(E_\pi - E_\nu) + \omega] = -(f_\nu - f_\pi)[F_{\pi\nu}^{\overline{11}} + \delta H_{\pi\nu}^{\overline{11}}(\omega)]. \tag{6.12d}$$

The matrices $X(\omega)$ and $Y(\omega)$ are defined similarly to their even-even versions, but their matrix elements are reduced by a factor $1 - f = 1/2$ when one of the indices π, ν denotes a "blocked" level (i.e., one of the "odd" quasiparticle levels $\alpha_{\Lambda_0}^\dagger$ or $\alpha_{\bar{\Lambda}_0}^\dagger$). Their matrix elements vanish if both quasiparticle indices are blocked. We also have additional, very sparse matrices $P(\omega)$ and $Q(\omega)$ that have non-zero matrix elements when exactly one of the proton and neutron levels is blocked. $F_{\pi\nu}^{11}$ and $F_{\pi\nu}^{\overline{11}}$ are additional matrix elements of the external field $\hat{F}$ in the quasiparticle basis, and $\delta H^{11}(\omega)$ and $\delta H^{\overline{11}}(\omega)$ are additional matrix elements of the proton-neutron mean field.

Generally speaking, the four matrices $\delta H(\omega)$ are coupled together by the densities ρ and κ and their dependence on $P(\omega)$, $Q(\omega)$, $X(\omega)$, and $Y(\omega)$. The pnFAM equations for odd nuclei are solved iteratively in a similar way as their even-even counterparts, and their solutions make up the response function. The transition strength is still calculated with Eq. (5.28), but the trace now includes the matrices $P_{\pi\nu}(\omega)$ and $Q_{\pi\nu}(\omega)$:

$$S_F(F;\omega) = -\frac{1}{\pi}\sum_{\pi\nu}\left[F_{\pi\nu}^{11*}P_{\pi\nu}(\omega) + F_{\pi\nu}^{20*}X_{\pi\nu}(\omega) + F_{\pi\nu}^{02*}Y_{\pi\nu}(\omega) + F_{\pi\nu}^{\overline{11}*}Q_{\pi\nu}(\omega)\right]. \tag{6.13}$$

Section 6.3:   Interpretation of our results for odd nuclei

Because the equal filling approximation describes odd nuclei as a statistical ensemble, the meaning of our results should be carefully considered. Our interpretation of the odd pnFAM strength function follows from Eq. (6.2): since the strength functions are ensemble averages of one-body operators, our results can be written formally as

$$S_{F_K}^{\text{EFA}}(\omega) = \frac{1}{2}\left[S_{F_K}^{\Lambda_0}(\omega) + S_{F_K}^{\bar{\Lambda}_0}(\omega)\right], \tag{6.14}$$

i.e., our computed strength functions (for an operator F that changes the z component of angular momentum by an amount K) are an average of the strength computed from the states $\alpha_{\Lambda_0}^\dagger|\phi\rangle$ and $\alpha_{\bar{\Lambda}_0}^\dagger|\phi\rangle$.

When the operator F does not change the intrinsic z projection, i.e., $K = 0$, the two terms on the right-hand side of Eq. (6.14) produce equivalent strength functions. This is not true when $K \neq 0$, but it turns out that we need transition strengths from intrinsic states with $K < 0$ in our β-decay calculations. The connection between lab-frame and intrinsic-frame transitions (3.10) introduced additional intrinsic-frame contributions to the strength function: we found that the lab-frame transition strength that describes a transition between rotation bands $K_i \to K_f$ is related to the pair of intrinsic transitions $K_i \to K_f$ and $-K_i \to K_f$ as long as the operator F can connect the two intrinsic states.

Consider as an example the $J^\pi = 1^+$ β-decay from a rotation band with $K = 1/2$. According to Eq. (3.10) the following intrinsic transitions are involved:

$$|\langle 1/2\,|\,F_{K=0}\,|\,1/2\rangle|^2, \qquad |\langle 1/2\,|\,F_{K=1}\,|-1/2\rangle|^2,$$
$$|\langle 3/2\,|\,F_{K=1}\,|\,1/2\rangle|^2. \tag{6.15}$$

With the above considerations for the strength function S_{F_K}, we see that the the total 1^+ strength function,

$$S_{\text{total}}(\omega) = S_{F_{K=0}}^{\text{EFA}}(\omega) + 2S_{F_{K=1}}^{\text{EFA}}(\omega), \tag{6.16}$$

includes all the required transitions. For an example with a slight twist, consider a $J^\pi = 2^-$ decay from

a rotation band with $K = 3/2$. An operator that has angular momentum $J = 2$ can connect bands with K-values differing by as much as ± 2, and the required intrinsic transition strengths for this decay are:

$$
\begin{aligned}
&\left| \langle 3/2 \, | \, F_{K=0} \, | \, 3/2 \rangle \right|^2 , \\
&\left| \langle 5/2 \, | \, F_{K=1} \, | \, 3/2 \rangle \right|^2 , \\
&\left| \langle 7/2 \, | \, F_{K=2} \, | \, 3/2 \rangle \right|^2 , \\
&\left| \langle 1/2 \, | \, F_{K=-1} \, | \, 3/2 \rangle \right|^2 , \qquad \left| \langle 1/2 \, | \, F_{K=2} \, | -3/2 \rangle \right|^2 .
\end{aligned}
\tag{6.17}
$$

Here we have a different situation—(6.17) requires a $K = -1$ transition from the $K = 3/2$ initial state. However, due the time-reversal symmetry of $| \phi \rangle$ in equal-filling, this transition strength is related to the strength with all angular momenta reversed:

$$
\left| \langle 1/2 \, | \, F_{K=-1} \, | \, 3/2 \rangle \right|^2 = \left| \langle -1/2 \, | \, F_{K=1} \, | -3/2 \rangle \right|^2 .
\tag{6.18}
$$

The total pnFAM strength function for 2^- decays,

$$
S_{\text{total}}(\omega) = S^{\text{EFA}}_{F_{K=0}}(\omega) + 2 S^{\text{EFA}}_{F_{K=1}}(\omega) + 2 S^{\text{EFA}}_{F_{K=2}}(\omega),
\tag{6.19}
$$

includes all the necessary transitions.

In this way we obtain the transition strength for odd nuclei as simply as for even nuclei. Our EFA-based pnFAM calculations represent a trade-off, exchanging a unique fully polarized ground state for a partially polarized ensemble. This ensemble simulates time-odd polarization without giving up time-reversal invariance and while including at least some polarization effects in the ground state [112]. The time-odd fields that appear in the pnFAM, and consequently should appear in the mean field of an odd nucleus in the blocking approximation, are neglected in the EFA ground state. Using the EFA as a basis for linear response calculations is a very good compromise and a step forward in the mean field description of odd nuclei.

CHAPTER 7: β-DECAY HALF-LIVES OF RARE-EARTH ISOTOPES

Having detailed the theory and computational techniques that we have developed alongside M. T. Mustonen to improve β-decay calculations, we turn to the details and the results of the calculations themselves. As introduced in Chapter 1, we have computed β-decay half-lives of neutron-rich r-process nuclei in two well-separated regions of the nuclear chart: nuclei with mass number $A \simeq 80$ and charge number $Z < 50$, and nuclei in the rare-earth region ($A \simeq 160$, $Z \gtrsim 50$). In this chapter we present results for the larger of the two calculations: the study of well-deformed rare-earth nuclei. Our methods are particularly well suited to these calculations: the rare-earth nuclei of interest are mostly found mid shell and should be well deformed as a result [73].

Section 7.1: The rare-earth r-process nuclei

Unlike the three primary r-process abundance peaks, the rare-earth element (REE) peak is not caused directly by the neutron capture properties of closed-shell nuclei. The primary r-process peaks are formed essentially during the $(n, \gamma) \rightleftarrows (\gamma, n)$ equilibrium as isotopic abundances pile up at $N = 50$, 82, and 126. It has been shown for a hot r process (distinguished by a long $(n, \gamma) \rightleftarrows (\gamma, n)$ equilibrium that persists until essentially all the free neutrons have been depleted [140]) that the REE peak is actually formed during the freeze-out phase—when β decay and n capture occur in roughly equal amounts, and the extremely neutron-rich r-process material formed at the beginning of the r process begins to decay towards stability [18]. The peak forms as a result of a local maximum in nuclear deformation that produces a "kink" in curves of constant neutron separation energy S_n. As laid out in Ref. [20], if there is a kink in this curve near $A \sim 160$, and if the r-process path traverses this region while neutron capture continues at roughly the same rate as β decay, then a REE peak can form as the difference in neutron separation energies "funnels" nuclei into the peak region.

Mumpower et $al.$ [20] have shown that a rare-earth peak can also be formed in cold r-process scenarios where the temperature or density drops quickly and the $(n, \gamma) \rightleftarrows (\gamma, n)$ equilibrium does not persist. In these situations photo-dissociation is frozen out, and the r-process path is determined by the interplay of β decay and neutron capture. The REE peak is then formed from a neutron-capture effect: if the r-process path traverses a region of slower neutron-capture rates than material above and below, material can become "trapped" in the peak region.

These two mechanisms are sensitive to somewhat different sets of β-decay half-lives: a cold r process tends to populate nuclei further from stability than a hot r process [19]. The most important isotopes for a particular process are identified by performing sensitivity studies (Refs. [25, 62, 140, 141] demonstrate this technique for β decay, neutron capture, and nuclear masses), which quantify the effect of a change in, e.g., a β-decay half-life on astrophysical abundances. A typically-used metric is the quantity

$$F_K(Z, N) = 100 \times \sum_A \left| Y^K(A) - Y^b(A) \right|, \tag{7.1}$$

which measures the change in abundances $Y^K(A)$ relative to baseline $Y^b(A)$ when the β-decay rate of a particular nucleus with Z protons and N neutrons is changed by a factor K [62]. The results of such a study for rare-earth nuclei are presented in Fig. 7.1, courtesy of M. Mumpower [62]. The figure includes sensitivity measures for three different r-process scenarios: a hot r process, a cold r process, and a neutron star merger.

Following these sensitivity studies, we have computed half-lives for the seventy rare-earth nuclei listed in Table 7.1. We have also repeated the calculation several times, applying a variety of Skyrme EDFs that we have tailored to reproduce experimentally-measured half-lives in this mass region. The placement of these nuclei on the nuclear chart is shown in Fig. 7.2.

Z	Isotopes
50	^{150}Sn, ^{152}Sn
51	^{151}Sb, ^{153}Sb
52	^{150}Te, ^{152}Te, ^{154}Te, ^{156}Te, ^{158}Te
53	^{151}I, ^{153}I, ^{155}I, ^{157}I, ^{159}I
54	^{148}Xe, ^{150}Xe, ^{152}Xe, ^{154}Xe, ^{156}Xe, ^{158}Xe, ^{160}Xe, ^{162}Xe, ^{164}Xe, ^{166}Xe
55	^{157}Cs, ^{159}Cs, ^{161}Cs, ^{163}Cs, ^{165}Cs, ^{167}Cs
56	^{156}Ba, ^{158}Ba, ^{160}Ba, ^{162}Ba, ^{164}Ba, ^{166}Ba, ^{168}Ba, ^{170}Ba, ^{172}Ba, ^{174}Ba
57	^{163}La, ^{165}La, ^{167}La, ^{169}La, ^{171}La, ^{173}La, ^{175}La
58	^{160}Ce, ^{164}Ce, ^{166}Ce, ^{168}Ce, ^{170}Ce, ^{172}Ce, ^{174}Ce, ^{176}Ce
59	^{171}Pr, ^{173}Pr, ^{175}Pr, ^{177}Pr
60	^{164}Nd, ^{166}Nd, ^{172}Nd, ^{174}Nd, ^{176}Nd, ^{178}Nd
61	^{179}Pm
62	^{178}Sm, ^{180}Sm
64	^{178}Gd, ^{180}Gd

Table 7.1: The seventy rare-earth r-process nuclei for which we compute β-decay half-lives, including forty-five even-even nuclei and an additional twenty-five proton-odd nuclei.

Section 7.2:   Overview of the calculation

A good part of this chapter describes our adjustments of the Skyrme EDFs to optimize our calculations for this mass region. In order to calculate the half-lives of *these particular nuclei* as accurately as possible,
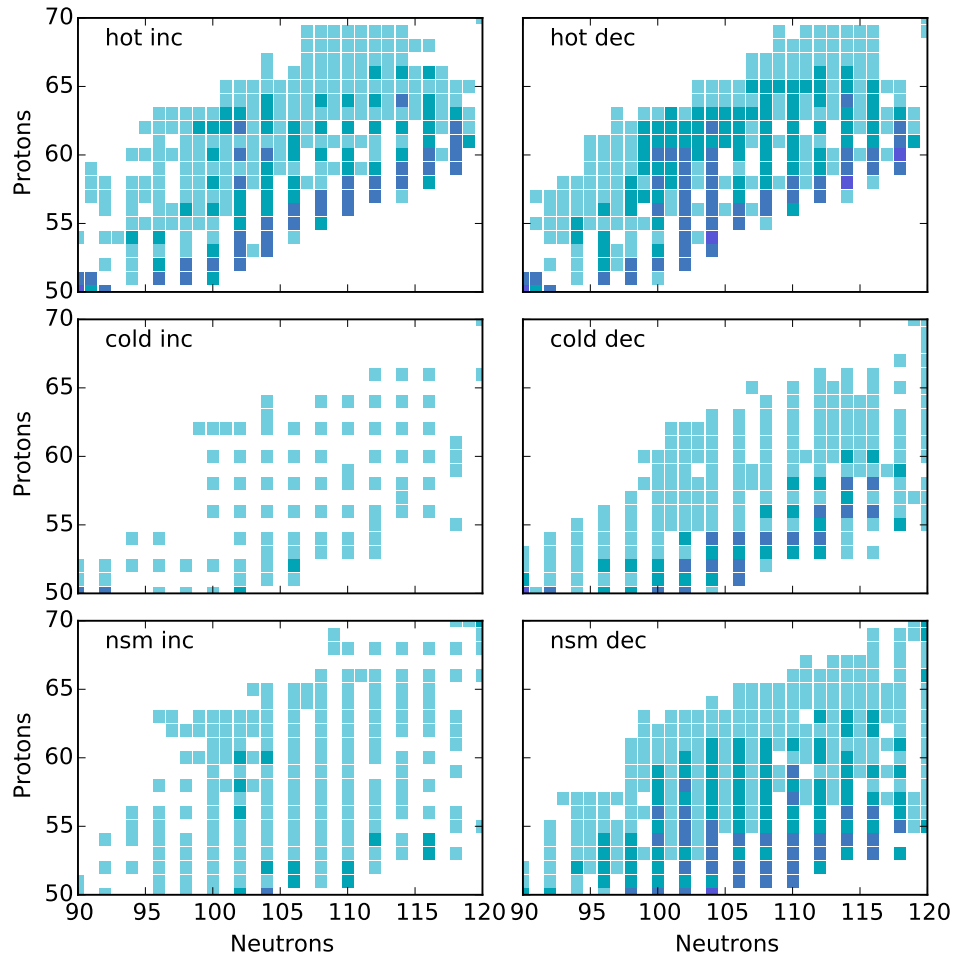
Figure 7.1: Sensitivity of r-process abundances to increases ("inc") and decreases ("dec") of individual rare-earth β-decay rates by a factor of 5. The most darkly shaded nuclei produced the largest effects. The figure is courtesy of M. Mumpower [62] and includes results for three r-process trajectories: a hot r process, a cold r process, and a neutron star merger.
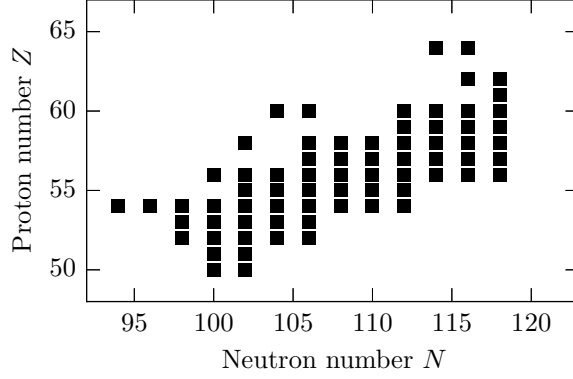
Figure 7.2: The locations on the nuclear chart (cf. Fig. 1.1) of the seventy rare-earth nuclei listed in Table 7.1.

we tune the functionals to reproduce experimentally measured properties of nuclei that are as near to the important nuclei as possible (this is in contrast with the global calculations of Möller *et al.* [55]).

As mentioned earlier, in calculations that include pairing correlations Skyrme EDFs are usually split into two pieces, a particle-hole part and a pairing part:

$$E[\rho, \kappa] = E_{\text{Sk}}[\rho] + E_{\text{pair}}[\rho, \kappa]. \tag{7.2}$$

$E_{\text{Sk}}[\rho]$ generates the mean field of the nucleus ($h_{ij} = \delta E/\delta \rho_{ji}$), and $E_{\text{pair}}[\rho, \kappa]$ describes the pairing correlations among the nucleons ($\Delta_{ij} = \delta E/\delta \kappa_{ij}^*$). We adjust each of these functionals separately to relevant nuclear data.

Our particle-hole functional $E_{\text{Sk}}[\rho]$ is the standard Skyrme EDF described briefly in Chapter 4 and very thoroughly in, e.g., Ref. [88]. Recall that the functional can be split into parts, e.g.,

$$E_T^{\text{even/odd}}[\rho] = \int H_T^{\text{even/odd}}(\mathbf{r}) \, d\mathbf{r}, \tag{7.3}$$

and the labels T (which can equal 0 or 1) and "even/odd" describe the properties of the local densities which make up the $H_T(\mathbf{r})$. The isovector ($T = 1$) terms control β-decay properties, but both $T = 0$ and $T = 1$ components are involved in ground state calculations. On the other hand, in our time-even ground state calculations all time-odd densities vanish and $H_T^{\text{odd}}(\mathbf{r})$ is completely inactive. The time-odd densities are crucial, however, for an accurate description of β-decay transitions.

Because only the time-even part of the Skyrme functional is active in ground state calculations, fits of Skyrme functionals (or, historically, Skyrme two-body interactions) to nuclear data only determine values of the coupling constants in $H_T^{\text{even}}(\mathbf{r})$. (We should note that there has been at least one recent attempt to use both ground state and β-decay data to parameterize a Skyrme two-body interaction [142, 143].) From the

viewpoint of density functional theory, it is not sensible to determine $H_T^{\text{odd}}(\mathbf{r})$ by only considering time-even data. Rather, we adjust $E_{\text{Sk}}[\rho]$ in the following way: We take the time-even parts of the functional or interaction as given since they were fit to nuclear data that are affected by the time-even part of the functional (e.g., masses, radii, or unpolarized nuclear matter [144]). We then adjust the time-odd part of the functional (specifically the time time-odd, isovector part $H_1^{\text{odd}}(\mathbf{r})$ that affects β decay) to charge-changing nuclear data. These fits do not spoil self-consistency since H^{odd} does not contribute to mean field calculations in even-even nuclei.[1] In this way we hope to preserve the best parts of the original fits while optimizing the pieces that are essentially unconstrained.

For $E_{\text{pair}}[\rho, \kappa]$ we choose the pairing functional implemented in the solver HFBTHO [77, 78], which uses a standard Skyrme pairing functional corresponding to the pairing interaction [78]

$$V_{\text{pair}}^{(n,p)}(\mathbf{r}, \mathbf{r}') = V_{(n,p)} \left(1 - \alpha \frac{\rho_0(\mathbf{r})}{\rho_c}\right) \delta(\mathbf{r} - \mathbf{r}'), \tag{7.4}$$

where $\rho_c = 0.16 \text{ fm}^{-3}$ is the saturation density of nuclear matter and $\alpha \in [0, 1]$ controls the mixture of density-dependence. We have extended this interaction in PNFAM to include a proton-neutron mixing (isoscalar) pairing term that would vanish in HFBTHO:

$$V_{\text{pair}}(\mathbf{r}, \mathbf{r}') = (V_0 \hat{\Pi}_{T=0} + V_1 \hat{\Pi}_{T=1}) \left(1 - \alpha \frac{\rho_0(\mathbf{r})}{\rho_c}\right) \delta(\mathbf{r} - \mathbf{r}'). \tag{7.5}$$

In PNFAM we take $V_1 = (V_n + V_p)/2$, but V_0 is a free parameter that strongly affects β-decay rates. The individual proton and neutron pairing strengths are free parameters we adjust during ground state calculations.

The speed and efficiency of the FAM allow us to compute the half-lives of many nuclei and also to repeat these calculations with a variety of Skyrme EDFs. This allows us to get a sense of the variation among functionals and helps to reject particularly unsatisfactory parameterizations. To this end we have selected four Skyrme functionals from different "families": SkO$'$ [145], SV-min [146], SLy5 [147], and UNEDF1-HFB [148] (a recent re-fit of the functional UNEDF1 [149], which was originally fit incorporating a different treatment for pairing correlations than we use here). SV-min and UNEDF1-HFB stand out as particularly recent parameterizations, and they were fit directly as density functionals. Additionally the SkO$'$ parameterization has been applied in previous β-decay calculations at UNC [60, 61, 150], and we have included the Skyrme interaction SLy5 as something of an outlier—it produces less collective Gamow-Teller (allowed β-decay) transition strength than other Skyrme interactions [151] and might be a good example of the variation we

---

[1] As mentioned at the end of Chapter 6, our ground state calculations do not include time-odd components in the mean field either.

can expect among functionals. We have applied the time-even parts of these functionals as provided except for a slight tweak to SV-min, which was originally fit with a code that allowed separate masses for protons and neutrons.

We note that in both our rare-earth and $A \simeq 80$ calculations these adjustments were completed well before we had extended the pnFAM to odd nuclei. As a result our Skyrme EDFs have only been tuned to the β-decay properties of even-even nuclei. Test calculations have shown (as will be demonstrated for our $A \simeq 80$ calculations in the the next chapter) that we represent odd-mass nuclei nearly as well as their even-even neighbors. These are nice confirmations of our pnFAM-EFA method.

Section 7.3: Adjustments to and evaluation of ground state properties

Ground state calculations are foundational to our later calculations of β-decay half-lives, since they determine (among other things) the pairing properties, Q values, and excitation energies of the nucleus. As touched on above, the parts of the nuclear EDF (at least the particle-hole parts) that determine ground-state properties are fixed during the fitting procedure, but the pairing functional is usually left to be adjusted later. As a result we must fix the strengths of the proton and neutron pairing interactions now, before computing the ground states of our target rare-earth nuclei.

First, however, we comment on the main computational parameters (e.g., the basis and integration mesh sizes) that carry through both our HFBTHO and PNFAM calculations, since these must be selected before our ground state calculations as well. We have chosen these parameters following loosely those reported in large-scale calculations with HFBTHO, e.g., the UNEDF series of Skyrme EDF fits [144, 149, 152], as well as the default values [78]. Specifically, we have chosen a spherical harmonic oscillator basis that includes 16 oscillator shells in our calculations (this value was also chosen for a previous calculation of ours [61]), reduced from the 20 shells in the UNEDF fits. This choice significantly speeds up our already efficient PNFAM calculations, lowering the CPU time by a factor of approximately 3. We have also chosen smaller integration meshes than the default in HFBTHO calculations: 30 mesh points for integrations along the z and ρ directions, and 60 points for the Coulomb potential. These values represent 3/4 of the default HFBTHO values [78]. Once these parameters are set, they remain fixed throughout our ground state and β-decay calculations.

Now, in terms of pairing properties our selected Skyrme functionals can be grouped into two categories: those EDFs for which the pairing strengths V_p and V_n are not already determined (SkO$'$ and SLy5), and those EDFs for which the pairing properties were fit along with the particle-hole properties (SV-min and UNEDF1-HFB). Because the functional UNEDF1-HFB was fit using the code HFBTHO, it is simplest (although more computationally expensive, since it was fit in a space of 20 oscillator shells) to use the pairing properties as-provided. This is the method we have adopted for UNEDF1-HFB, and all calculations with this EDF were

carried out in 20 oscillator shells. The application of SV-min is more complicated since it was fit in a slightly different scheme (Hartree-Fock plus BCS pairing) with a different quasiparticle energy cutoff than we can apply in HFBTHO. As a result, we have chosen to re-fit the pairing strengths V_p and V_n for SV-min while keeping the same density-dependent form (i.e., using the same value for α in Eq. (7.4) as in the original fit).

7.3.1: Adjustment of the pairing functional

Pairing strengths are typically fixed by comparing the average HFB pairing gap [77, 153],

$$\bar{\Delta}_{\mathrm{HFB}} = \frac{\mathrm{Tr}\,\Delta\rho}{\mathrm{Tr}\,\rho},\tag{7.6}$$

to the odd-even binding energy differences of nearby nuclei. These differences are estimated using the experimental measure $\tilde{\Delta}^{(3)}$ which has been applied in the UNEDF parameterizations [144, 149, 152], e.g.,

$$\tilde{\Delta}_n^{(3)}(Z,N) = \frac{1}{2}\left[\Delta_n^{(3)}(Z,N+1) + \Delta_n^{(3)}(Z,N-1)\right],\tag{7.7}$$

where $\Delta^{(3)}$ is the traditional three-point mass formula [154, 155] for nuclear binding energies ($B < 0$):

$$\Delta_n^{(3)}(Z,N) = \frac{(-1)^{(Z+N)}}{2}\left[B(Z,N+1) + B(Z,N-1) - 2B(Z,N)\right].\tag{7.8}$$

We have calculated $\tilde{\Delta}^{(3)}$ for 19 nuclei near our region of interest; the results are listed in Table 7.2. These values were computed using atomic mass excesses from the 2012 Atomic Mass Evaluation [156, 157] and subtracting the electronic binding-energy contributions [144] from the atomic binding energies [158] using the formula in Ref. [157]. We propagated the uncertainties reported in the Atomic Mass Evaluation to obtain corresponding uncertainties in $\tilde{\Delta}^{(3)}$. We then applied HFBTHO to determine the values of V_p and V_n that satisfied the corresponding 1-σ uncertainty bounds.[2] Mapping the resulting asymmetric uncertainties in the pairing strength, $V_q + \sigma_q^{(+)} - \sigma_q^{(-)}$, onto a roughly equivalent symmetric set $V_q \pm \bar{\sigma}_q$ [6], we fit average values of the proton and neutron pairing strengths that incorporate all 19 nuclei. Our final pairing strengths, along with the density dependence α (set to 0.5 if not previously specified), are listed in Table 7.3. If our calculated ground-state shapes differed from the previous Skyrme HFB calculations in Ref. [159], we checked that our fitted pairing strengths did not change significantly if we change the shape of our ground state solutions.

---

[2]We are grateful to N. Schunck for providing us with a bisection solver, which we have adapted to version 2 of HFBTHO.

Z	N	$\tilde{\Delta}_{\mathrm{p}}^{(3)}$ (MeV)	$\tilde{\Delta}_{\mathrm{n}}^{(3)}$ (MeV)
52	84	0.79096 ± 0.00464	0.75491 ± 0.0024
54	86	0.90975 ± 0.01527	0.87276 ± 0.0022
56	90	0.92059 ± 0.01093	0.92025 ± 0.0204
58	90	0.99503 ± 0.00975	0.97777 ± 0.0092
60	92	0.68605 ± 0.01176	0.77895 ± 0.0298
62	94	0.57543 ± 0.02887	0.67368 ± 0.0042
62	96	0.55867 ± 0.05021	0.58183 ± 0.0049
64	96	0.57608 ± 0.00276	0.67969 ± 0.0018
66	98	0.53795 ± 0.00277	0.67866 ± 0.0016
68	100	0.55392 ± 0.00312	0.64734 ± 0.0017
68	102	0.50391 ± 0.03646	0.60222 ± 0.0021
70	104	0.52725 ± 0.00300	0.53483 ± 0.0017
72	106	0.62796 ± 0.00168	0.63470 ± 0.0016
72	108	0.62486 ± 0.00388	0.57799 ± 0.0022
74	110	0.55784 ± 0.00199	0.66483 ± 0.0008
74	112	0.60795 ± 0.01224	0.70165 ± 0.0013
74	114	0.67773 ± 0.03607	0.79595 ± 0.0227
76	116	0.78248 ± 0.01110	0.83218 ± 0.0020
78	118	0.75364 ± 0.00128	0.88139 ± 0.0009

Table 7.2: Even-even nuclei used to fit the pairing strengths V_{p} and V_{n}. The odd-even mass indicators $\tilde{\Delta}^{(3)}$ are described in the text.

Functional	V_{p} (MeV fm^3)	V_{n} (MeV fm^3)	α
SkO$'$	-270.0	-243.0	0.5
SV-min	-374.0	-322.0	0.75618
SLy5	-327.0	-298.0	0.5
UNEDF1-HFB	$-260.437\ldots$	$-234.380\ldots$	0.5

Table 7.3: Values of the pairing strength and density dependence used in our rare-earth calculations. The value of α for SV-min, as well as all three pairing parameters for UNEDF1-HFB, were not changed.

7.3.2: Calculated ground state properties

Having fully determined the parts of the Skyrme EDF that affect ground state properties, there are two key ground-state quantities that we examine to assess our calculations: the ground state deformation and the β-decay Q value. We consider the deformation here first. Previous calculations have found the rare-earth nuclei to be strongly prolate [159], and the rare-earth r-process peak is thought to be a consequence of a local maximum in the nuclear deformation [18]. Although our primary focus is on excited states (β-decay transitions), it would be nice to at least approximately reproduce these ground state results, especially since strong disagreement in nuclear shapes could indicate problems with our EDFs or calculations.

For axially- and reflection-symmetric nuclei, the nuclear shape is usually quantified by a single parameter, the quadrupole deformation β. A textbook multipole expansion of the nuclear radius up to quadrupole order gives the nuclear radius as [72, 73, 75]

$$R(\theta, \phi) = R_0 \left[1 + \beta Y_{20}(\theta, \phi) \right].$$

(7.9)

Nuclei with $\beta = 0$ are spherical, those with $\beta > 0$ are prolate (taller than they are wide), and those with $\beta < 0$ are oblate (wider than they are tall). We have sketched these deformations in Fig. 7.3. We have also calculated the ground state shapes of quite a few even-even nuclei in this region and plotted their quadrupole deformations in Fig. 7.4. The results are encouraging: all four Skyrme parameterizations show a prolate deformation maximum near $Z = 60$ and $N = 100$. Although there is variation among EDFs, especially in the transition region between prolate and spherical or oblate shapes, most rare-earth nuclei are described as strongly prolate in our calculations.

Spherical ($\beta = 0$) Prolate ($\beta > 0$) Oblate ($\beta < 0$)
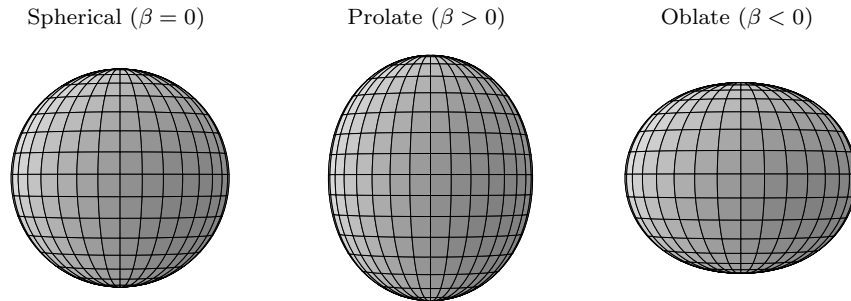
Figure 7.3: Schematic demonstration of the three classes of nuclear shapes allowed in our calculations as a function of the quadrupole deformation parameter β (Eq. (7.9)).

Our values of β are obtained directly from HFBTHO by trial and error. The solver allows us to temporarily constrain the shape of the nucleus at the beginning of a calculation so that by selecting a prolate, oblate,
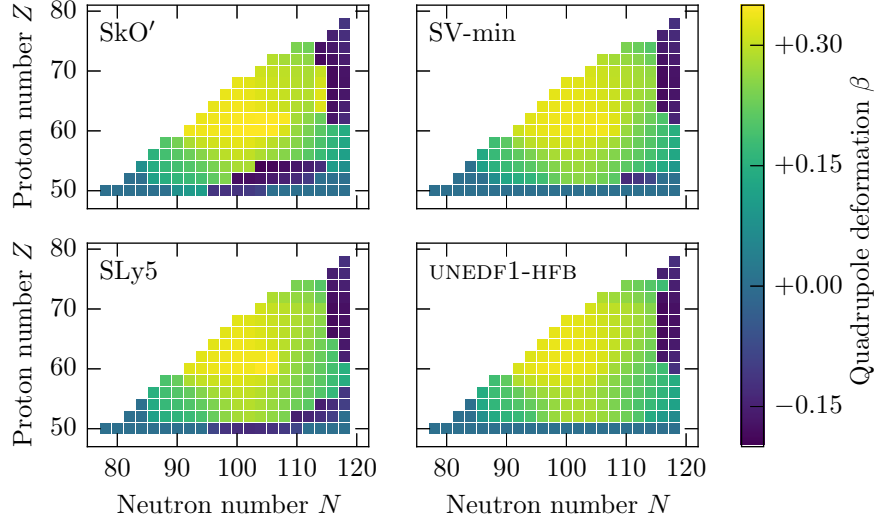
Figure 7.4: Ground state quadrupole deformations β obtained with HFBTHO for even-even nuclei using the energy-density functionals (a) SkO′, (b) SV-min, (c) SLy5, and (d) UNEDF1-HFB. A prolate deformation maximum is clearly visible with $Z \approx 60$ and $100 \leq N \leq 110$.

or spherical shape we can "pull" the ground state solution in a given direction. Some nuclei may have only one local minimum of the energy as a function of β, but many have minima at both prolate and oblate deformations. The correct ground state of the nucleus is chosen to be the most-bound of the candidates; for a well-deformed nucleus the energy difference between the the two or three candidate solutions can be several MeV. We apply an initial quadrupole constraint [78] of ± 500 fm^2, usually large enough to find the minima shown in Fig. 7.4.

Unlike deformation properties, the β-decay Q values estimated from our ground state calculations are significantly less consistent among functionals. However, reasonable Q-value estimates are essential since the rare-earth isotopes of interest are exceedingly neutron-rich; we cannot count on experimental Q-value data being available. Our Q-value estimates come from the HFB+QRPA prescription of Ref. [150]: the ground state Q value is given in terms of nuclear masses via Eq. (2.5)

$$Q_\beta = M_i(Z, N) - M_f(Z + 1, N - 1) - m_e, \tag{2.5}$$

or in terms of nuclear binding energies that we calculate with HFBTHO ($B < 0$) as

$$Q_\beta = B_i - B_f + (m_n - m_p - m_e). \tag{7.10}$$

53

The binding energy of the β-decay daughter, required in Eq. (7.10), is approximated by

$$B_f \approx B_i + \lambda_\pi - \lambda_\nu + E_0^{(\mathrm{pn})}, \tag{7.11}$$

where the λ_μ are the HFB Fermi energies (representing the change in binding energy with the addition or removal of a nucleon [72]), and $E_0^{(\mathrm{pn})}$ is the lowest two-quasiparticle excitation energy of the ground state. The correct value for $E_0^{(\mathrm{pn})}$ would be found by performing many matrix QRPA calculations with different final-state angular momenta and selecting the lowest-energy excitation. Without the ability to spend so much computational effort on $E_0^{(\mathrm{pn})}$ (the FAM does not provide the energies of individual states), we approximate the lowest-energy excitation as the sum $E_0^{(\mathrm{pn})} \approx E_\pi^0 + E_\nu^0$; that is, we neglect interactions between the two states and take the quasiparticle energies directly from HFBTHO. Our approximation to Q, as in Ref. [150], is then

$$Q_\beta = \Delta M_{n-H} + \lambda_\nu - \lambda_\pi - E_0^{(\mathrm{pn})}, \tag{7.12}$$

with ΔM_{n-H} the mass difference between a free neutron and a Hydrogen atom.

We have calculated Q_β for a handful of the most neutron-rich rare-earth nuclei with measured Q values in the 2012 Atomic Mass Evaluation [157]. The results are presented in Figure 7.5 and lead immediately to an important observation that our Q-value estimates are almost exclusively too large. Further, the Q values in this set of nuclei range from approximately 1–8 MeV, so a mean difference of 500 keV is not negligible. We will see shortly that this turns out not to be a major problem in most of our calculations, but the results obtained with UNEDF1-HFB (and to a lesser extent SLy5) are significantly worse than those with the other functionals. The Q values computed with UNEDF1-HFB are systematically $\simeq 1\,\mathrm{MeV}$ larger than those computed with SkO$'$ or SV-min. We have also included Q values from Möller $et~al.$ [160] in Fig. 7.5 for comparison; these lie much closer to the experimental values.

Q values have a much simpler connection to our β-decay calculations than the deformation does: the total β-decay rate λ (2.11) is roughly proportional to Q^5 [161] and thus very sensitive to errors. We will see later that too-small Q values (or correspondingly to too-long half-lives) can be fixed by adjusting the proton-neutron isoscalar pairing, but we do not have tools to fix too-large Q values. Despite these concerns, we have kept both SLy5 and UNEDF1-HFB in the calculation since PNFAM calculations are relatively inexpensive. Results obtained with these EDFs should be treated with some caution, but they will provide lower bounds on our calculated β-decay half-lives: large Q values imply large decay rates (and correspondingly short half-lives).
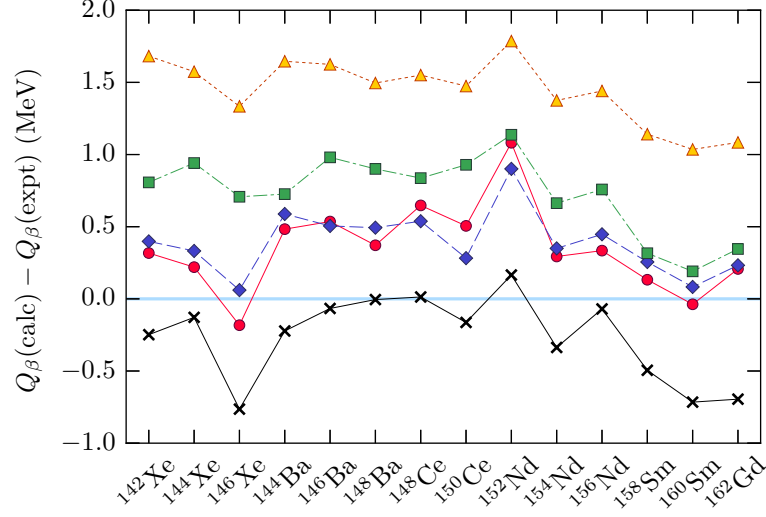
Figure 7.5: Difference between calculated and experimental Q_β values for a selection of rare-earth nuclei using the Skyrme functionals SkO$'$ (red circles), SV-min (blue diamonds), SLy5 (green squares), and UNEDF1-HFB (yellow triangles). The Q values of Möller *et al.* [160] (crosses) have been included for comparison. Experimental values are taken from the 2012 Atomic Mass Evaluation [157].

7.3.3: Treatment of odd nuclei

Our set of target nuclei includes a number of proton-odd isotopes, although they have not contributed to our fits. The half-lives of odd nuclei are computed using the EFA adaptation of pnFAM described in Chapter 6, and their ground states are determined using HFBTHO in the equal filling approximation. The EFA assumes a statistical density matrix built up from one-quasiparticle excitations of the HFB ground state, $\alpha^\dagger_{\Lambda_0} | \phi \rangle$. The quasiparticle level Λ_0 is not known *a priori*: since the HFB calculation is self-consistent the initial choice for Λ_0 affects all the resulting quasiparticle states (see, e.g., Ref. [115]). As a result we must run a series of trial calculations, blocking a variety of quasiparticle levels (a list of candidates is provided by HFBTHO) and selecting the configuration that produces the most-bound solution for the ground state. In practice odd-even ground state calculations are thus 5–15 times more expensive than even-even ones.

Section 7.4: β-decay properties

After adjusting the pairing functional (the parts of the functional that affect time-even calculations) and computing the ground states of the nuclei of interest, we now consider β-decay properties. The dominant charge-changing excitations we encounter are of the Gamow-Teller type, driven by the spin-isospin operator $\boldsymbol{\sigma} t_-$ (where $t_- | n \rangle = | p \rangle$ changes neutrons to protons), and several first-forbidden decay operators have a similar form. As a result, β-decay excitations are very sensitive to the parts of the functional that are odd under the action of the time reversal operator, which also reverses the angular momentum. As discussed previously, from the viewpoint of density functional theory the time-odd parts of these functionals are

unconstrained, so we have no knowledge *a priori* as to whether or not these Skyrme functionals will accurately describe β-decay transitions in this mass region.

Since β decay changes the nuclear charge, the proton-neutron isoscalar pairing (or $T = 0$ pairing), which is ineffectual in the time-even mean field, also plays a pivotal role in half-life calculations; it strongly affects the proton-neutron-mixed states that are obtained in the pnFAM. (See, e.g., Ref. [150] for just one example of how strongly the $T = 0$ pairing affects β-decay calculations.) To reproduce experimentally-measured β-decay half-lives—and to have confidence in our predictions—it is mandatory that we adjust the proton-neutron pairing and the time-odd, isovector part of the Skyrme functional ($H_1^{\mathrm{odd}}(\mathbf{r})$ in Eq. (4.5)) to nuclear data in this region.

7.4.1: The time-odd functional

On the face of it, adjusting the time-odd functional is a daunting task. The time-odd, isovector ($T = 1$) component of modern Skyrme functionals contains seven different combinations of time-odd densities, each multiplied by a different coupling constant [88]: C_1^s, $C_1^{\Delta s}$, C_1^T, C_1^j, $C_1^{\nabla j}$, $C_1^{\nabla s}$, and C_1^F. The relative paucity of charge-exchange nuclear data makes fitting all of these constants a very challenging problem. Mustonen and Engel have very recently made an effort to fit several of these coupling constants simultaneously [60], but such a task is beyond the scope of this work.

One way to simplify an adjustment of the functional is by requiring the Skyrme functional to be locally gauge invariant as some authors do [88, 162] (SV-min is one example of this [146]). (The enforcement of gauge invariance is approximately equivalent to the requirement of invariance under boosts.) Gauge invariance provides additional constraints on the functional, introducing connections between some time-odd coupling constants and also connecting time-odd couplings to "partner" time-even ones. We use this constraint as a way to fix as many of the time-odd couplings as possible in our selected functionals.

We determine the remaining couplings following the practical fit of Ref. [89]. Among other things, the authors of Ref. [89] studied the effect of the coupling constants C_1^s, $C_1^{\Delta s}$, and C_1^T on Gamow-Teller giant resonances of magic nuclei. (C_1^s can be density dependent and is sometimes written [144] $C_1^s[\rho] = C_{10}^s + C_{1D}^s \rho_0^\gamma$.) With the functional SkO$'$, they were able to match their calculations to data reasonably well for a few nuclei by leaving C_1^T at its normal (gauge-invariant) value and then setting $C_1^{\Delta s} = 0$. The density-independent coupling constant C_{10}^s was the only one they changed and set to a nonzero value.

In the same vein, for each of our functionals we set all the coupling constants not linked via gauge invariance to zero and perform a one-parameter search for the value of C_{10}^s. This coupling constant is adjusted so that the excitation energy of the Gamow-Teller giant resonance from the doubly-magic nucleus ^{208}Pb (i.e., the excitation energy in the daughter ^{208}Bi) matches the experimental value of 15.6 ± 0.2 MeV [163]. (The

excitation energy in the odd-odd daughter nucleus is estimated in our calculations as $E_x = E_{\text{FAM}} - E_0^{(\text{pn})}$ where $E_0^{(\text{pn})}$ approximates the lowest proton-neutron excitation energy and thus the energy of the ground state of ^{208}Bi.) ^{208}Pb is a good candidate for this fit since (1) pairing effects vanish in doubly-magic nuclei, preventing cross-talk between the time-odd functional and $T = 0$ pairing, and (2) it is heavier than other doubly magic nuclei for which we have experimental data and better-matches the rare-earth region.

The time-odd coupling constants we use after these fits are presented in Table 7.4. We have also introduced a fifth functional, called SkO$'$-Nd, for which the coupling constant was adjusted to the Gamow-Teller giant resonance from the deformed nucleus ^{150}Nd. This nucleus is well-deformed with $\beta = 0.29$, and the excitation energy of the giant resonance in ^{150}Pm is around 15.25 MeV [164].[3] We demonstrate the difference between our SkO$'$ and SkO$'$-Nd fits in Fig. 7.6. The new value for C_{10}^s, obtained with the $T = 0$ pairing turned off to avoid unwanted correlations between the pairing and the time-odd functional, is different by almost 20% from the SkO$'$ fit. We see from the figure that SkO$'$-Nd seems to slightly increase the amount of low-energy β-decay strength, which likely leads to shorter half-lives.
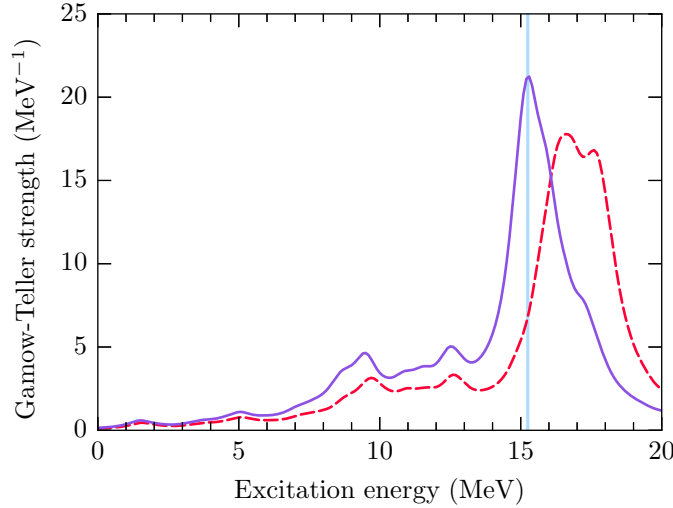
Figure 7.6: Demonstration of the effect of changing the coupling constant C_{10}^s on the Gamow-Teller giant resonance in ^{150}Pm. The strength function obtained with the functional SkO$'$, adjusted to the Gamow-Teller giant resonance in ^{208}Bi, is plotted with a red dashed line and misses the experimental value [164] (vertical line) by a few MeV. The SkO$'$ strength function adjusted to reproduce this resonance, called SkO$'$-Nd, is plotted as a solid line and shows slightly increased low-energy transition strength.

7.4.2: The isoscalar proton-neutron pairing

The final piece of the puzzle is the proton-neutron isoscalar pairing. Because it also introduces correlations between protons and neutrons, the $T = 0$ pairing can significantly affect β decay by shortening half-lives as

---

[3] We thank D. L. Fang for bringing this measurement to our attention.

Functional	C_{10}^s	C_1^T	C_1^j	$C_1^{\nabla j}$
SkO$'$	128.0	-9.1719	4.1562	41.4444
SV-min	126.0	0.0	3.2393	-22.9681
SLy5	150.0	-65.0575	-23.7164	-31.25
UNEDF1-HFB	109.0	0.0	24.1357	-51.9125
SkO$'$-Nd	102.0	-9.1719	4.1562	41.4444

Table 7.4: Non-zero time-odd coupling constants used in our calculations. All couplings are in units of MeV fm^5 except C_{10}^s, which has units MeV fm^3. The functional SkO$'$-Nd differs from SkO$'$ only in its value of the coupling C_{10}^s.

the pairing strength $|V_0|$ is increased. Ref. [150] demonstrated it was possible, with a different type of pairing interaction, to find a value V_0 of the isoscalar pairing strength that well-reproduced the half-lives of several spherical nuclei simultaneously. Our goal is to similarly use neutron-rich rare-earth isotopes with measured half-lives to fit the $T = 0$ pairing. The resulting fits are perhaps not as clean as those in Ref. [150], but they do a reasonably good job of reproducing the half-lives of a large number of rare-earth nuclei.

To adjust the $T = 0$ pairing we consider the β-decay half-lives of the isotopes listed in the left-hand column of Table 7.5. These nuclei make up the most neutron-rich isotopes with $Z = 54, 56, 58, 60, 62$, and 64 that have measured half-lives with reasonable uncertainties according to Ref. [165]. For each nucleus in Table 7.5, and with each of our selected Skyrme EDFs (including SkO$'$-Nd), we approximately determine the pairing strength V_0 that reproduces the experimental β-decay half-life. These individual pairing strengths for each nucleus are then averaged together, weighting short-lived nuclei more heavily (since we expect the highly neutron-rich isotopes of interest to be even shorter-lived) with the function

$$w_i = \frac{1}{\log_{10}\left(T_{1/2}^{\text{expt}}(i)/35 \text{ ms}\right)}. \tag{7.13}$$

The reference half-life of 35 milliseconds in Eq. (7.13) provides sensible fits for the proton-neutron pairing, but it is not unique—we have also tested a reference of 25 milliseconds, and the resulting pairing strengths only changed by about 2%. We list our final averaged isoscalar pairing strengths in Table 7.6 along with the relative strength of the $T = 0$ pairing compared to the $T = 1$ pairing (noted g_{pp}). We will refer to this ratio below.

As detailed in Table 7.5, none of our five EDFs can reproduce the half-lives of all the isotopes in our test set—some half-lives are too short even when the isoscalar proton-neutron pairing is disabled ($V_0 = 0$). When there is no value of V_0 that reproduces the half-life, we remove the corresponding nucleus from the fit. Some functionals perform better than others in this regard; the best functionals (SkO$'$ and SV-min) also reproduced Q values well in Fig. 7.5. While the EDFs SkO$'$ (which reproduced 15 of 18 half-lives in our set)

Fit nuclei						Evaluation nuclei			
Z	N	Isotope	$T_{1/2}$ (s)	Excluded?		Z	N	Isotope	$T_{1/2}$ (s)
54	88	^{142}Xe	1.23	b	d e	50	84	^{134}Sn	1.05
54	90	^{144}Xe	0.388	b	d e	50	86	^{136}Sn	0.25
54	92	^{146}Xe	0.146		d e	52	82	^{134}Te	2508
56	88	^{144}Ba	11.5	a b	d e	52	84	^{136}Te	17.63
56	90	^{146}Ba	2.22	b	d e	52	86	^{138}Te	1.4
56	92	^{148}Ba	0.612		e	54	84	^{138}Xe	844.8
58	90	^{148}Ce	56	b c d e		54	86	^{140}Xe	13.6
58	92	^{150}Ce	4		d e	56	86	^{142}Ba	636
58	94	^{152}Ce	1.4		d e	56	94	^{150}Ba	0.3
60	92	^{152}Nd	684	a b c d e		58	90	^{146}Ce	811.2
60	94	^{154}Nd	25.9	b c d e		62	90	^{156}Sm	33840
60	96	^{156}Nd	5.06	b	d e	66	102	^{168}Dy	522
62	96	^{158}Sm	318	a b c d e		68	106	^{174}Er	192
62	98	^{160}Sm	9.6		e	70	108	^{178}Yb	4440
62	100	^{162}Sm	2.4		e	70	110	^{180}Yb	144
64	98	^{162}Gd	504	b	e	72	112	^{184}Hf	14832
64	100	^{164}Gd	45		e	72	114	^{186}Hf	156
64	102	^{166}Gd	4.8		e	74	116	^{190}W	1800

Table 7.5: Isotopes used to fit the proton-neutron isoscalar pairing and, later, to evaluate our complete fitting procedure. The experimental half-lives were taken from Ref. [165]. The labels a–e in the "Excluded?" column note which isotopes were excluded from our pairing fits for the functionals (a) SkO$'$, (b) SkO$'$-Nd, (c) SV-min, (d) SLy5, and (e) UNEDF1-HFB. Isotopes were excluded when our calculated half-lives were shorter than experimental values and the proton-neutron isoscalar pairing was disabled.

Functional	V_0 (MeV fm^3)	g_{pp}
SkO$'$	-320.0	1.25
SkO$'$-Nd	-300.0	1.17
SV-min	-370.0	1.06
SLy5	-240.0	0.77
UNEDF1-HFB	-0.0	0.00

Table 7.6: Fitted proton-neutron isoscalar pairing strengths describing rare-earth nuclei. We have included the dimensionless parameter $g_{\mathrm{pp}} = V_0/V_1 = 2V_0/(V_{\mathrm{p}} + V_{\mathrm{n}})$, which measures the strength of the $T = 0$ pairing relative to its $T = 1$ counterpart. That is, a value $g_{\mathrm{pp}} = 1$ means the $T = 0$ pairing is the same strength as the $T = 1$ pairing.

and SV-min (14 of 18) performed well, SLy5 (only 6 of 18) and UNEDF1-HFB (none) struggled to reproduce measured half-lives. It is notable that ground-state calculations with these latter EDFs yielded too-large Q values in Fig. 7.5; these functionals now demonstrate too-short half-lives with the proton-neutron isoscalar pairing disabled.

The connection between the reproduction of Q values and the relative shortening of half-lives is certainly not contradicted by the ratios of the $T = 0$ to $T = 1$ pairing strengths (g_{pp}) listed in Table 7.6. The values of g_{pp} demonstrate the relative importance of the proton-neutron isoscalar pairing, and SLy5 and UNEDF1-HFB stand out by requiring much smaller proton-neutron pairing strengths than the other EDFs.

We have yet to discuss the fit obtained with our readjusted functional SkO$'$-Nd, which presents an interesting in-between case. On one hand, SkO$'$-Nd could only reproduce 9 of our 18 test nuclei with any value $|V_0| \neq 0$. On the other hand, its best value of V_0 (and thus g_{pp}) is very similar to that of the SkO$'$ functional fitted to the GT giant resonance from ^{208}Pb. Since the two parameterizations are identical in every other way, this must be the result of the changed time-odd coupling constant C_{10}^s. This conclusion agrees with the strength function plotted in Fig. 7.6: for excitations in ^{150}Pm, the SkO$'$-Nd parameterization increases the low-energy transition strength which strongly affects the β-decay half-life—an increase in low-energy strength leads to reduced half-lives. So the SkO$'$-Nd readjustment leads to slightly shorter half-lives for our fit nuclei in Table 7.5, making it less capable of fitting all of these nuclei simultaneously. We will see below that, because we exclude these "unfittable" nuclei in the fit, the Nd-adjusted version of SkO$'$ produces slightly shorter half-lives even after fitting the proton-neutron pairing.

Section 7.5: Evaluation of fits, results, and conclusions

Simply by counting how many half-lives our Skyrme EDFs can reproduce from the left column of Table 7.5, we might expect SkO$'$ and SV-min to produce the best results and UNEDF1-HFB to perform rather poorly, with SLy5 and SkO$'$-Nd somewhere between. To evaluate our parameterizations more rigorously, we calculate half-lives for the thirty-six nuclei in Table 7.5, including the isotopes used in the proton-neutron pairing fit

plus an additional eighteen heavy nuclei. These nuclei have been selected to cover a significant extent of the rare-earth region, both in Z and in N.

The results of our test calculations are plotted in Fig. 7.7. We see that most of our functionals demonstrate a systematic bias towards too-short half-lives as the experimental half-life gets longer (or, generally, as Q_β gets smaller). The two SkO′-based functionals are notable for demonstrating the least bias, and UNEDF1-HFB is seriously inaccurate for most long-lived isotopes.

The two SkO′ functionals and SV-min all reproduce half-lives of short-lived nuclei ($T_{1/2} < 100$ s) very well—despite difficulties fitting the proton-neutron pairing with SkO′-Nd, it appears to perform roughly as well as SkO′. On the other hand, SLy5 and UNEDF1-HFB mostly yield too-short half-lives even for the shorted-lived isotopes in our set, though SLy5 is less biased than UNEDF1-HFB overall.
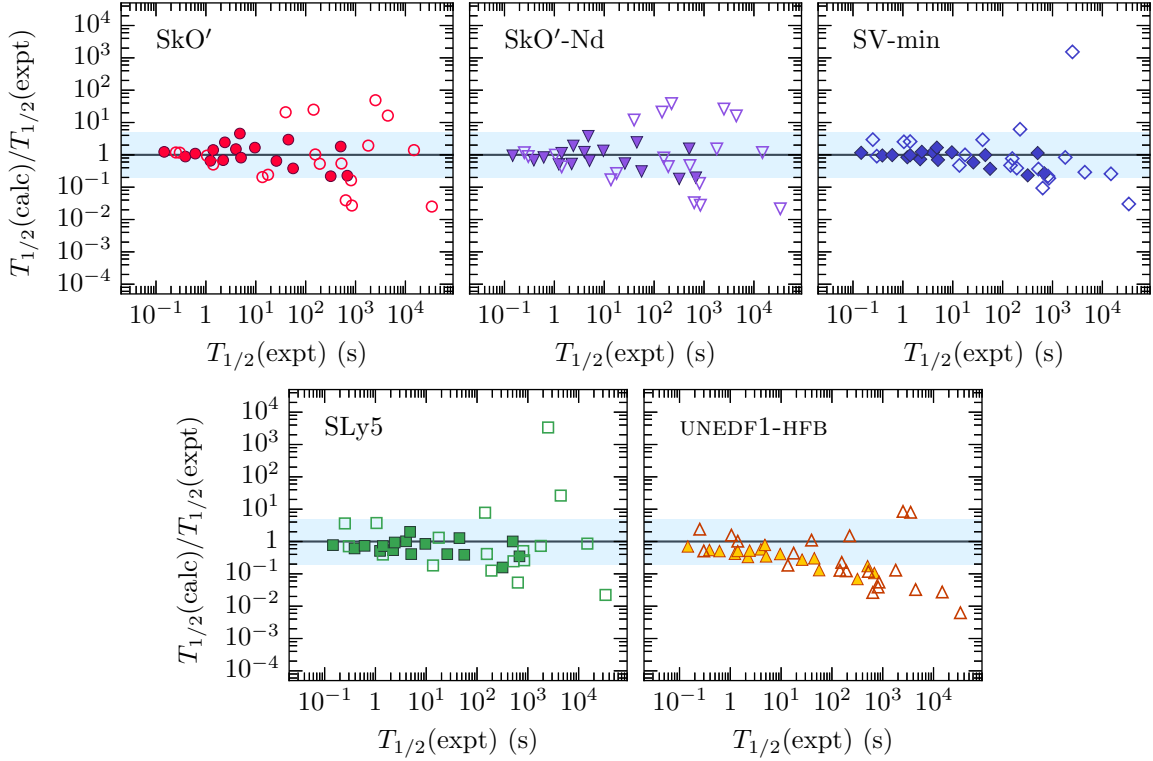
Figure 7.7: Evaluation of our adjustments through comparison between our calculated half-lives and experimental values for the nuclei in Table 7.5. By plotting the ratio $T_{1/2}(\text{calc})/T_{1/2}(\text{expt})$, our best calculations lie along the solid line with the ratio equal to 1, and nuclei with short experimental half-lives are generally better-reproduced. Filled symbols represent nuclei in the left column of Table 7.5, and open symbols represent the nuclei in the right column (i.e., not even considered in the proton-neutron pairing fit). The shaded area represents a deviation of $\pm 5\times$ the experimental value.

We can also assess our fits numerically using the quantity r defined as [125]

$$r = \log_{10}\left[\frac{T_{1/2}(\text{calc})}{T_{1/2}(\text{expt})}\right], \tag{7.14}$$

along with related statistical quantities from Refs. [55, 125]. Deviations from experimental values can be evaluated in terms of the mean (M_r), standard deviation (σ_r), and RMS error (Σ_r) of the set $\{r_i\}$ by expressing these quantities as powers of 10 (e.g., $M_r^{10} \equiv 10^{M_r}$) [55, 125]. We have computed these diagnostics and list them in Table 7.7 alongside values derived from the global calculations of Möller *et al.* [55]. The calculations of Ref. [55] are a useful benchmark since they also include first-forbidden β-decay transitions.

We find, as expected from Fig. 7.7, that SkO$'$, SkO$'$-Nd, and SV-min provide the best results, both for short-lived nuclei and for the entire set; these EDFs, along with SLy5, show a modest improvement in the mean deviation M_r^{10} compared with the results of Möller *et al.* This is not so surprising—our functionals are specifically tailored to this region of the nuclear chart while Möller *et al.*'s are global—but it serves as a useful check that our best parameterizations give sensible results. We also see that even SLy5 and UNEDF1-HFB are not so poor as we might have expected, at least for short-lived nuclei: UNEDF1-HFB certainly produces the worst results, but even this EDF underestimates the half-lives of short-lived nuclei only by approximately a factor of 2.

Functional	$T_{1/2} \leq 100$ s				All isotopes			
	N	M_r^{10}	σ_r^{10}	Σ_r^{10}	N	M_r^{10}	σ_r^{10}	Σ_r^{10}
SkO$'$	21	1.11	2.68	2.69	36	0.92	5.30	5.31
SkO$'$-Nd	21	0.90	2.51	2.52	37	0.84	5.54	5.59
SV-min	21	1.10	1.74	1.75	37	0.84	4.98	5.02
SLy5	20	0.79	2.07	2.15	35	0.80	6.76	6.85
UNEDF1-HFB	21	0.52	1.93	2.54	38	0.29	4.46	7.03
Möller, *et al.* [55]	21	1.63	2.28	2.61	38	1.30	2.96	3.05

Table 7.7: Statistical measures of goodness-of-fit in the rare-earth region for both our entire set (Table 7.5) and short-lived nuclei only. We have analyzed both the five EDFs used in this work and results from the global fit of Möller *et al* [55]. The metric $M_r^{10} = 10^{M_r}$ (described in the text and taken from Refs. [55, 125]) represents the mean deviation of a set of computed half-lives: $M_r^{10} = 1.0$ implies a perfect fit (on average), and $M_r^{10} = 2.0$ implies a mean deviation by a factor 2. The standard deviation (σ_r^{10}) and RMS error (Σ_r^{10}) are defined similarly. On occasion we could not compute a reasonable half-life value and removed these isotopes from consideration (this is why N changes for different EDFs).

With these diagnostics in mind, we present in Fig. 7.8 our set of calculated half-lives for the r-process nuclei listed in Table 7.1. The uniformity of our calculated β-decay half-lives is striking given the wide range of Q values produced by the different Skyrme EDFs in Fig. 7.5 and the challenges we encountered fitting the proton-neutron isoscalar pairing in lighter-mass nuclei. Although our EDF adjustments appear to smooth out the largest differences in Q, Fig. 7.9 demonstrates that (1) the evolution of our calculated Q values with increasing neutron number is at least somewhat correlated with the evolution of the half-lives and (2) our Q values are very similar to those calculated by Möller *et al.* in Ref. [160]. We also see in Fig. 7.8, as expected from our Q-value analysis and $T = 0$ pairing fits, that SLy5 and UNEDF1-HFB produce somewhat

shorter half-lives than the other functionals. However, even with its clear systematic errors for longer-lived isotopes (Fig. 7.7), UNEDF1-HFB produces results that are only shorter than those of SkO′ (which provides our longest-lived results) by approximately a factor of 2.
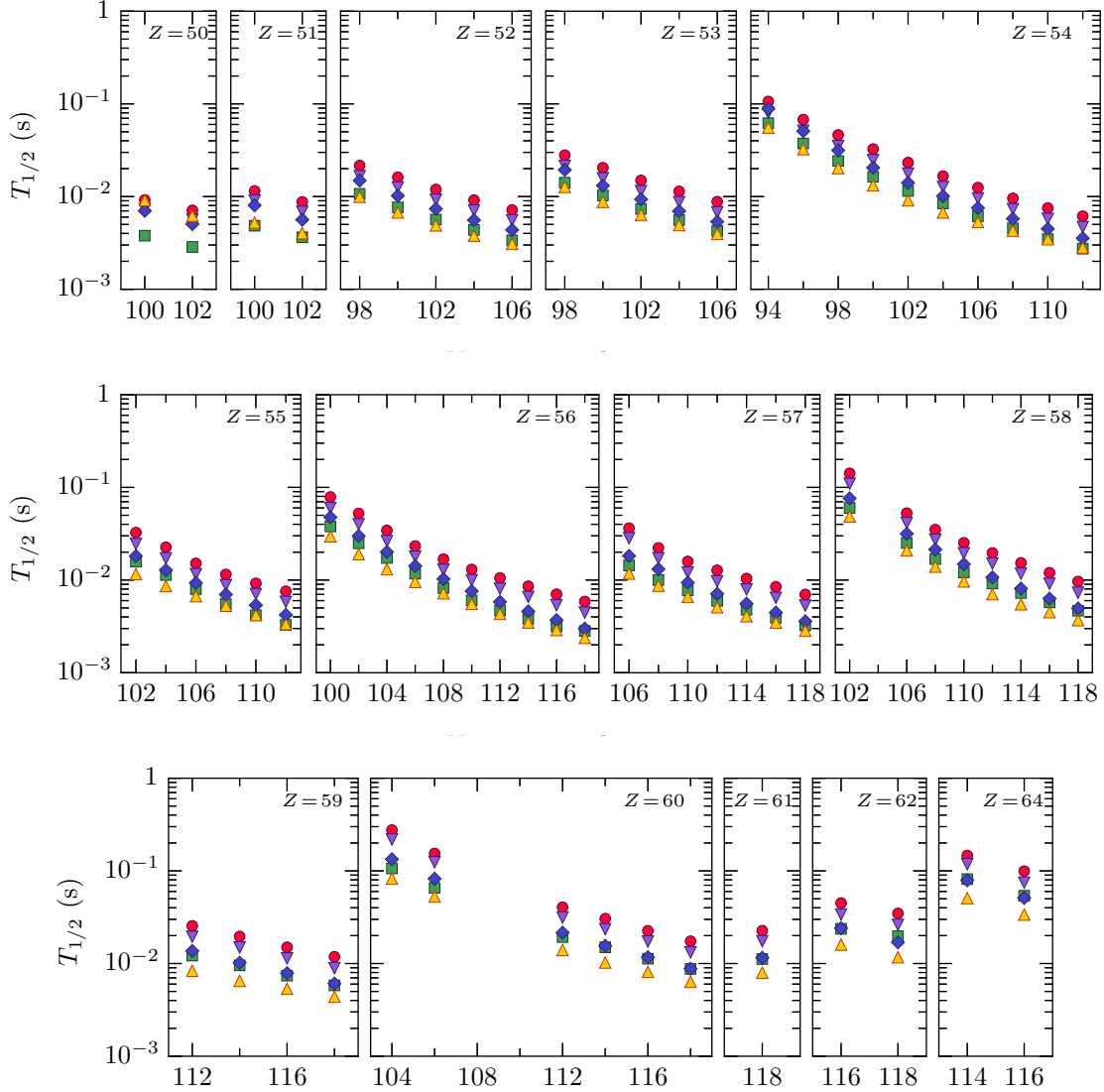
Figure 7.8: Calculated half-lives for the seventy rare-earth nuclei in Table 7.1. The various markers correspond to SkO′ (red circles), SkO′-Nd (purple triangles), SV-min (blue diamonds), SLy5 (green squares), and UNEDF1-HFB (orange triangles).

Comparing the half-lives produced with SkO′ and SkO′-Nd in Figs. 7.8 and 7.9, we also see that altering the parameter C_{10}^s does not significantly affect the pattern of the resulting half-lives (after re-adjusting the proton-neutron isoscalar pairing). The half-lives computed with SkO′-Nd are (uniformly) slightly shorter, probably because fewer nuclei contributed to the pairing fit and only those that had long-enough half-lives.
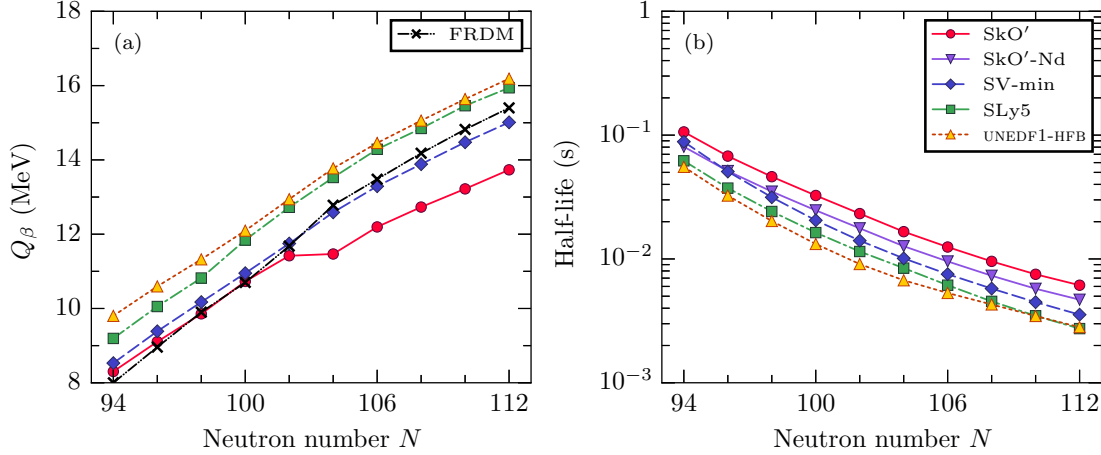
Figure 7.9: Evolution of (a) Q values and (b) half-lives for neutron-rich Xe isotopes. Panel (a) includes Q values calculated with the finite-range droplet model (FRDM) of Möller *et al.* [160] for comparison. In panel (b) we have also included half-lives calculated with SkO′-Nd, which share the same Q values as SkO′.

The overall effect is rather small.

We compare all of our computed half-lives with those of Möller *et al.* [55] in Fig. 7.10. Möller *et al.*'s half-lives generally lie on the shorter-lived side of our three most reliable calculations (SkO′, SV-min, and SkO′-Nd), and at times their half-lives change more dramatically with neutron number than do ours. The results from Ref. [55] most closely agree with our values computed using SV-min, which is understandable in light of the close agreement between FRDM (the mass model used by Möller *et al.*) and SV-min calculations of Q_β in Fig. 7.9. SV-min is also the functional which demonstrated the best overall fit according to Table 7.7.

We note that Möller *et al.*'s results differ most significantly from ours in Fig. 7.10 for nuclei with $Z = 50$ and $Z = 51$—we predict somewhat longer half-lives for these isotopes. Because we did not include closed-shell nuclei in our fits of the proton-neutron pairing, our results are probably less reliable for these few nuclei. When we consider the β-decay of $A \simeq 80$ nuclei in Chapter 8 we will find that closed-shell nuclei require somewhat stronger proton-neutron pairing strengths than usual.

At first glance, the lack of any serious disagreement between our calculations and those of Möller *et al.* [55] is surprising. Our calculations do, however, share common features: Although the calculations of Möller *et al.* are significantly different from ours in the details, their decay rates were still obtained with the QRPA using a one-parameter β-decay interaction. This is not so dissimilar from what we have done here—our simple adjustment of C_{10}^s can be directly connected to that of a single term in the nuclear two-body interaction:

$$V \sim 2C_{10}^s(\boldsymbol{\sigma} \cdot \boldsymbol{\sigma}')(\boldsymbol{\tau} \cdot \boldsymbol{\tau}')\delta(\mathbf{r}_1 - \mathbf{r}_1')\delta(\mathbf{r}_2 - \mathbf{r}_2')\delta(\mathbf{r}_1 - \mathbf{r}_2). \tag{7.15}$$

If C_{10}^s parameterizes the most important part of the Skyrme EDF for β-decay calculations, it is at least less
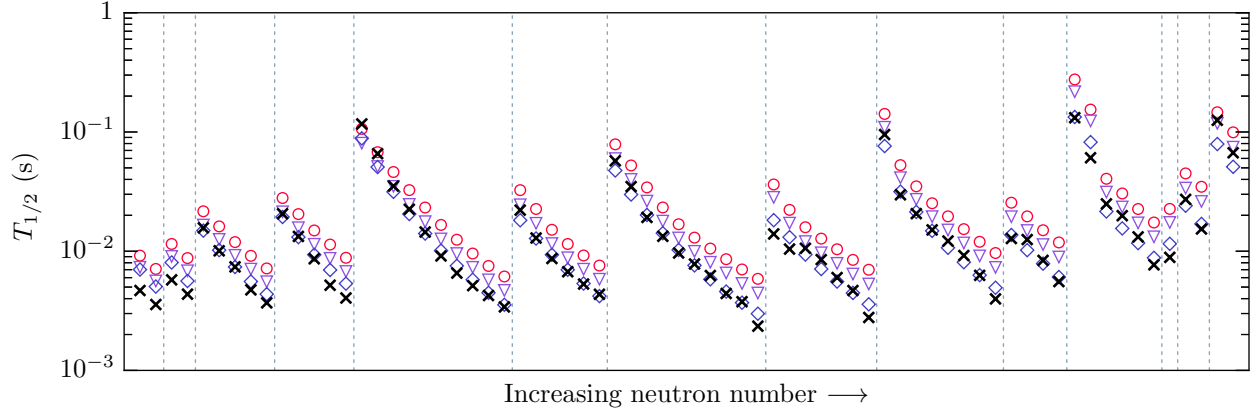
Figure 7.10: Comparison of our results applying the EDFs SkO′ (red circles), SkO′-Nd (purple triangles), and SV-min (blue diamonds) with those of Möller *et al.* [55] (crosses) for the same nuclei as Fig. 7.8. Vertical lines separate isotopic chains, which are ordered with increasing Z as in the previous figure.

surprising that the two calculations produce similar results. (Notably, however, Möller *et al.*'s calculation did not include proton-neutron isoscalar pairing, which plays a key role in this work.) It also seems that the two-body interaction of Möller *et al.* was adjusted to experimental giant resonances [55, 80, 166] in a similar way as we have done here.

A recent, more holistic attempt to constrain the time-odd parts of the Skyrme functional that affect β decay (but not ground state properties) has been carried out by Mustonen and Engel [60]. This work resulted in half-lives that were not much better than previous calculations over the last two decades. Ref. [60] found that C_{10}^s and V_0 constituted the dominant effect on half-lives and concluded that it seems "difficult" to reproduce β-decay half-lives much better using only the QRPA. Nonetheless, it is interesting that our targeted calculations are so similar to Möller *et al.*'s global ones. It has been found that the calculations of Möller *et al.* result in too-long half-lives for $N = 126$ waiting-point nuclei in particular (see, e.g., Refs. [52, 53] and refs. therein), and recent calculations (e.g., Refs. [58, 167]) have resulted in shorter half-lives. We do not see a comparable shift to lower half-lives in the mid-shell REE region.

Finally, it is also interesting to examine the relative importance of allowed and first-forbidden β-decay transitions in our calculations. We have plotted the first-forbidden contributions to the β-decay rate in Fig. 7.11. The results demonstrate that forbidden transitions are certainly not negligible in this region, and that the relative importance of these decays varies among the different EDFs. First-forbidden transitions (the contribution of nuclear operators with $J^\pi = 0^-$, 1^-, and 2^-) make up roughly 10–40% of the total β-decay rate in this mass region. The first-forbidden contributions can also be visualized as a function of Z and N as in Ref. [60]: results obtained with the functional SV-min are shown in Fig. 7.12. This figure reveals that first-forbidden contributions to the half-life increase both with N and Z—the effect depends approximately

on the mass of the nucleus.
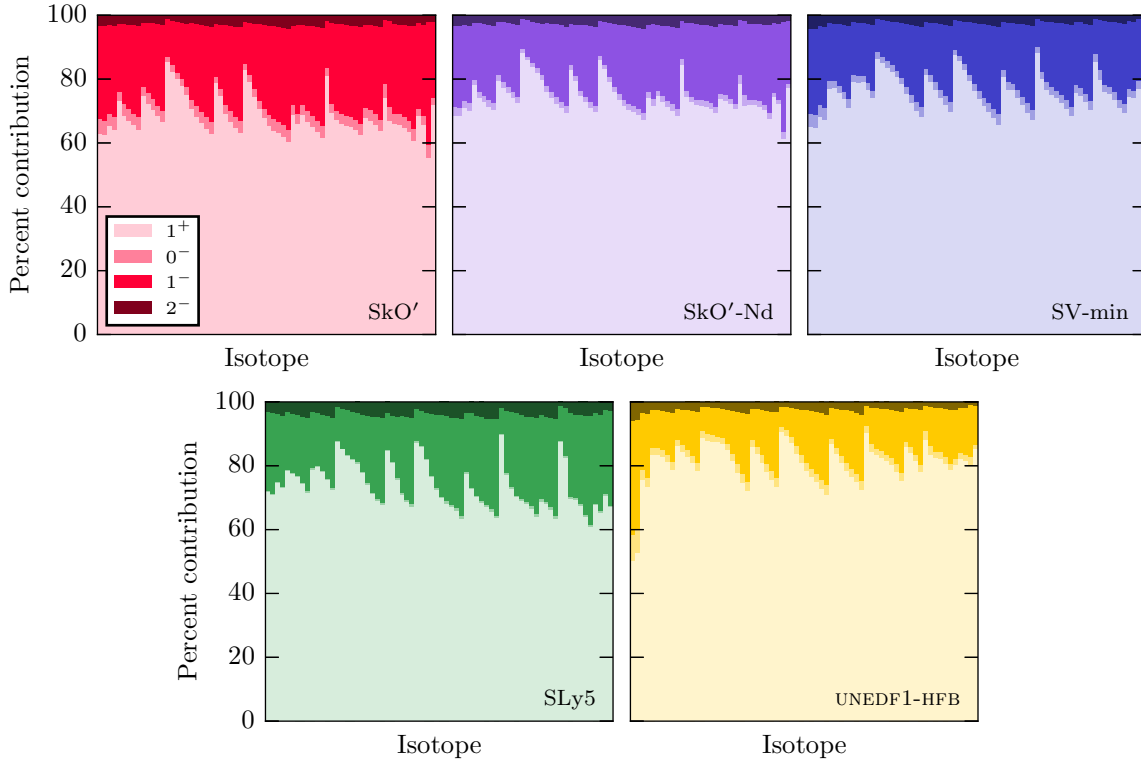
Figure 7.11: Multipole decomposition of the β-decay transition strength for all seventy r-process nuclei in Table 7.1, in ascending order of Z and N. Allowed (1^+) decays dominate as expected, but the first-forbidden transitions (0^-, 1^-, and 2^-) comprise a significant fraction of the β strength. (Fermi (0^+) β decay is neglected since these transitions occur at very high excitation energies.)

Section 7.6: Consequences for rare-earth r-process nucleosynthesis

Calculated r-process abundances obtained using our β-decay half-lives are shown in Fig. 7.13, compared with abundances derived from the half-lives of Möller $et\ al.$ [55]. Our calculated half-lives are broadly similar to those of Ref. [55], but are almost uniformly faster or slower depending on the Skyrme EDF (cf. Fig. 7.10). Most notably in a hot r process (top panel of Fig. 7.13), a uniform increase in half-lives seems to fill in the REE peak [62]. Correspondingly, the shortened half-lives we have calculated with SLy5 and UNEDF1-HFB slightly erode the peak.

The bottom panel of Fig. 7.13, which displays results from a neutron star merger r-process trajectory, exhibits a different behavior. With this trajectory, nuclear abundances are most strongly altered near $A \approx 150$ and $A \approx 180$; the main REE peak is largely unaffected. This demonstrates the impact of nuclear physics input on r-process studies—our new decay rates affect the various r-process trajectories in different ways.

We note that these abundances are not calculated completely self-consistently, though consistent r-process
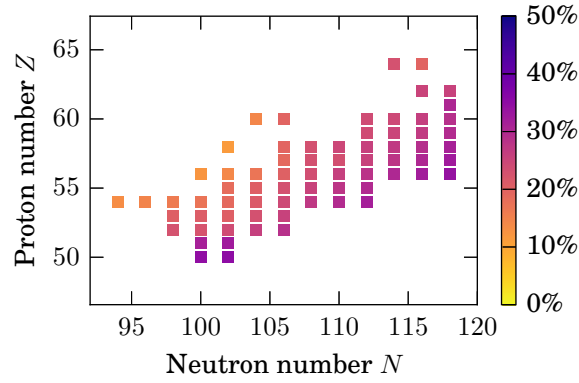
Figure 7.12: First-forbidden contributions to the β-decay rate for the functional SV-min. The results are plotted as a percentage, i.e., "50%" means that the first-forbidden transitions make up 50% of the β-decay rate.

calculations are strongly preferred [3, 4]. The calculations presented in Fig. 7.13 incorporate β-delayed neutron emission probabilities from a different set of calculations.

By including a variety of EDFs in our calculations, Figs. 7.8 and 7.13 provide a sense of the uncertainties in both our results and derived rare-earth r-process abundances. Our best functionals, SkO$'$, SkO$'$-Nd, and SV-min, produce abundance patterns that deviate from the baseline by a factor of $\sim$2, strengthening the rare-earth peak in top and middle panels, while SLy5 and UNEDF1-HFB seem to give a comparable deviation in the opposite direction. The overall scale of these abundance effects is roughly consistent with calculations performed in Ref. [25], which carefully considered the propagation of errors in nuclear masses (which affect, among other nuclear physics observables, β-decay half-lives) through r-process calculations.

We conclude that our calculations suggest a slight increase in rare-earth r-process abundances above those calculated with the β-decay half-lives of Möller *et al.*, particularly with hot and cold r-process trajectories. The variation in r-process abundances for different EDFs, especially when we include the SLy5 and UNEDF1-HFB functionals, makes drawing stronger conclusions more difficult and highlights the challenges inherent in the search for the r-process site.
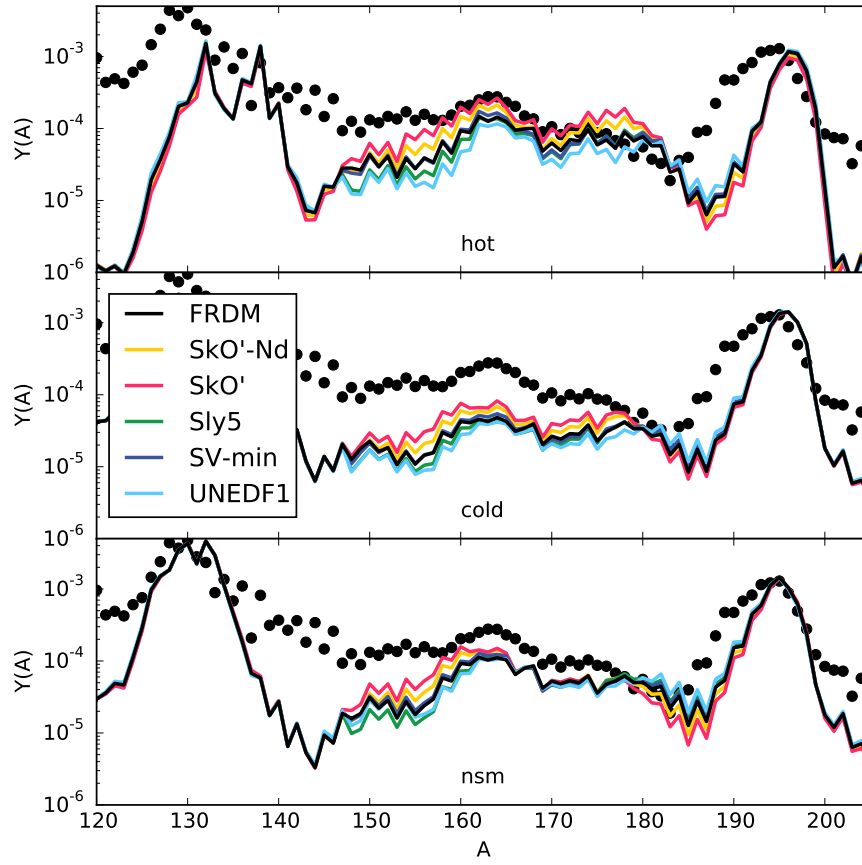
Figure 7.13: Calculated *r*-process abundances, using the same trajectories as Fig. 7.1, that incorporate the β-decay half-lives calculated in this work. The solid black line is the baseline abundance distribution obtained with the β-decay calculations of Möller *et al.* [55]. Figure courtesy of M. Mumpower [62].

CHAPTER 8: β-DECAY HALF-LIVES OF ISOTOPES WITH $A \simeq 80$

Our second application of the pnFAM to r-process nuclei focuses on isotopes with mass number $A \simeq 80$ in an effort to better constrain weak r-process contributions to abundances in this region. Along the same lines as the previous chapter we are guided by an r-process sensitivity study, provided by R. Surman, highlighting the β-decay half-lives that most strongly affect r-process abundances near $A = 80$. The results of the study are displayed in Fig. 8.1, computed in a scenario thought to generate a weak r process [62]. From this sensitivity study we have compiled a list of 45 nuclei spanning 10 isotopic chains that have the largest impact on r-process abundances in this region. This set of nuclei, all with $24 \leq Z \leq 34$ and $44 \leq N \leq 64$, are listed in Table 8.1 and plotted in Fig. 8.2 for reference. Although not listed in the ENSDF compilation we have used here [168], the half-lives of ^{76,77}Co and ^{80,81}Cu have been recently measured and reported in Ref. [169]. We have computed new half-lives for these nuclei as well.
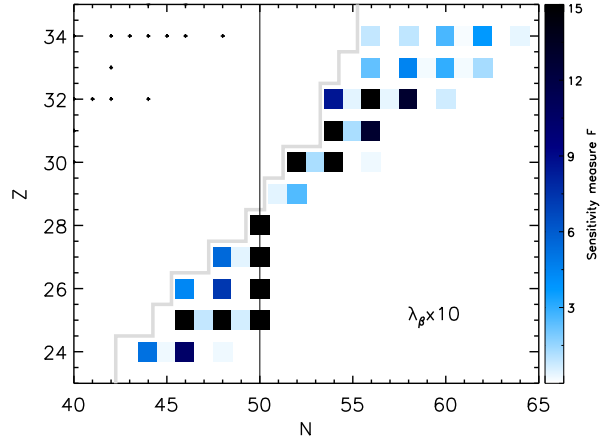
Figure 8.1: Sensitivity study in the $A \simeq 80$ region similar to that described in Ref. [141], courtesy of R. Surman [62]. Rates were varied by a factor of 10 to obtain this figure, and nuclei are shaded more darkly with increasing importance to the r process. Stable isotopes are marked by crosses, and the grey line denotes the boundary between measured and not-measured β-decay half-lives.

We have decided to apply SV-min, the best-performing functional from Chapter 7, for this set of calculations. SV-min demonstrated both the best average agreement with experimental half-lives and the smallest variance for nuclei with half-lives shorter than 100 seconds (see Table 7.7). As before, we will fine-tune the Skyrme EDF to best represent the ground-state and β-decay properties of nuclei in this mass region. The broad points of the adjustment (which parts of the EDF should be re-adjusted, and which can

Z	Isotopes
24	^{68}Cr, ^{69}Cr, ^{70}Cr, ^{71}Cr, ^{72}Cr
25	^{71}Mn, ^{72}Mn, ^{73}Mn, ^{74}Mn, ^{75}Mn
26	^{72}Fe, ^{73}Fe, ^{74}Fe, ^{75}Fe, ^{76}Fe
27	^{76}Co, ^{77}Co
29	^{80}Cu, ^{81}Cu
30	^{84}Zn, ^{85}Zn, ^{86}Zn
31	^{86}Ga, ^{87}Ga
32	^{86}Ge, ^{87}Ge, ^{88}Ge, ^{89}Ge, ^{90}Ge, ^{91}Ge, ^{92}Ge
33	^{89}As, ^{90}As, ^{91}As, ^{92}As, ^{93}As, ^{94}As, ^{95}As
34	^{92}Se, ^{93}Se, ^{94}Se, ^{95}Se, ^{96}Se, ^{97}Se, ^{98}Se

Table 8.1: The forty-five $A \simeq 80$ r-process nuclei studied in this work. Their locations on the nuclear chart are also plotted in Fig. 8.2.
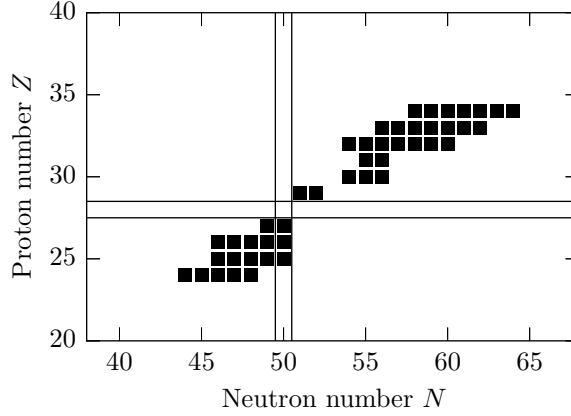
Figure 8.2: Locations of the r-process nuclei in Table 8.1 on the nuclear chart (cf. Fig. 1.1). The $Z = 28$ and $N = 50$ shell closures are also highlighted.

be used as given) remain unchanged, and we refer to the previous chapter for background and motivation.

After adjusting the SV-min pairing strengths (V_p, V_n, and V_0) and coupling constant C_{10}^s to experimental data in this region, we will also use $A \simeq 80$ nuclei to test our pnFAM-EFA method for calculating β-decay half-lives of odd nuclei. This provides a fairly large set of half-lives with which to analyze both (1) our SV-min re-parameterization and (2) the quality of our odd β-decay scheme in general. Results for odd nuclei in the previous chapter did not immediately suggest significant problems for odd nuclei, but a proper test of the pnFAM-EFA is essential to verify that technique is accurate enough to apply.

Section 8.1: Ground state properties

As in the previous chapter, the first part of this new calculation involves (1) determining the optimal ground state pairing strengths V_p and V_n for nuclei in this mass range and (2) computing the ground states of the r-process nuclei in Table 8.1. Our ground-state calculations are carried out in the same way that was

described previously, both for even-even and singly-odd nuclei.

In addition, there are several odd-odd nuclei in our set; their ground states are computed in a similar way as the singly-odd nuclei, described in Chapter 7. Starting from a reference even-even nucleus, HFBTHO provides a list of candidate states (numbered N_p and N_n for protons and neutrons, respectively) in which to place the odd nucleon. We determine the ground state of the odd-odd nucleus by computing all $N_p \times N_n$ blocking configurations and then selecting the most-bound solution. Odd-odd ground state calculations are then, by default, more difficult than those of both even-even and odd-even nuclei. These calculations tend to be more fragile in practice as well. Once we have successfully determined the ground state, however, our choice for the blocked quasiparticle levels $(\Lambda_\pi, \Lambda_\nu)$ is fixed; subsequent PNFAM calculations based upon this ground state are no more complicated than usual.

8.1.1: Adjusting the pairing strengths

We adjust the proton and neutron pairing strengths by finding values for V_p and V_n that best reproduce the pairing properties of $A \simeq 80$ nuclei. As before, this requires comparing the average pairing gap $\bar{\Delta}_{\text{HFB}}$ taken from HFBTHO with the indicators $\tilde{\Delta}^{(3)}$ calculated using experimental data from the 2012 Atomic Mass Evaluation [157]. We have adopted the set of nuclei in Table 8.2 for this procedure and calculated the values for the experimental mass indicators $\tilde{\Delta}^{(3)}$ that appear in the table.

Z	N	$\tilde{\Delta}_{\text{p}}^{(3)}$ (MeV)	$\tilde{\Delta}_{\text{n}}^{(3)}$ (MeV)
24	32	1.26354	1.01634
26	38	1.17387	1.29269
30	44	1.01199	1.41433
32	46	1.13235	1.24835
32	48	0.99635	1.17779
34	52	1.17100	0.78968
36	54	1.15773	0.83990
36	56	1.18243	0.90644
38	58	1.11437	0.93063
38	60	0.99089	0.85591
42	62	0.99786	0.95077
28	38	0.00000	1.20975
32	50	0.95788	0.00000
28	50	0.00000	0.00000

Table 8.2: $A \simeq 80$ nuclei whose pairing properties entered into the proton and neutron pairing strength adjustments. The experimental indicators $\tilde{\Delta}^{(3)}$ (7.7) are computed using data from the 2012 Atomic Mass Evaluation [157] as described in Chapter 7. Nuclei with $Z = 28$ or $N = 50$ have $\tilde{\Delta}^{(3)}$ set to zero by hand.

Following discussions with M. T. Mustonen, and with some assistance, we improved our ground state fits by replacing the "by-hand" fitting technique from the previous chapter with a program driven by the non-linear least-squares algorithm POUNDERS [170]. The POUNDERS algorithm has been previously applied, for

example, to fit ground-state Skyrme functionals using HFBTHO [144]. More recently, M. T. Mustonen has used the method to optimize the time-odd parts of the Skyrme EDF [60]. We apply it here to search for the parameters $(V_\mathrm{p}, V_\mathrm{n})$ which best represent the nuclei in Table 8.2.

The POUNDERS algorithm searches for the best values V_p and V_n iteratively: at each step we provide the algorithm with a weighted set of residuals

$$X_i = w_i \left[\bar{\Delta}_i(V_\mathrm{p}, V_\mathrm{n}) - \tilde{\Delta}_i^{(3)} \right], \tag{8.1}$$

where $\bar{\Delta}_i$ is obtained from an HFBTHO calculation and the index i runs over both proton and neutron pairing gaps. These residuals are all given the weight $w_i = 1$ except for the doubly-magic nucleus ^{78}Ni, to which we assign $w_i = 10$ in an effort to minimize the spurious introduction of pairing correlations into magic (closed-shell) nuclei. The algorithm then determines new trial values V_p' and V_n' that we apply with HFBTHO, and the iteration proceeds. Our values for the proton and neutron pairing strengths obtained via POUNDERS are, in rounded form, $V_\mathrm{p} = -361.0$ MeV fm^3 and $V_\mathrm{n} = -320.9$ MeV fm^3 (cf. $V_\mathrm{p} = -374.0$ and $V_\mathrm{n} = -322.0$ in the rare-earth region). We have checked the quality of the fit by examining the RMS deviation in $\bar{\Delta}_{\mathrm{HFB}}$ for the nuclei used in the fit, with values of V_p and V_n near the optimal solution (the pairing strengths used are within 0.01% of their optimal values). The RMS error for these nuclei is only 176 keV (10–20% of the values listed in Table 8.2).

8.1.2: Shape deformations and ground state pairing properties

Having fixed the pairing strengths, it is instructive to examine the ground state deformations of nuclei in this mass region. We have plotted the quadrupole deformation β for even-even nuclei in Fig. 8.3 and find a very different situation than that of the rare-earth isotopes (Fig. 7.4). These lighter isotopes have neither the large absolute values of β found in rare-earth nuclei ($\beta \sim 0.3$–0.4) nor the smooth transition from spherical or oblate shapes to strong prolate ones. Rather, these $A \simeq 80$ nuclei exhibit a fairly abrupt transition from prolate to oblate shapes around $N = 56$. There is also a large section of spherical or nearly-spherical isotopes, even beyond the $Z = 28$ and $N = 50$ shell closures.

It is likely that the primary cause of this difference in nuclear shapes between our rare-earth and $A \simeq 80$ calculations is the location of these lighter isotopes on the nuclear landscape. It is well known that nuclei with closed proton or neutron shells tend to have spherical shapes [72], and the influence of these shell closures is clearly seen in the values of β near the lines $Z = 28$ and $N = 50$. It is clearly not the case that all of these $A \simeq 80$ nuclei are spherical—they still have very large neutron excesses $N \approx 2Z$ and deformations $|\beta|$ approaching 0.2—but rather that the deformation varies much more quickly between isotopes and isotones.
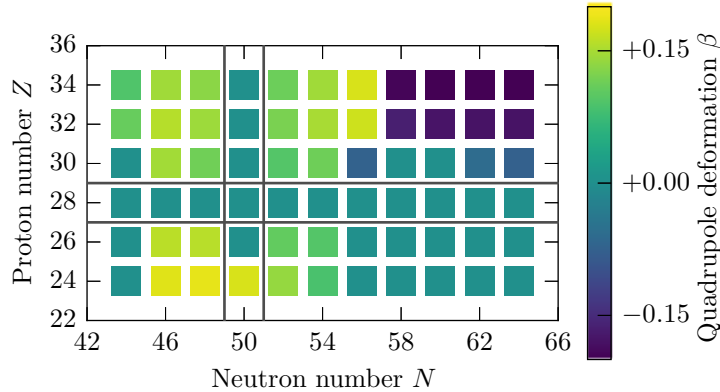
Figure 8.3: Quadrupole deformations β of nuclei in the $A \simeq 80$ region.

We find as well that the "depth" of the potential-energy minimum at the ground state deformation is shallower than in rare-earth nuclei, with only 10s or 100s of keV between prolate and oblate solutions (cf. MeV differences in many rare-earth isotopes).

We also expect pairing correlations to disappear in closed shells [72], which reduces the ability of the proton-neutron isoscalar pairing to shorten the half-lives of such nuclei. (As mentioned above, we have tried to *ensure* these pairing correlations vanish while fitting V_p and V_n.) As a result, the proton-neutron pairing will act differently in $Z = 28$ and $N = 50$ nuclei than in the remainder of the set in Table 8.1. To the extent that the smoothly-varying nature of the rare-earth isotopes improved the quality of our fine-tuning in the previous chapter, it may be correspondingly more difficult to represent these $A \simeq 80$ successfully.

Section 8.2: Excited states

Having fixed the proton and neutron pairing strengths, we must still adjust both the proton-neutron pairing strength V_0 and the coupling constant C_{10}^s. Previously, we used the Gamow-Teller giant resonance from ^{208}Pb to fix C_{10}^s since ^{208}Pb is both doubly magic (pairing correlations are therefore suppressed) and situated relatively near to the rare-earth region. Applying these criteria to the $A \simeq 80$ mass region, we have selected the doubly-magic nucleus ^{48}Ca for the corresponding $A \simeq 80$ fit. The GT giant resonance from ^{48}Ca to ^{48}Sc has an experimental resonance energy of 10.6 MeV in ^{48}Sc [171].

Our previous fit for the time-odd coupling constant C_{10}^s required estimating the ground state energy of the odd-odd daughter nucleus through the parameter $E_0^{(\text{pn})}$. This approximation may be avoided by examining the excitation energy with respect to the even-even target nucleus, E_t, [151, 172] instead of the excitation energy with respect to the odd-odd daughter. E_t is calculated by adding the mass difference between final

and initial nuclei plus the neutron-proton mass difference to the excitation energy:

$$E_t = E_x + (M_f - M_i) + (m_n - m_p) \approx E_x + (B_f - B_i). \tag{8.2}$$

The corresponding calculated quantity, taken from the PNFAM and HFBTHO, can be computed using the approximation (7.11) for the binding energy difference:

$$E_t^{\text{calc}} = E_{\text{FAM}} + \lambda_\pi - \lambda_\nu. \tag{8.3}$$

The Fermi energies λ_μ are taken directly from our HFB calculation of ^{48}Ca, so E_t^{calc} does not depend on any estimated parameters. We find that $E_t \approx 11.1$ MeV in ^{48}Ca using binding energies calculated from [157], and the value $C_{10}^s = 148.0$ MeV fm^3 fits the giant resonance in this scheme—an increase of approximately 16% from the SV-min value for ^{208}Pb. The remaining time-odd coupling constants are kept at their values from the previous chapter (Table 7.4).

8.2.1: Fitting the proton-neutron isoscalar pairing

We adjust the proton-neutron isoscalar pairing using the nuclei listed in Table 8.3, specifically including both magic and open-shell nuclei. These nuclei, whose half-lives are tabulated in the ENSDF [168], are among the most neutron-rich isotopes for $Z \in [22, 36]$ with reasonably precise half-life measurements.

Open-shell					Semi-magic			
Z	N	Isotope	$T_{1/2}$ (s)		Z	N	Isotope	$T_{1/2}$ (s)
22	38	^{60}Ti	0.022		28	46	^{74}Ni	0.680
24	40	^{64}Cr	0.043		28	48	^{76}Ni	0.238
26	44	^{70}Fe	0.094		30	50	^{80}Zn	0.540
30	52	^{82}Zn	0.228		32	50	^{82}Ge	4.560
32	52	^{84}Ge	0.954				—	
34	54	^{88}Se	1.530				—	
36	60	^{96}Kr	0.080				—	

Table 8.3: $A \simeq 80$ nuclei whose half-lives were taken as inputs to adjust the proton-neutron isoscalar pairing. Isotopes in the left column were used to determine the pairing strength for non-magic nuclei, and isotopes in the right column were used to determine the pairing strengths for nuclei with at least one closed shell. The experimental half-lives were taken from the ENSDF [168].

We use an interpolation scheme to determine the optimal proton-neutron pairing strength for these nuclei, computing a set of half-lives for each isotope over several values of V_0 and using splines to approximate a continuous dependence of $T_{1/2}$ on V_0. Because the half-life depends on V_0 smoothly on a logarithmic scale (see Fig. 8.4), we fit the interpolating splines to the logarithmic ratio r defined in Eq. (7.14). We then minimize

the function

$$F(V_0) = \sum_{i=1}^{\text{no. nuclei}} \left[\log T_{1/2}^{\text{calc}}(V_0; i) - \log T_{1/2}^{\text{expt}}(i) \right]^2 \tag{8.4}$$

to find the best-fit value of V_0.

Figure 8.4 demonstrates that our set of open-shell nuclei (solid lines) are best fit with a weaker proton-neutron pairing interaction than the magic isotopes (dashed lines). This makes sense—the shell closures at $Z = 28$ and $N = 50$ generally suppress pairing correlations among proton and neutrons, respectively, and so the proton-neutron correlations should be suppressed as well to some extent. Minimizing the function $F(V_0)$ separately for magic and open-shell nuclei, we obtain the pairing strengths listed in Table 8.4. The application of these values to our calculations is straightforward: for nuclei with $Z = 28$ or $N = 50$ we use the value $V_0^{\text{cs}} = -549$ MeV fm^3, and for all other nuclei we use $V_0^{\text{os}} = -353$ MeV fm^3.
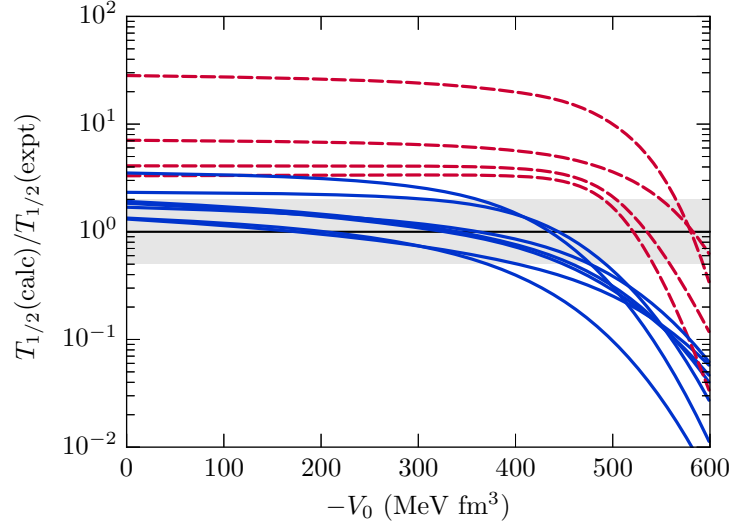
Figure 8.4: Dependence of our calculated half-lives on the isoscalar pairing strength V_0 for open-shell (solid lines) and semi-magic (dashed lines) nuclei listed in Table 8.3. These half-lives are plotted as the ratio $T_{1/2}(\text{calc})/T_{1/2}(\text{expt})$, so a value 1.0 indicates perfect agreement between calculation and experiment. The curves were obtained by interpolating between logarithms of our calculated values $T_{1/2}(\text{calc})$ using splines before plotting the values $10^{\log_{10} T_{1/2}(\text{interp})}$. The grey shaded area highlights the region in which our calculations agree with experimental results within a factor of 2.

Classification	V_0 (MeV fm^3)
Open-shell	-353.0
Closed-shell	-549.0

Table 8.4: Fitted proton-neutron isoscalar pairing strengths V_0 for open-shell and closed-shell nuclei as demonstrated in Fig. 8.4.

Section 8.3:   Fit evaluation, results, and conclusions

Having optimized the pairing and excited-state properties of SV-min, we test our new parameterization using a large set of $A \simeq 80$ nuclei with experimentally-measured half-lives. For this test we have selected all even-even and singly-odd nuclei from the ENSDF data set [168] with $22 \leq Z \leq 36$ and $T_{1/2} \leq 1$ day. The resulting list includes 41 even-even nuclei and 92 singly-odd nuclei.

Our results for these nuclei are presented in Fig. 8.5 alongside the calculations of Möller *et al.* [55]. Direct inspection combined with a statistical analysis presented in Table 8.5 suggests our SV-min adjustment performs well: we are able to reproduce the half-lives of even-even nuclei very well, significantly better than the global fit of Ref. [55]. Importantly, we also find that we reproduce the β-decay half-lives of short-lived odd nuclei nearly as well as we do their even-even neighbors. Our results degrade somewhat for longer half-lives, but for nuclei with $T_{1/2} \leq 100$ s we find a mean deviation of about 1.86 for odd nuclei (that is, our average half-life in a logarithmic sense is 1.86 times the experimental value) compared to 1.17 for even-even nuclei and 0.81 from Ref. [55]. Recalling that we did not include any odd isotopes in the adjustment of SV-min, we take these results as a validation of our pnFAM-EFA calculations.

	$T_{1/2} \leq 100$ s				All isotopes		
	N	M_r^{10}	σ_r^{10}	Σ_r^{10}	N	M_r^{10}	σ_r^{10}	Σ_r^{10}
This work, even-even	35	1.172	3.081	3.115	39	1.315	5.021	5.138
Möller *et al.*, even-even	36	2.949	2.807	4.459	41	3.549	4.788	7.495
This work, odd	71	1.858	4.396	4.978	89	2.705	9.403	11.611
Möller *et al.*, odd	73	0.806	3.063	3.127	92	0.950	6.450	6.455

Table 8.5: Comparison of our SV-min re-adjustment with results from Ref. [55] using the (logarithmic) statistical measures of Refs. [55, 125] (see Eq. (7.14) and Table 7.7). Occasionally, our calculations have produced negative or unusable half-lives; these isotopes (2 even-even, 3 odd) have been removed from the statistics.

We are also aware of recent calculations of Ge, Se, and Kr half-lives for even-even and odd nuclei [125] using a separable QRPA interaction. In these calculations (which did not include forbidden β decay) the interactions between the odd valence nucleon and the even core are treated perturbatively. We have reproduced three figures from this reference in Fig. 8.6 and included our own results using the SV-min parameterization described above. We find that our computed half-lives are mostly equivalent to or better than the results of Ref. [125] for isotopes with experimentally-measured half-lives, both for even and odd nuclei.

8.3.1:   Half-lives of $A \simeq 80$ nuclei

Having tested our parameterization of SV-min against experimental values and recent β-decay calculations, we present half-lives in Fig. 8.7 for the $A \simeq 80$ r-process nuclei in Table 8.1. As in the rare-earth region, our results are broadly similar to those of Möller *et al.* [55], particularly in the low-Z and high-Z isotopic chains.
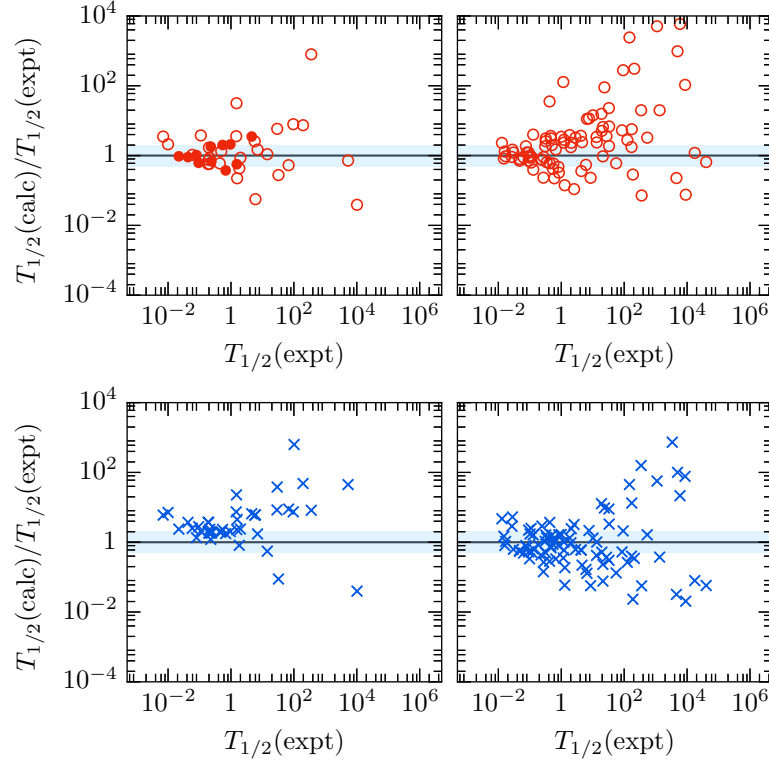
Figure 8.5: Evaluation of our SV-min adjustment (top) compared to the result of Möller *et al.* [55] (bottom) for nuclei with $22 \leq Z \leq 36$ and $T_{1/2} \leq 1$ day, as a function of the experimental value for the half-life. This evaluation is plotted as the ratio between calculated and experimental half-lives, so agreement with experiment produces a y-value of 1. The even-even nuclei used in the SV-min adjustment are represented by filled circles in the top graph. Experimental values were taken from the ENSDF [168], and the shaded region covers a factor of 2 relative to these experimental values.
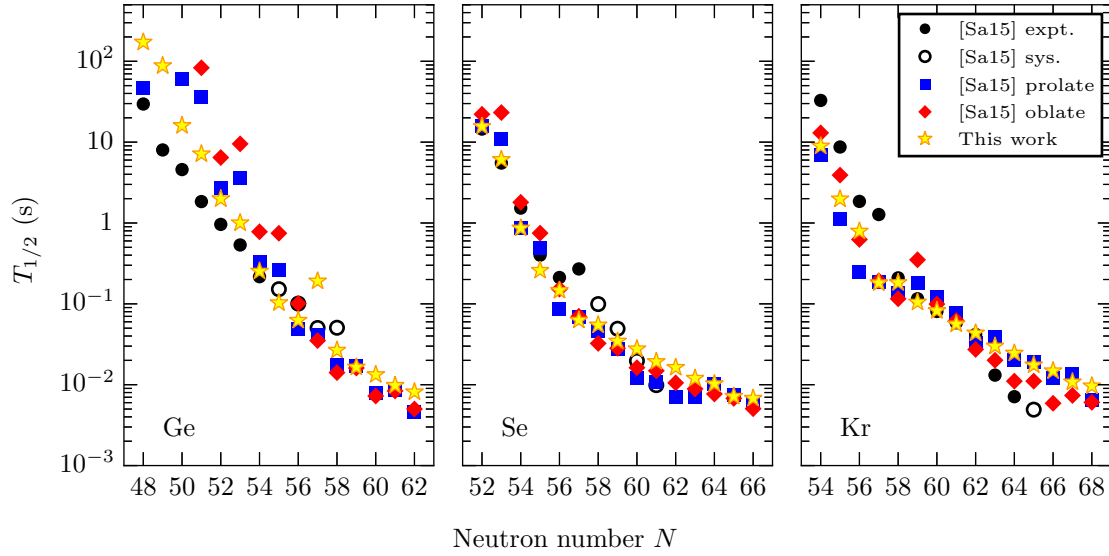
Figure 8.6: β-decay half-life chains for Ge, Se, and Kr, with our calculations (stars) plotted alongside those reproduced from Ref. [125] ("[Sa15] prolate/oblate"). All experimental values, including those from systematics ("sys."), are reproduced from Ref. [125]. Adapted with permission from Ref. [125]. Copyrighted by the American Physical Society.
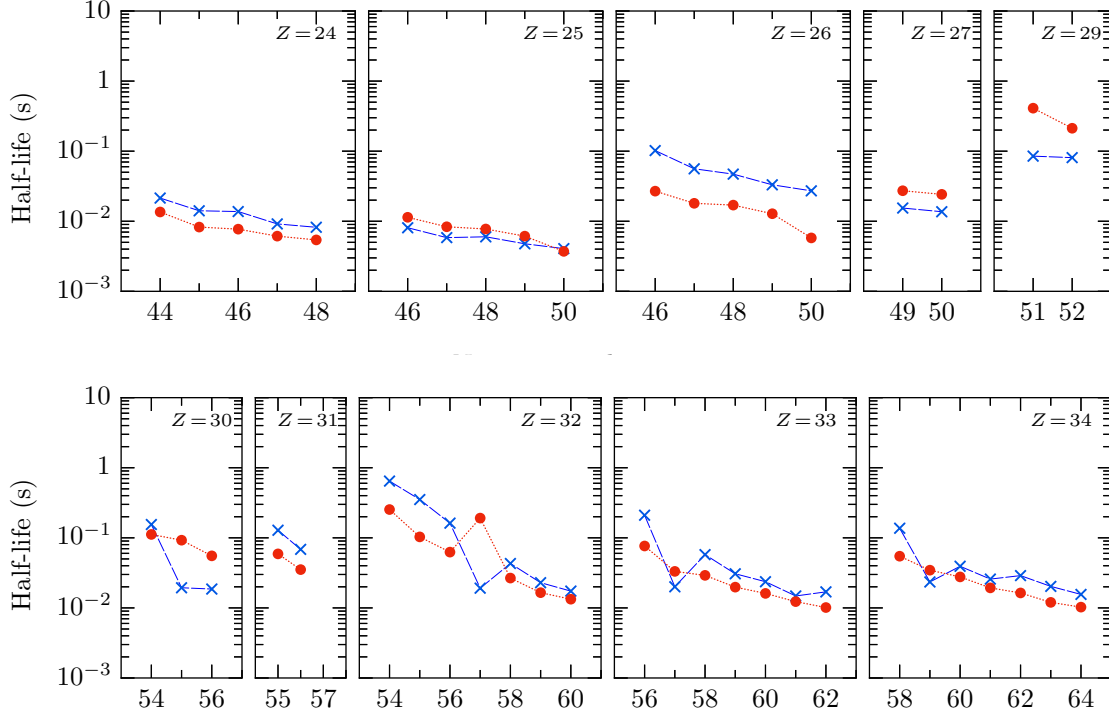
Figure 8.7: Calculated half-lives in this work for the forty-five $A \simeq 80$ r-process nuclei in Table 8.1 (red circles) compared with corresponding values from Möller $et\ al.$ [55] (blue crosses).

A notable feature of our results is the slight increase in half-lives for $N \sim 55\text{–}57$ nuclei due to a changeover from prolate to oblate ground state deformations (or vice versa). The most striking example is ^{89}Ge, situated between isotopes with fairly strong prolate (^{88}Ge, $\beta = 0.17$) and oblate (^{90}Ge, $\beta = -0.17$) deformations. Our predicted half-life is much longer than that of Ref. [55] because we predict ^{89}Ge to be spherical in its ground state ($\beta = 0$) with relatively weak pairing among neutrons ($\Delta_n = 0.27$ MeV, cf. 1.11 MeV for protons). In a case such as this the proton-neutron pairing is likely less able to affect β-decay transitions, resulting in a somewhat longer half-life.

We have also plotted the effect of the first-forbidden β-decay transitions in Figs. 8.8 and 8.9. On the whole, forbidden transitions are much less important in these nuclei than in the rare-earth region (cf. Figs. 7.11 and 7.12), as noted in, e.g., Refs. [70, 125] and references therein. However, the Cu and Zn isotopes, plus ^{89}Ge, are notable exceptions and demonstrate very large first-forbidden contributions. This places our calculations somewhere between that of Borzov [70], who did not find significant first-forbidden contributions in $N = 50$ isotones, and Marketin *et al.* [58], for whom first-forbidden transitions contribute significantly in $N = 50$ nuclei. It is interesting that, in our calculation, Zn and Ge nuclei with large first-forbidden contributions lie in shape-transition regions (cf. Fig. 8.3)—particularly because the calculations of Ref. [58] were restricted to spherical shapes.
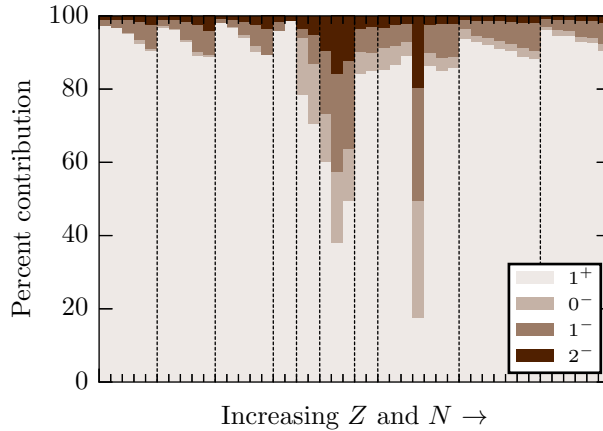
Figure 8.8: Contributions of the allowed (1^+) and first-forbidden (0^-, 1^-, 2^-) transitions to the total β-decay rate for the r-process nuclei in Fig. 8.7. Isotopic chains are separated by dashed vertical lines and are ordered as in Fig. 8.7.

We note occasional difficulties in calculating half-lives of odd nuclei, when the blocking procedure we apply to obtain the ground state of proton-odd nuclei can lead to artificially small (or even negative) β-decay rates as well as transition energies $E_\nu - E_\pi < 0$. (We have observed similar, though much less dramatic, issues with negative decay rates in relatively stable even-even nuclei with small Q values.) In our calculation, the half-lives of the nuclei ^{77}Co and ^{81}Cu (odd number of protons) as well as ^{82}Cu, ^{86}Ga, and ^{94}As (doubly
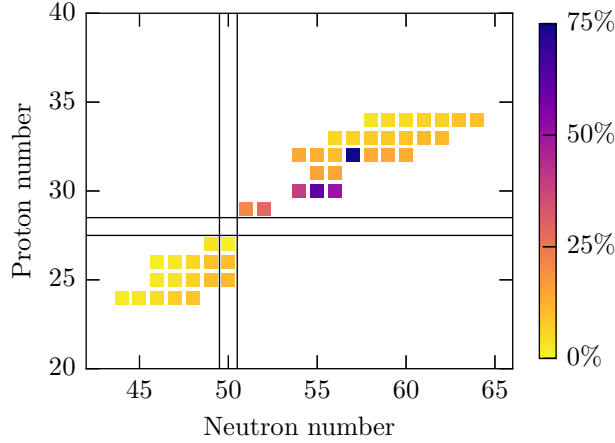
Figure 8.9: Total first-forbidden contribution to the β-decay rate as a function of proton and neutron number. The copper ($Z = 29$) and zinc ($Z = 30$) isotopes, as well as ^{89}Ge, stand out as the only isotopes with significant forbidden contributions.

odd) have been identified as potentially artificially elongated.

8.3.2: Consequences for the weak r process

The weak r-process abundances obtained with our new β-decay half-lives are shown in Fig. 8.10 and compared with abundances calculated using half-lives from Möller *et al.* [55] as well as the REACLIB database[1] [56]. Many $A \simeq 80$ β-decay half-lives in REACLIB come from an older theoretical calculation by Klapdor *et al.* [57],[2] which predicts very different half-lives from ours and those of Ref. [55], especially for lighter elements. Fig. 8.10 was formed by replacing the REACLIB half-lives (blue curve) with either our values (red) or those of Möller *et al.* (purple) for only the isotopes we have studied here. The abundance patterns derived from more recent β-decay calculations (the red and purple curves in Fig. 8.11) are fairly similar to one another, but the abundances computed with the REACLIB half-lives (blue curve) are dramatically different—particularly for nuclei with $A > 90$.

As in the $A \simeq 160$ region, we find only small differences between abundances computed from half-lives in this work and those of Möller *et al.* [55] despite many of our computed half-lives being shorter than those of Ref. [55] (cf. Fig. 8.7). The relatively small changes in the abundance pattern can be explained via a cancellation effect, demonstrated in Fig. 8.11, in which faster β decay in the peak region (with $Z \lesssim 28$ and

---

[1] `https://groups.nscl.msu.edu/jina/reaclib/db/`

[2] We thank R. Surman for pointing this out to us.
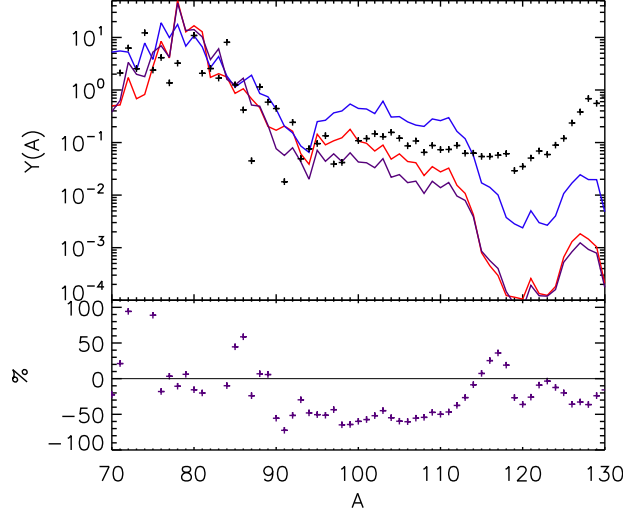
Figure 8.10: Weak *r*-process abundances computed with three sets of $A \simeq 80$ β-decay half-lives: those from this work (red), Möller *et al.* [55] (purple), and REACLIB [56] (blue). Figure courtesy of R. Surman [62].

$N \lesssim 50$) affect abundances differently than faster rates above the $Z = 28$ and $N = 50$ closed shells [62]. Faster rates for Fe isotopes (green lines and markers in Fig. 8.11) and Cr isotopes (light green) near the $A = 80$ *r*-process peak increase abundances at the doubly-magic waiting point ^{78}Ni. In this case less material can move to higher-*A* nuclei. On the other hand, faster rates for nuclei just a few neutrons from the $N = 50$ peak (e.g., Ge isotopes, the yellow line in Fig. 8.11) move material to higher-mass nuclei.

The net result of our new calculations is perhaps a slight narrowing of the $A = 80$ *r*-process peak and an increase in the abundance of $A > 90$ nuclei compared to results computed with half-lives from Möller *et al.* [55]. As was also the case for rare-earth nuclei, our $A \simeq 80$ calculations produce β-decay half-lives very similar to the global calculations of Ref. [55]. It is notable that both our new half-lives and those of Möller *et al.* predict significantly smaller $A > 90$ *r*-process abundances than the half-lives in REACLIB. This large difference demonstrates the necessity of improved β-decay half-life calculations, as well as continued experimental measurements, for accurate *r*-process calculations.
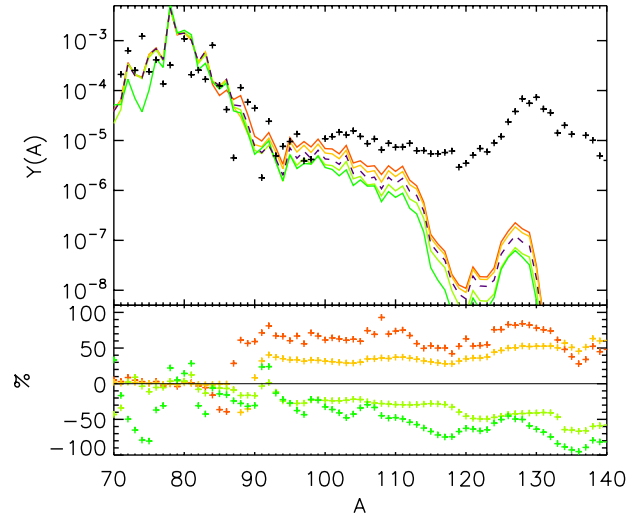
Figure 8.11: Impact of changes to the β-decay half-lives of individual elements on weak r-process abundances, courtesy of R. Surman [62]. The various lines demonstrate the effects of our newly-calculate half-lives on individual elements: Cr (light green), Fe (green), Ge (yellow), and As (orange). The Cr and Fe half-lives calculated in this work reduce the amount of $A > 100$ material while our new Ge and As half-lives increase the amount of $A > 90$ material.

CHAPTER 9: CONCLUSIONS AND IMPLICATIONS FOR FUTURE r-PROCESS AND β-DECAY STUDIES

To conclude, we briefly summarize the main results of this work and look ahead to future investigations. In Chapter 5 we have presented the proton-neutron finite amplitude method (pnFAM) [61], a new technique for calculating the β-decay half-lives of deformed nuclei that includes both allowed and first-forbidden transitions. The pnFAM is fast enough to enable the large calculations presented here and more—the method can scale up to global calculations, like the one of Ref. [60]. In Chapter 6 we have extended the pnFAM, originally restricted to even-even nuclei [61], to calculate half-lives of odd nuclei. This has been accomplished by applying the equal-filling approximation (EFA) to approximate properties of odd nuclei in a manner preserving key symmetries of the calculation. We have subsequently demonstrated in Chapter 8 that this EFA description of β decay yields reasonable half-lives when compared with experimental measurements and with the prescription of Möller *et al.* [55]. Following the introduction of the pnFAM, in Chapters 7 and 8 we have calculated β-decay half-lives of heavy, deformed nuclei found to strongly impact calculated r-process abundances in the $A \simeq 80$ and $A \simeq 160$ mass regions. Our goals in this investigation are two-fold: First, we have examined how our half-lives differ from previous work, specifically the calculations of Möller *et al.* [55], which is a decade old. Second, we have studied the effect of these new half-lives on calculated r-process abundances. Our results are summarized below—we have found that our calculations yield very similar half-lives to those of Möller *et al.* [55] and thus produce small changes in r-process abundances as a result.

Section 9.1: New calculations of β-decay half-lives of deformed nuclei

Both calculations in Chapters 7 and 8 yield very similar β-decay half-lives to those of Möller *et al.* [55]. We have suggested in Chapter 7 that similarities between the two calculations can be at least partially understood by considering the methods involved: both calculations employ the QRPA with fairly simple two-body β-decay interactions. This suggestion is based on the results of Ref. [60], which found that although the Skyrme EDF has many adjustable parameters, the two parameters we adjust in this work (the proton-neutron isoscalar pairing and the time-odd spin-isospin potential C_{10}^s) are the only meaningful ones in β-decay calculations. It also appears that Möller *et al.*'s two-body interaction was adjusted to experimental giant resonances [55, 80, 166] in a similar way as we have done following the practical recipe in Ref. [89].

Despite these similarities of technique, we note the calculations of Möller *et al.* [55] are based on a

very different mass model from ours, the finite-range droplet model. Our calculations also leverage the proton-neutron isoscalar pairing to bring calculated half-lives into agreement with experiment—introducing a parameter not required in Möller *et al.*'s calculations—and this pairing has a strong effect as shown in Chapter 8. Nonetheless, a comparison in Xe isotopes (Fig. 7.9) has shown that our Q-value predictions are very similar to those of Möller *et al.*, both in absolute value and in the overall trend. The two mass models approximately agree for very neutron-rich nuclei nuclei (this agreement appears worse for lighter isotopes, cf. Fig. 7.5). Our half-life calculations are also very similar to those of Möller *et al.* The adjustment of our Skyrme EDFs to experimental data appears to wash away most differences between mass models and pairing prescriptions.

Besides comparing our calculations to those of Möller *et al.* [55], we have examined the spread in calculated half-lives that can be expected by applying different Skyrme EDFs. We repeated our calculations in the $A \simeq 160$ mass region for a number of EDFs and found a fairly consistent range of half-lives. We have compared the results obtained with the EDFs SkO$'$ and SkO$'$-Nd, which are based on the same set of ground state calculations but have different values of the key parameters C_{10}^s and V_0. Changes to these parameters—constrained to reproduce experimental results—do not significantly affect half-lives.

However, a comparison between calculations that apply different functionals in ground-state calculations (e.g., SkO$'$ and SV-min or certainly SkO$'$ and UNEDF1-HFB) suggests that Q-values play an important role. In a test with Xe isotopes, the spread in predictions among functionals appears to be correlated with the evolution of Q_β (Fig. 7.9). In total, the interplay between ground-state properties and adjustments to the two-body β-decay interaction (C_{10}^s and V_0), results in a factor of 2–5 variation in half-lives among all functionals. If we restrict our analysis to functionals that well-reproduce experimental half-lives (i.e., exclude SLy5 and UNEDF1-HFB), this variation stays relatively constant near a factor of 2.

Section 9.2:   Consequences for the *r* process

Because our computed half-lives are very similar to those of Möller *et al.* [55], we have found correspondingly small effects on *r*-process abundances compared to baseline calculations applying rates from Ref. [55]. In the rare-earth region, our half-lives are almost uniformly faster or slower than those of Möller *et al.*, which in turn builds up or depletes the rare-earth abundance peak, depending on the astrophysical trajectory employed [62]. Although our results depend on the EDF employed, our three most reliable functionals (SV-min, SkO$'$, and SkO$'$-Nd) produce half-lives that are equivalent to or slightly longer than those of Möller *et al.*, thus slightly increasing abundances in, e.g., a hot *r* process (Fig. 7.13). However, the difference between our calculated half-lives and those of Möller *et al.* are small enough that these increases are quite small—about a factor of 2—with respect to baseline.

In the $A \simeq 80$ region we again find only small deviations between our calculations and those of Möller *et al.* [55]. The differences appear slightly less uniform than in the REE region, but our computed half-lives are mostly faster than those of Ref. [55]. New *r*-process calculations incorporating our half-lives are once again very similar to baseline computations applying Möller *et al.*'s rates (Fig. 8.10). It appears that in this region our new half-lives lead to a cancellation effect (Fig. 8.11): Faster half-lives above the waiting point ^{78}Ni tend to fill in gaps in the abundance distribution caused by faster half-lives below the waiting point [62].

We have also noted that our $A \simeq 80$ half-lives differ markedly from those appearing in the REACLIB database, which come from decades-old calculations [57]. These differences result in more significant changes to *r*-process abundances and demonstrate the impact of improved β-decay calculations as input for *r*-process studies.

Section 9.3: Future directions

The development of the pnFAM for even-even and odd nuclei should allow the application of Skyrme density functional theory across the nuclear chart. Indeed, Mustonen and Engel [60] have already made a full table of β^- half-lives available for even-even nuclei applying the pnFAM. Within the equal-filling approximation, we have found that odd calculations are only slightly more complicated than their even-even counterparts, and it does not seem too difficult to extend a full-table calculation to include most odd nuclei. Such a calculation could also be extended to approximately include β-delayed neutron emission, e.g., as found in Ref. [55], and now a full-table Skyrme calculation that consistently describes masses, Q values, β-decay half-lives, and β-delayed neutron capture rates seems possible.

It may also be useful to examine the Q-value properties of Skyrme EDFs in more detail and attempt to discriminate among EDFs based on Q_β calculations. We have seen in Chapter 7 that the wide variation in Q_β among EDFs can have real consequences for predictive power (e.g., SkO$'$ vs. UNEDF1-HFB). The functionals we have applied were all parameterized using nuclear data (and possibly the properties of nuclear matter), but produce a wide range of Q values. Even after incorporating the proton-neutron isoscalar pairing, our calculations have resulted in a spread of approximately a factor of 4 in calculated half-lives among functionals. It is unclear how much of an effect Q values actually have on these half-lives, but if the spread in half-lives in Figs. 7.8 and 7.9 is mostly attributable to β-decay Q values, this effect is not negligible.

This is an exciting time for large-scale nuclear structure calculations and for *r*-process physics. It now seems possible to extend microscopic Skyrme β-decay calculations across the nuclear chart, including both nuclear deformation and pairing correlations self-consistently. Such an effort could provide a deeper understanding of β-decay physics across the nuclear chart and also provide new, complete nuclear physics calculations for *r*-process studies—incorporating masses, Q values, deformation, β-decay half-lives, etc. self-consistently. In

this way we can continue to take small steps towards the goal of finally identifying the astrophysical r-process site.

APPENDIX A: DETAILED EXPRESSIONS FOR ALLOWED AND FIRST-FORBIDDEN β-DECAY RATES

In Chapter 2 we provided an overview of nuclear β decay, including the various classifications and an expression for the total β-decay rate of a nucleus, Eq. (2.11). In this appendix we provide more details, most of which are reproduced from Ref. [65]. We include expressions for the shape factors C_{J^π} in terms of reduced nuclear matrix elements, summarizing primarily Ref. [65] but also Refs. [63, 111]. We have also consulted Refs. [173, 174]. Our shape factors, in a form compatible with the pnFAM (Chapter 5), have also been published in Ref. [61].

Section A.1:   Overview of the β-decay rate

A proper derivation of the nuclear β-decay rate requires a relativistic treatment as presented in, e.g., Refs. [65] and [63]. The total rate is calculated using perturbation theory in the weak interaction, and the total decay probability per unit time is [65]

$$\frac{\mathrm{d}N}{\mathrm{d}t} \propto \sum_f \sum_s \int \left|T_{fi}\right|^2 \delta^3(\mathbf{p}_f + \mathbf{p}_e + \mathbf{p}_\nu)\,\delta(W_f + W_e + W_\nu - M_i)\,\mathrm{d}\mathbf{p}_f\,\mathrm{d}\mathbf{p}_e\,\mathrm{d}\mathbf{p}_\nu, \tag{A.1}$$

where the sum is taken over all final states and angular momenta, and T_{fi} is a transition matrix element. Following the convention of Ref. [65], energies and momenta are presented in natural units (scaled by the electron mass) and are labeled p and W, respectively. The transition matrix element contains the nuclear and lepton physics, notably including the influence of the nuclear charge distribution on the outgoing β-decay electron. Full expressions for $|T_{fi}|^2$ are terrifically complicated and must be treated approximately to relate T_{fi} to nuclear matrix elements (e.g., nucleons are treated as independent, point-like particles [65]). The results are presented in exhaustive detail in Refs. [65] and [63].

To relate the β-decay transition matrix element to nuclear physics calculations, the T_{fi} is expanded in multipoles corresponding to allowed ($J^\pi = 0^+$ and 1^+), first-forbidden (0^-, 1^-, 2^-), and higher forbidden decays. The transition matrix element for a given multipole can then be written [65]

$$\left|T_{fi}\right|^2 \to C_{J^\pi}(W_e)L_0 F_0(Z_i + 1, W_e), \tag{A.2}$$

where $Z_i + 1$ is the charge number of the daughter nucleus, F_0 is the standard Fermi function [65] which accounts for the distortion of the electron wave function by the nuclear charge distribution,

$$F_{k-1}(Z, W) = [k(2k-1)!!]^2 4^k (2pR)^{2(\gamma_k - k)} e^{\pi \alpha Z W/p} \left[\frac{|\Gamma(\gamma_k + i\alpha Z W/p)|}{\Gamma(1 + \gamma_k)} \right]^2, \tag{A.3}$$

$\alpha \approx 1/137.036$ is the fine structure constant [175], and L_0 and γ_k are Coulomb functions

$$\gamma_k = \sqrt{k^2 - (\alpha Z)^2}, \tag{A.4a}$$

$$L_0 \approx (1 + \gamma_1)/2. \tag{A.4b}$$

$C_{J^\pi}(W_e)$ is called the shape factor of the decay, and it is built up from energy-dependent combinations of nuclear matrix elements detailed below.

Section A.2: Allowed decay

The conventional allowed-decay shape factors, ignoring higher-order corrections (see Ref. [65] for corrections), are extremely simple. Each shape factor consists solely of the square of a single nuclear matrix element, squared:

$$C_{0^+} = M_{\mathrm{F}}^2, \tag{A.5a}$$

$$C_{1^+} = g_A^2 M_{\mathrm{GT}}^2, \tag{A.5b}$$

where $g_A = -1.2723 \pm 0.0023$ [66] is the weak axial-vector coupling constant for a free neutron. It is generally observed that g_A has a somewhat smaller absolute value in nuclei [4], and we use $g_A = -1$ in our calculations to approximate this effect. The two spin-reduced nuclear matrix elements appearing in (A.5) are (assuming the initial nucleus has angular momentum $J = J_i$):

$$M_{\mathrm{F}} = (2J_i + 1)^{-1/2} \langle \psi_f \, || \, t_- \, || \, \psi_i \rangle, \tag{A.6a}$$

$$M_{\mathrm{GT}} = (2J_i + 1)^{-1/2} \langle \psi_f \, || \, \boldsymbol{\sigma} \, t_- \, || \, \psi_i \rangle, \tag{A.6b}$$

where t_- is the isospin-lowering operator $(t_- | n \rangle = | p \rangle)$ and $\boldsymbol{\sigma}$ is a vector operator composed of Pauli spin matrices. We briefly discuss reduced matrix elements in Chapter 3.

Section A.3: First-forbidden decay

The shape factors which enter calculations of the first-forbidden decay rate are significantly more complicated than those in allowed decay since (1) the forbidden shape factors are energy-dependent, and (2) we now have many more nuclear matrix elements to calculate. In fact there are six operators which contribute: four from the multipole expansion of the lepton current and another two from the relativistic form of the

transition matrix element [111]. These operators enter into the following reduced nuclear matrix elements:

$$M_{[\mathbf{r}\boldsymbol{\sigma}]_0} = \frac{\sqrt{4\pi}}{\sqrt{2J_i+1}} \langle \psi_f \, || \, r \, [Y_1(\hat{\mathbf{r}})\boldsymbol{\sigma}]_0 \, t_- \, || \, \psi_i \rangle, \tag{A.7a}$$

$$M_{[\mathbf{r}\boldsymbol{\sigma}]_1} = -\frac{\sqrt{4\pi}}{\sqrt{2J_i+1}} \langle \psi_f \, || \, r \, [Y_1(\hat{\mathbf{r}})\boldsymbol{\sigma}]_1 \, t_- \, || \, \psi_i \rangle, \tag{A.7b}$$

$$M_{[\mathbf{r}\boldsymbol{\sigma}]_2} = \frac{\sqrt{4\pi}}{\sqrt{2J_i+1}} \langle \psi_f \, || \, r \, [Y_1(\hat{\mathbf{r}})\boldsymbol{\sigma}]_2 \, t_- \, || \, \psi_i \rangle, \tag{A.7c}$$

$$M_{\mathbf{r}} = \frac{\sqrt{4\pi}}{\sqrt{2J_i+1}} \langle \psi_f \, || \, rY_1(\hat{\mathbf{r}}) \, t_- \, || \, \psi_i \rangle, \tag{A.7d}$$

$$M_{\mathbf{p}\boldsymbol{\sigma}} = \frac{1}{M_N\sqrt{2J_i+1}} \langle \psi_f \, || \, \boldsymbol{\sigma} \cdot \boldsymbol{\nabla} \, t_- \, || \, \psi_i \rangle, \tag{A.7e}$$

$$M_{\mathbf{p}} = \frac{1}{M_N\sqrt{2J_i+1}} \langle \psi_f \, || \, \boldsymbol{\nabla} \, t_- \, || \, \psi_i \rangle. \tag{A.7f}$$

The specific matrix elements, and the combinations in which they appear, are determined by the expansion of the transition matrix element T_{fi}. This expansion generally includes very many terms (see Ref. [65] for full expressions) and is truncated at an acceptable order. We use the leading-order terms provided by the authors of Ref. [65] to determine our first-forbidden shape factors, resulting in very similar forms for $C_{J^\pi}(W_e)$ to those reported by other authors and groups [58, 63, 111, 167].

We note, however, that the shape factors are complicated enough to allow for slight differences in approximation among different groups, and it is difficult to rule out small errors when deriving the final expressions. Although we followed Ref. [65] to select the matrix elements which make up our shape factors, our forms for the various C_{J^π} include both more terms and slightly different terms than theirs.

Our shape factors probably agrees best with those of Ref. [63] after comparing "form factor coefficients," but our C_{J^π} still differ from those of Refs. [63] and [111] by a numerical constant that multiplies a single squared matrix element. In fact, the three derivations all differ from one another. Setting aside this numerical factor, the shape factor reported in Ref. [111] otherwise agrees with ours as long as g_A is taken as negative, instead of positive as reported in the text (although we could only compare shape factors via their expressions in the "Cartesian notation" explained in Ref. [65]).

Finally, our shape factor agrees very well with the one reported in more recent calculations [58, 167], except these calculations include a Coulomb-distorted wave function $I(1,1,1,1;r)$ (as in Ref. [65]) instead of our constant value of 3/2 which is adopted in Ref. [111]. They also make a few other slightly different Coulomb function approximations.

Unlike the allowed shape factors (A.5), those involved in first-forbidden decay depend on the electron energy W_e:

$$C(W_e) = k(1 + aW_e + \mu_1\gamma_1 bW_e^{-1} + cW_e^2), \tag{A.8}$$

where k, a, b, and c are combinations of nuclear matrix elements, Coulomb functions, and the factors $X_\pm$ are defined as

$$X_\pm = \frac{W_0}{3} \pm \frac{\alpha Z}{2R}. \tag{A.9}$$

$W_0 = m_e + Q$ is the maximum β-decay electron energy, and the Coulomb function μ_1 is always set equal to 1 in our calculations. Many authors also account for the screening of the nuclear charge by the atomic electrons (see, e.g., Ref. [65]), but we have left out this screening correction, taking into account only the dominant effect of the nucleus on the electron wave function via the Fermi function F_0 (A.3).

Our shape factor for $J^\pi = 0^-$ transitions is

$$C_{0^-}(W_e) = g_A^2\left(\overline{M}_{01}^2 + \frac{1}{9}M_{[\mathbf{r}\boldsymbol{\sigma}]_0}^2\right) - \frac{2}{3}\frac{\mu_1\gamma_1}{W_e}g_A^2\overline{M}_{01}M_{[\mathbf{r}\boldsymbol{\sigma}]_0}, \tag{A.10}$$

where $\overline{M}_{01}$ is the combination of matrix elements

$$\overline{M}_{01} = M_{\mathbf{p}\boldsymbol{\sigma}} + X_+M_{[\mathbf{r}\boldsymbol{\sigma}]_0}. \tag{A.11}$$

$J^\pi = 1^-$ transitions involve the most complicated shape:

$$\begin{aligned}
C_{1^-}(W_e) = {} & \overline{M}_{11}^2 + \frac{1}{9}\overline{M}_{12}^2 - \frac{4\sqrt{2}}{9\sqrt{3}}g_A M_{[\mathbf{r}\boldsymbol{\sigma}]_1}\overline{M}_{12} \\
& + \frac{4\sqrt{2}}{2\sqrt{3}}g_A M_{[\mathbf{r}\boldsymbol{\sigma}]_1}\overline{M}_{11}W_e - \frac{2}{3}\frac{\mu_1\gamma_1}{W_e}\overline{M}_{11}\overline{M}_{12} \\
& + \frac{8}{27}g_A^2 M_{[\mathbf{r}\boldsymbol{\sigma}]_1}^2 W_e^2 + \frac{1}{9}\left[(W_0 - W_e)^2\overline{M}_{1-}^2 + \lambda_2(W_e^2 - 1)\overline{M}_{1+}^2\right],
\end{aligned} \tag{A.12}$$

where

$$\lambda_2 = \frac{F_1(Z_i + 1, W_e)}{F_0(Z_i + 1, W_e)}\frac{2 + \gamma_2}{2(1 + \gamma_1)} \tag{A.13}$$

is an additional Coulomb function, and we have introduced the new combinations of matrix elements

$$\overline{M}_{11} = M_{\mathbf{p}} - \frac{1}{\sqrt{3}}X_+M_{\mathbf{r}} - \sqrt{\frac{2}{3}}X_-g_A M_{[\mathbf{r}\boldsymbol{\sigma}]_1}, \tag{A.14a}$$

$$\overline{M}_{12} = \sqrt{\frac{2}{3}}g_A M_{[\mathbf{r}\boldsymbol{\sigma}]_1} - \frac{1}{\sqrt{3}}M_{\mathbf{r}}, \tag{A.14b}$$

$$\overline{M}_{1\pm} = \sqrt{\frac{2}{3}}M_{\mathbf{r}} \pm \frac{1}{\sqrt{3}}g_A M_{[\mathbf{r}\boldsymbol{\sigma}]_1}. \tag{A.14c}$$

Finally, the $J^\pi = 2^-$ shape is:

$$C_{2^-}(W_e) = \frac{1}{9}g_A^2 M_{[\mathbf{r}\boldsymbol{\sigma}]_2}^2\left[(W_0 - W_e)^2 + \lambda_2(W_e^2 - 1)\right]. \tag{A.15}$$

The 2^- transitions are called "unique" first-forbidden transitions. The matrix element $M_{[\mathbf{r}\boldsymbol{\sigma}]_2}$ completely separates from the energy-dependent part of the shape factor, and the unique forbidden decays look much like allowed decays, possessing a different energy dependence overall since the squared matrix element is multiplied by the quantity

$$p_\nu^2 + \lambda_2 p_e^2 = (W_0 - W_e)^2 + \lambda_2(W_e^2 - 1). \tag{A.16}$$

The above expressions for first-forbidden β decay have been generated following primarily Ref. [65] and only considering the "dominant terms" [65]. It is worth noting, however, that for high-energy decays of heavy nuclei ($Q_\beta \sim 15$ MeV, $Z \sim 60$, $A \sim 160$) this level of approximation is less acceptable than in more typical β-decay calculations with smaller Q values or mass numbers. With these values for Q, Z, and A the expansion parameters take on values $W_0 R \sim \alpha Z \sim 0.45$ that are not much less than one. In most of the decays we have studied, however, the forbidden transitions make up less than fifty percent of the total rate (see Chapters 7 and 8), and so further corrections are unlikely to impact our results significantly.

APPENDIX B: NUCLEAR SHAPE DEFORMATION

In this appendix we provide additional details regarding the transformation between the laboratory coordinate system and an intrinsic coordinate system attached to a deformed nucleus. We follow very closely to Ref. [74], filling in extra details along the way.

Section B.1: Nuclear matrix elements in the laboratory rest frame

With the lab-frame nuclear wave functions $\Psi_{J,K=0}(\mathbf{\Omega})$ (3.5a) and $\Psi_{J,K>0}(\mathbf{\Omega})$ (3.5b) defined in Chapter 3 we can calculate matrix elements in the lab frame and relate them to the matrix elements we compute in the intrinsic nuclear frame. To this end we need a connection between a tensor operator of rank λ in the lab frame, $\hat{M}_{\lambda\mu}$, and the corresponding operator in the intrinsic frame, $\hat{m}_{\lambda\nu}$ [74, 76]:

$$\hat{M}_{\lambda\mu} = \sum_{\nu=-\lambda}^{\lambda} \mathscr{D}_{\mu\nu}^{\lambda}(\mathbf{\Omega})\, \hat{m}_{\lambda,\nu}. \tag{B.1}$$

The differences between the lab-frame wave functions when $K = 0$ (3.5a) and $K \neq 0$ (3.5a) lead to three types of nuclear matrix elements: those with $K_i = K_f = 0$, those with $K_i = 0$ and $K_f > 0$, and those with both $K_i > 0$ and $K_f > 0$. The simplest of these matrix elements connects two $K = 0$ states:

$$
\begin{aligned}
\langle J_f\, 0\,|\, \hat{M}_{\lambda\mu}\,|\, J_i\, 0\rangle &= \frac{\sqrt{(2J_i+1)(2J_f+1)}}{8\pi^2} \int d\mathbf{\Omega}\, \langle J_f\, 0\,|\, \mathscr{D}_{00}^{J_f\,*}(\mathbf{\Omega}) \left(\sum_{\nu=-\lambda}^{\lambda} \mathscr{D}_{\mu\nu}^{\lambda}(\mathbf{\Omega})\hat{m}_{\lambda\nu} \right) \mathscr{D}_{00}^{J_i}(\mathbf{\Omega})\,|\, J_i\, 0\rangle \\
&= \frac{\sqrt{(2J_i+1)(2J_f+1)}}{8\pi^2} \sum_{\nu=-\lambda}^{\lambda} \langle 0\,|\, \hat{m}_{\lambda\nu}\,|\, 0\rangle \int d\mathbf{\Omega}\, \mathscr{D}_{00}^{J_f\,*}(\mathbf{\Omega})\mathscr{D}_{\mu\nu}^{\lambda}(\mathbf{\Omega})\mathscr{D}_{00}^{J_i}(\mathbf{\Omega}) \\
&= \sqrt{\frac{2J_i+1}{2J_f+1}}\, \langle 0\,|\, \hat{m}_{\lambda,\nu=0}\,|\, 0\rangle\, (\, J_i\, 0\, \lambda\, 0\,|\, J_f\, 0\,)^2\, \delta_{\mu,0},
\end{aligned} \tag{B.2}
$$

where $(\, J_1\, M_1\, J_2\, M_2\,|\, J_f\, M_f\,)$ is a Clebsch-Gordan angular momentum coupling coefficient [76, 79], and we have used the combination properties and the orthogonality of the Wigner D functions to write [75, 76]

$$
\begin{aligned}
\int d\mathbf{\Omega}\, \mathscr{D}_{M_f K_f}^{J_f\,*}(\mathbf{\Omega})\mathscr{D}_{\mu\nu}^{\lambda}(\mathbf{\Omega})\mathscr{D}_{M_i K_i}^{J_i}(\mathbf{\Omega}) &= \frac{8\pi^2}{2J_f+1}(\, \lambda\, \mu\, J_i\, M_i\,|\, J_f\, M_f\,)(\, \lambda\, \nu\, J_i\, K_i\,|\, J_f\, K_f\,) \\
&= \frac{8\pi^2}{2J_f+1}(\, J_i\, M_i\, \lambda\, \mu\,|\, J_f\, M_f\,)(\, J_i\, K_i\, \lambda\, \nu\,|\, J_f\, K_f\,).
\end{aligned} \tag{B.3}
$$

The second line of (B.3) can be obtained from the first by noting that interchanging the two angular momenta on the left-hand side of the Clebsch Gordan coefficients introduces a phase factor $(-1)^{\lambda+J_i-J_f}$. Because both CG coefficients introduce the same factor, and the angular momentum addition rules guarantee that $J_i + \lambda - J_f$ is an integer, the total phase factor must be $+1$. Equation (B.2) demonstrates the lab-frame

matrix element is directly proportional to a matrix element obtained in a body-fixed calculation, multiplied by only a few geometrical factors.

The $K = 0 \to K > 0$ matrix element is computed similarly by using the reflection symmetry of the intrinsic state $| K \rangle$ to combine the two terms in (3.5b):

$$
\begin{aligned}
\langle J_f \, K_f \,|\, \hat{M}_{\lambda\mu} \,|\, J_i \, 0 \rangle = {} & \frac{1}{\sqrt{2}} \frac{\sqrt{(2J_i + 1)(2J_f + 1)}}{8\pi^2} \int \mathrm{d}\boldsymbol{\Omega} \\
& \times 2 \langle K \,|\, \mathscr{D}_{KK}^{J_f \, *}(\boldsymbol{\Omega}) \left(\sum_{\nu = -\lambda}^{\lambda} \mathscr{D}_{\mu\nu}^{\lambda}(\boldsymbol{\Omega}) \hat{m}_{\lambda\nu} \right) \mathscr{D}_{00}^{J_i}(\boldsymbol{\Omega}) \,|\, 0 \rangle,
\end{aligned}
\tag{B.4}
$$

which gives the matrix element

$$
\langle J_f \, K \,|\, \hat{M}_{\lambda\mu} \,|\, J_i \, 0 \rangle = \sqrt{\frac{2(2J_i + 1)}{2J_f + 1}} \, \langle K \,|\, \hat{m}_{\lambda,\nu=K} \,|\, 0 \rangle \, (\, \lambda \, K \, J_i \, 0 \,|\, J_f \, K \,)^2 \, \delta_{\mu,K}.
\tag{B.5}
$$

Eq. (B.5) is similar to the $0 \to 0$ matrix element (B.2); the matrix element is proportional to the corresponding intrinsic matrix element and the appropriate Clebsch-Gordan coefficient. The $K = 0 \to K > 0$ matrix element also yields an extra factor of $\sqrt{2}$. In fact, for the decay of even-even nuclei which have $J_i = K_i = 0$ in their ground states [67, 72], Ref. [74] gives a general expression seen often in the literature for the matrix elements from a $K = 0$ rotation band (Eq. 4–92 in Ref. [74]):

$$
\langle J_f \, K_f \,|\, \hat{M}_{\lambda,\mu=K_f} \,|\, 0 \, 0 \rangle = \frac{\langle K_f \,|\, \hat{m}_{\lambda,\nu=K_f} \,|\, 0 \rangle}{\sqrt{2J_f + 1}} \times
\begin{cases}
1, & K_f = 0 \\[2mm]
\sqrt{2}, & K_f \neq 0.
\end{cases}
\tag{B.6}
$$

Finally, to compute the decays of odd nuclei we need the most-general lab frame matrix element which has both $K_i \neq 0$ and $K_f \neq 0$ since odd nuclei can have $J_i \neq 0$ in their ground state. The matrix element between such states is, after simplifying as much as possible using the reflection symmetry [74]:[1]

$$
\begin{aligned}
\langle J_f \, K_f \,|\, \hat{M}_{\lambda\mu} \,|\, J_i \, K_i \rangle = {} & \frac{\sqrt{(2J_i + 1)(2J_f + 1)}}{8\pi^2} \int \mathrm{d}\boldsymbol{\Omega} \left\{ \langle K_f \,|\, \mathscr{D}_{K_f K_f}^{J_f \, *}(\boldsymbol{\Omega}) \hat{M}_{\lambda\mu} \mathscr{D}_{K_i K_i}^{J_i}(\boldsymbol{\Omega}) \,|\, K_i \rangle \right. \\
& \left. + (-1)^{J_i - K_i} \langle K_f \,|\, \mathscr{D}_{K_f K_f}^{J_f \, *}(\boldsymbol{\Omega}) \hat{M}_{\lambda\mu} \mathscr{D}_{K_i, -K_i}^{J_i}(\boldsymbol{\Omega}) \,|\, \overline{K_i} \rangle \right\}.
\end{aligned}
\tag{B.7}
$$

As before, integrating over the D functions and expanding the lab-frame operators in terms of their intrinsic-

---

[1] As mentioned in Chapter 3, we use a slightly different phase convention than Ref. [74]. As a result, we have a different phase multiplying the interference term than the text does.

frame counterparts yields the nuclear matrix element in terms of intrinsic-frame matrix elements:

$$
\begin{aligned}
\langle J_f\, K_f \,|\, \hat{M}_{\lambda\mu} \,|\, J_i\, K_i \rangle = \sqrt{\frac{2J_i + 1}{2J_f + 1}} \,(\, J_i\, K_i\, \lambda\, [K_f - K_i] \,|\, J_f\, K_f \,)\, \delta_{\mu, K_f - K_i} \\
\times \Big[(\, J_i\, K_i\, \lambda\, [K_f - K_i] \,|\, J_f\, K_f \,)\langle K_f \,|\, \hat{m}_{\lambda, \nu = K_f - K_i} \,|\, K_i \rangle \\
+ (-1)^{J_i - K_i}(\, J_i\, {-}K_i\, \lambda\, [K_f + K_i] \,|\, J_f\, K_f \,)\langle K_f \,|\, \hat{m}_{\lambda, \nu = K_f + K_i} \,|\, \overline{K_i} \rangle \Big].
\end{aligned}
\tag{B.8}
$$

The matrix element (B.8) contains an interference term that affects the decay of odd nuclei. Note, however, that the interference term only contributes if the intrinsic z projection satisfies $-\lambda \leq K_i + K_f \leq \lambda$, where λ is the rank of the operator. Otherwise, the additional term vanishes.

Section B.2: Reduced matrix elements, transition strengths, and cross terms

The strength function $B(\hat{O}_\lambda; J_i K_i \to J_f K_f)$ (Eq. (3.7)) and cross-terms $X(\hat{O}_\lambda^{(1)}, \hat{O}_\lambda^{(2)}; J_i K_i \to J_f K_f)$ (Eq. (3.8)) were defined in Chapter 3 as products of reduced lab-frame matrix elements, and we quoted their relationship to the intrinsic strengths we compute in Chapters 5 and 6. In this appendix, we show how to calculate the total transition strength, inspired by Ref. [80], to all the states with different values J_f in a rotation band (defined in Eq. (3.10)), which is necessary to obtain simple expressions for odd nuclei that have $J_i \neq 0$:

$$
B(\hat{M}_\lambda; J_i\, K_i \to K_f) = \frac{1}{2J_i + 1} \sum_{J_f = |J_i - \lambda|}^{J_i + \lambda} \left| \langle J_f\, K_f \,||\, \hat{M}_\lambda \,||\, J_i\, K_i \rangle \right|^2.
\tag{B.9}
$$

The sum (B.9) only has a single term when $J_i = 0$ and is equivalent to the definition in Chapter 3 of the transition strength for even-even nuclei. The "total cross-term" between two operators is defined similarly:

$$
X(\hat{M}_\lambda^{(1)}, \hat{M}_\lambda^{(2)}; J_i\, K_i \to K_f) = \frac{1}{2J_i + 1} \sum_{J_f = |J_i - \lambda|}^{J_i + \lambda} \langle J_f\, K_f \,||\, \hat{M}_\lambda^{(1)} \,||\, J_i\, K_i \rangle \langle J_f\, K_f \,||\, \hat{M}_\lambda^{(2)} \,||\, J_i\, K_i \rangle^*.
\tag{B.10}
$$

The total strength function and cross-terms enter β-decay calculations, where we need to calculate the squares of different combinations of matrix elements (cf. Appendix A):

$$
\frac{1}{2J_i + 1} \sum_{J_f = |J_i - \lambda|}^{J_i + \lambda} \left| \langle J_f\, K_f \,||\, \hat{M}_\lambda^{(1)} \,||\, J_i\, K_i \rangle + \alpha \langle J_f\, K_f \,||\, \hat{M}_\lambda^{(2)} \,||\, J_i\, K_i \rangle \right|^2.
\tag{B.11}
$$

Expanding the square in Eq. (B.11) and summing over J_f results in a pair of strength functions and a cross term (with α real):

$$
B(\hat{M}_\lambda^{(1)}; J_i\, K_i \to K_f) + \alpha^2 B(\hat{M}_\lambda^{(2)}; J_i\, K_i \to K_f) + 2\alpha \mathrm{Re} X(\hat{M}_\lambda^{(1)}, \hat{M}_\lambda^{(2)}; J_i\, K_i \to K_f).
\tag{B.12}
$$

The reduced matrix elements that enter the expressions for B and X can be calculated directly with the Wigner-Eckart theorem (3.6), and the expression for a general lab-frame nuclear matrix element (B.8) provides the necessary details to calculate the corresponding reduced matrix element:

$$
\begin{aligned}
\langle J_f \, K_f \, || \, \hat{M}_\lambda \, || \, J_i \, K_i \rangle &= \frac{\sqrt{2J_f + 1}}{(\, J_i \, K_i \, \lambda \, [K_f - K_i] \, | \, J_f \, K_f \,)} \langle J_f \, K_f \, | \, \hat{M}_{\lambda, \mu = K_f - K_i} \, | \, J_i \, K_i \rangle \\
&= \sqrt{2J_i + 1} \Big[(\, J_i \, K_i \, \lambda \, [K_f - K_i] \, | \, J_f \, K_f \,) \langle K_f \, | \, \hat{m}_{\lambda, \nu = K_f - K_i} \, | \, K_i \rangle \\
&\quad + (-1)^{J_i - K_i} (\, J_i \, -K_i \, \lambda \, [K_f + K_i] \, | \, J_f \, K_f \,) \langle K_f \, | \, \hat{m}_{\lambda, \nu = K_f + K_i} \, | \, \overline{K_i} \rangle \Big].
\end{aligned}
\tag{B.13}
$$

The transition strength derived from this matrix element is then:

$$
\begin{aligned}
B(\hat{M}_\lambda; J_i \, K_i \to K_f) &= \frac{1}{2J_i + 1} \sum_{J_f = |J_i - \lambda|}^{J_i + \lambda} \left| \langle J_f \, K_f \, || \, \hat{M}_\lambda \, || \, J_i \, K_i \rangle \right|^2 \\
&= \left| \langle K_f \, | \, \hat{m}_{\lambda, \nu = K_f - K_i} \, | \, K_i \rangle \right|^2 \sum_{J_f} (\, J_i \, K_i \, \lambda \, [K_f - K_i] \, | \, J_f \, K_f \,)^2 \\
&\quad + \left| \langle K_f \, | \, \hat{m}_{\lambda, \nu = K_f + K_i} \, | \, \overline{K_i} \rangle \right|^2 \sum_{J_f} (\, J_i \, -K_i \, \lambda \, [K_f + K_i] \, | \, J_f \, K_f \,)^2 \\
&\quad + 2\Re \langle K_f \, | \, \hat{m}_{\lambda, \nu = K_f - K_i} \, | \, K_i \rangle \langle K_f \, | \, \hat{m}_{\lambda, \nu = K_f + K_i} \, | \, \overline{K_i} \rangle^* \\
&\quad \times \sum_{J_f} (\, J_i \, K_i \, \lambda \, [K_f - K_i] \, | \, J_f \, K_f \,)(\, J_i \, -K_i \, \lambda \, [K_f + K_i] \, | \, J_f \, K_f \,).
\end{aligned}
\tag{B.14}
$$

The first two sums over Clebsch-Gordan coefficients are equal to 1, expressing the completeness of angular momentum states. The final sum evaluates to zero, and transition strength in the lab frame is very simply related to the matrix elements we calculate in the intrinsic frame of the deformed nucleus (Eq. (3.10)):

$$
B(\hat{M}_\lambda; J_i \, K_i \to K_f) = \left| \langle K_f \, | \, \hat{m}_{\lambda, \nu = K_f - K_i} \, | \, K_i \rangle \right|^2 + \left| \langle K_f \, | \, \hat{m}_{\lambda, \nu = K_f + K_i} \, | \, \overline{K_i} \rangle \right|^2.
\tag{B.15}
$$

As mentioned following Eq. (B.8), the second term only contributes if $\left| K_i + K_f \right| \le \lambda$.

Cross-terms between different operators should follow immediately as long as both operators have the same rank λ and the matrix elements are between the same angular momentum states. If both conditions are met, the sums over Clebsch-Gordan coefficients when calculating X are the same as when calculating B, so the cross-terms are

$$
\begin{aligned}
X(\hat{M}_\lambda^{(1)}, \hat{M}_\lambda^{(2)}; J_i \, K_i \to K_f) &= \langle K_f \, | \, \hat{m}_{\lambda, \nu = K_f - K_i}^{(1)} \, | \, K_i \rangle \langle K_f \, | \, \hat{m}_{\lambda, \nu = K_f - K_i}^{(2)} \, | \, K_i \rangle^* \\
&\quad + \langle K_f \, | \, \hat{m}_{\lambda, \nu = K_f + K_i}^{(1)} \, | \, \overline{K_i} \rangle \langle K_f \, | \, \hat{m}_{\lambda, \nu = K_f + K_i}^{(2)} \, | \, \overline{K_i} \rangle^*.
\end{aligned}
\tag{B.16}
$$

The reduced matrix elements, transition strengths, and cross-terms for $K_i = K_f = 0$ and $K_i = 0, K_f > 0$ matrix elements are much simpler since they do not have interference terms like Eq. (B.8), and we simply quote the results here. $K = 0 \to K = 0$ transitions have the reduced matrix elements

$$\langle J_f\, 0\, ||\, \hat{M}_\lambda\, ||\, J_i\, 0 \rangle = \sqrt{2J_i + 1}\,(\, J_i\, 0\, \lambda\, 0\, |\, J_f\, 0\,)\langle 0\, |\, \hat{m}_{\lambda,\nu=0}\, |\, 0 \rangle, \tag{B.17}$$

and the corresponding transition strength is given by Eq. (3.9) with $\Theta_K = 1$:

$$B(\hat{M}_\lambda; J_i\, 0 \to 0) = \left|\langle 0\, |\, \hat{m}_{\lambda,\nu=0}\, |\, 0 \rangle\right|^2. \tag{B.18}$$

The $0 \to K_f$ transitions have nearly the same reduced matrix elements:

$$\langle J_f\, K_f\, ||\, \hat{M}_\lambda\, ||\, J_i\, 0 \rangle = \sqrt{2(2J_i + 1)}\,(\, J_i\, 0\, \lambda\, K_f\, |\, J_f\, K_f\,)\langle K_f\, |\, \hat{m}_{\lambda,\nu=K_f}\, |\, 0 \rangle, \tag{B.19}$$

and so B is again given by Eq. (3.9), this time with $\Theta_K = \sqrt{2}$:

$$B(\hat{M}_\lambda; J_i\, 0 \to K_f) = 2\left|\langle K_f\, |\, \hat{m}_{\lambda,\nu=K_f}\, |\, 0 \rangle\right|^2. \tag{B.20}$$

APPENDIX C: ADDITIONAL DETAILS INVOLVING THE DERIVATION OF THE PNFAM

In this appendix we provide a more detailed derivation of the pnFAM equations, whose main points have already been presented in Chapters 5 and 6. The pnFAM equations are derived in a similar way as, e.g., Refs. [98, 105]. M. T. Mustonen worked out the majority of the formalism for even-even nuclei initially [61, 107], and we have subsequently extended the method to include odd nuclei as described in Chapter 6.

Section C.1:   Derivation of the standard pnFAM equations

The pnFAM equations are obtained from the linear response approximation to the time-dependent HFB equations. The linear response equations in the quasiparticle basis (the basis that diagonalizes the Hamiltonian matrix) were written down in Eq. (5.22):

$$i\delta\dot{\mathbb{R}}(t) = [\mathbb{H}_0,\, \delta\mathbb{R}(t)] + [\delta\mathbb{H}(t) + \mathbb{F}(t),\, \mathbb{R}_0]. \tag{5.22}$$

To solve Eq. (5.22), we must define the matrices that contribute to the commutators. These matrices are expressed in the proton-neutron quasiparticle basis $[\,\alpha\,]^\dagger = (\alpha_\nu^\dagger\, \alpha_\nu\, \alpha_\pi^\dagger\, \alpha_\pi)$, obtained from the single particle basis $[\,c\,]^\dagger = (c_n^\dagger\, c_n\, c_p^\dagger\, c_p)$ with the proton-neutron Bogoliubov transformation Eq. (5.12). The HFB matrices $\mathbb{H}_0$ and $\mathbb{R}_0$ appearing in (5.22) are particularly simple; they are block-diagonal in the proton-neutron basis,

$$\mathbb{H}_0 = \begin{pmatrix} \mathbb{H}_0^{(n)} & 0 \\ 0 & \mathbb{H}_0^{(p)} \end{pmatrix}, \qquad \mathbb{R}_0 = \begin{pmatrix} \mathbb{R}_0^{(n)} & 0 \\ 0 & \mathbb{R}_0^{(p)} \end{pmatrix}, \tag{C.1}$$

and are composed of diagonal matrices (Eqs. (5.11) and (5.6)).

To obtain charge-changing solutions of Eq. (5.22) that describe β^- decay, we introduce an external field derived from a charge-changing, non-Hermitian operator $\hat{F} = \sum_{pn} f_{pn} c_p^\dagger c_n$. The proton-neutron Bogoliubov transformation (5.12) provides $\hat{F}$ in the quasiparticle representation,

$$\hat{F} = \frac{1}{2}\,[\,\alpha\,]^\dagger\,\mathbb{F}\,[\,\alpha\,], \qquad \mathbb{F} = \begin{pmatrix} 0 & \mathbb{F}^{(np)} \\ \mathbb{F}^{(pn)} & 0 \end{pmatrix}, \tag{C.2}$$

where the matrices $\mathbb{F}^{(pn)}$ and $\mathbb{F}^{(np)}$ are computed from the matrix elements of $\hat{F}$:

$$\mathbb{F}^{(pn)} \equiv \begin{pmatrix} F_{\pi\nu}^{11} & F_{\pi\nu}^{20} \\ -F_{\pi\nu}^{02} & -F_{\pi\nu}^{\overline{11}} \end{pmatrix} = \begin{pmatrix} (U^\dagger f U)_{\pi\nu} & (U^\dagger f V^*)_{\pi\nu} \\ (V^T f U)_{\pi\nu} & (V^T f V^*)_{\pi\nu} \end{pmatrix}, \qquad \mathbb{F}^{(np)} = \begin{pmatrix} F_{\nu\pi}^{\overline{11}}{}^T & -F_{\nu\pi}^{20}{}^T \\ F_{\nu\pi}^{02}{}^T & -F_{\nu\pi}^{11}{}^T \end{pmatrix}. \tag{C.3}$$

97

We can then define a weak time-dependent and Hermitian external field, generated from Eq. (C.3) and described by the time-dependent quasiparticle matrix

$$\mathbb{F}(t) = \eta \left(\mathbb{F} e^{-i\omega t} + \mathbb{F}^\dagger e^{i\omega t} \right), \tag{C.4}$$

that contributes to Eq. (5.22). The matrix $\mathbb{F}(t)$ has the same block-anti-diagonal form as the underlying operator $\hat{F}$, but only depends on two independent matrices, $F_{\pi\nu}^{11}(t)$ and $F_{\pi\nu}^{20}(t)$, since $\mathbb{F}(t)$ describes a Hermitian operator:

$$\mathbb{F}^{(pn)}(t) = \begin{pmatrix} F_{\pi\nu}^{11}(t) & F_{\pi\nu}^{20}(t) \\ -F_{\pi\nu}^{20*}(t) & -F_{\pi\nu}^{11*}(t) \end{pmatrix}. \tag{C.5}$$

The time-dependent matrices $F_{\pi\nu}^{11}(t)$ and $F_{\pi\nu}^{20}(t)$ couple the various blocks of $\mathbb{F}^{(pn)}$ in Eq. (C.3):

$$\begin{aligned} F_{\pi\nu}^{11}(t) &= F_{\pi\nu}^{11} e^{-i\omega t} + F_{\pi\nu}^{\overline{11}*} e^{i\omega t} \\ F_{\pi\nu}^{20}(t) &= F_{\pi\nu}^{20} e^{-i\omega t} + F_{\pi\nu}^{02*} e^{i\omega t}. \end{aligned} \tag{C.6}$$

The time-dependent generalized density $\mathbb{R}(t)$ and Hamiltonian matrix $\mathbb{H}(t)$ must be Hermitian by definition, and we introduce block-antidiagonal ansatzes for $\delta\mathbb{R}(t)$ and $\delta\mathbb{H}(t)$ similar to the form of $\mathbb{F}(t)$:

$$\delta\mathbb{R}(t) = \begin{pmatrix} 0 & \delta\mathbb{R}^{(pn)\,\dagger}(t) \\ \delta\mathbb{R}^{(pn)}(t) & 0 \end{pmatrix}, \qquad \delta\mathbb{R}^{(pn)}(t) \equiv \begin{pmatrix} P_{\pi\nu}(t) & X_{\pi\nu}(t) \\ -X_{\pi\nu}^*(t) & -P_{\pi\nu}^*(t) \end{pmatrix}, \tag{C.7}$$

$$\delta\mathbb{H}(t) = \begin{pmatrix} 0 & \delta\mathbb{H}^{(pn)\,\dagger}(t) \\ \delta\mathbb{H}^{(pn)}(t) & 0 \end{pmatrix}, \qquad \delta\mathbb{H}^{(pn)}(t) \equiv \begin{pmatrix} \delta H_{\pi\nu}^{11}(t) & \delta H_{\pi\nu}^{20}(t) \\ -\delta H_{\pi\nu}^{20*}(t) & -\delta H_{\pi\nu}^{11*}(t) \end{pmatrix}. \tag{C.8}$$

Because the time-dependent FAM matrices are Hermitian, we obtain two identical pnFAM equations: one for $\delta\mathbb{R}^{(pn)}(t)$ and another for its Hermitian conjugate.

We determine the exact form of $\delta\mathbb{R}^{(pn)}(t)$ by considering the effect of the external field on the HFB ground state. The influence of $\mathbb{F}(t)$ (C.4) can be represented by a small time-dependent unitary transformation [129]:

$$\hat{U}(t) = e^{i\eta\hat{A}(t)} \approx 1 + i\eta\hat{A}(t). \tag{C.9}$$

The operator $\hat{A}(t)$ is Hermitian, and the time-dependent effects are $\mathcal{O}(\eta)$ because $\mathbb{F}(t) \propto \eta$ (C.4). In the

quasiparticle basis, $\hat{A}(t)$ has the form [72, 129]

$$\hat{A}(t) = \frac{1}{2}[\alpha]^{\dagger}\mathbb{A}[\alpha] = \frac{1}{2}\sum_{\mu\nu}\left(A^{11}_{\mu\nu}(t)\alpha^{\dagger}_{\mu}\alpha_{\nu} + A^{20}_{\mu\nu}(t)\alpha^{\dagger}_{\mu}\alpha^{\dagger}_{\nu} - A^{20*}_{\mu\nu}(t)\alpha_{\mu}\alpha_{\nu} - A^{11*}_{\mu\nu}(t)\alpha_{\mu}\alpha^{\dagger}_{\nu}\right), \qquad \text{(C.10)}$$

with $A^{11}(t)$ Hermitian and $A^{20}(t)$ antisymmetric. Under the influence of $\hat{U}(t)$, the HFB ground state becomes time-dependent,

$$|\phi(t)\rangle = U(t)|\phi\rangle \approx |\phi\rangle + i\eta\hat{A}(t)|\phi\rangle + \dots, \qquad \text{(C.11)}$$

and the expectation value of an arbitrary operator $\hat{M}$ is, to linear order in η,

$$\langle\phi(t)|\hat{M}|\phi(t)\rangle \approx \langle\phi|\hat{M}|\phi\rangle + i\eta\langle\phi|[\hat{M},\hat{A}(t)]|\phi\rangle \equiv M_0 + \eta\delta M(t). \qquad \text{(C.12)}$$

With the definition of the generalized density in the quasiparticle basis, Eqs. (5.5) and (5.6),

$$\mathbb{R} \equiv \mathbb{W}^{\dagger}\mathcal{R}\mathbb{W} = \begin{pmatrix} \langle\phi|\alpha^{\dagger}_{\nu}\alpha_{\mu}|\phi\rangle & \langle\phi|\alpha_{\nu}\alpha_{\mu}|\phi\rangle \\ \langle\phi|\alpha^{\dagger}_{\nu}\alpha^{\dagger}_{\mu}|\phi\rangle & \langle\phi|\alpha_{\nu}\alpha^{\dagger}_{\mu}|\phi\rangle \end{pmatrix}, \qquad \text{(C.13)}$$

we can determine the form of $\delta\mathbb{R}(t)$ immediately with Wick's theorem [72, 95], with the result (5.23):

$$\delta\mathbb{R}^{(pn)}(t) = \begin{pmatrix} i\langle\phi|[\alpha^{\dagger}_{\nu}\alpha_{\pi},\hat{A}(t)]|\phi\rangle & i\langle\phi|[\alpha_{\nu}\alpha_{\pi},\hat{A}(t)]|\phi\rangle \\ i\langle\phi|[\alpha^{\dagger}_{\nu}\alpha^{\dagger}_{\pi},\hat{A}(t)]|\phi\rangle & i\langle\phi|[\alpha_{\nu}\alpha^{\dagger}_{\pi},\hat{A}(t)]|\phi\rangle \end{pmatrix} \equiv \begin{pmatrix} 0 & X_{\pi\nu}(t) \\ -X^{*}_{\pi\nu}(t) & 0 \end{pmatrix}. \qquad \text{(C.14)}$$

Direct calculation shows the diagonal matrix elements of $\delta\mathbb{R}^{(pn)}(t)$, i.e., the matrices $P_{\pi\nu}(t)$ in Eq. (C.7), are identically zero. As mentioned in Chapter 5, this is related the requirement that the generalized density must satisfy $\mathbb{R}^2(t) = \mathbb{R}(t)$ in the time-dependent HFB [105]. (Alternatively, the unitary transformation preserves the projectivity of $\mathbb{R}(t)$.) We also see that the matrix $X_{\pi\nu}(t)$ must be antisymmetric (in the sense that $X_{\nu\pi}(t) = -X_{\pi\nu}(t)$) as a result of the commutation relations among the α's.

With all the pieces in place, we evaluate the pnFAM commutator (5.22) and obtain a time-dependent equation for $X_{\pi\nu}(t)$, Eq. (5.24):

$$i\dot{X}_{\pi\nu}(t) = (E_{\pi} + E_{\nu})X_{\pi\nu}(t) + \delta H^{20}_{\pi\nu}(t) + F^{20}_{\pi\nu}(t). \qquad \text{(5.24)}$$

The energy-dependent pnFAM equations follow from substituting the typical ansatzes for $X(t)$ and $\delta H^{20}(t)$

(Eq. (5.25)) [98, 105],

$$X_{\pi\nu}(t) = X_{\pi\nu}(\omega)e^{-i\omega t} + Y_{\pi\nu}^*(\omega)e^{i\omega t}, \tag{C.15}$$

$$\delta H_{\pi\nu}^{20}(t) = \delta H_{\pi\nu}^{20}(\omega)e^{-i\omega t} + \delta H_{\pi\nu}^{02*}(\omega)e^{i\omega t}, \tag{C.16}$$

as well as the definition of $F_{\pi\nu}^{20}(t)$ in Eq. (C.6). Inserting these into Eq. (5.24) yields the pnFAM equations applied in our calculations and written in Eq. (5.26):

$$X_{\pi\nu}(\omega)[(E_\pi + E_\nu) - \omega] + \delta H_{\pi\nu}^{20}(\omega) = -F_{\pi\nu}^{20}, \tag{C.17a}$$

$$Y_{\pi\nu}(\omega)[(E_\pi + E_\nu) + \omega] + \delta H_{\pi\nu}^{02}(\omega) = -F_{\pi\nu}^{02}. \tag{C.17b}$$

C.1.1:   Determination of the perturbed mean fields $\delta H(\omega)$

Beginning from a static HFB solution with quasiparticle energies $\{E_\pi\}$ and $\{E_\nu\}$ and a choice of the charge-changing external field, we solve the equations (C.17) iteratively for $X(\omega)$ and $Y(\omega)$. The most complicated and time-consuming part of the calculation is the determination of $\delta H^{20}(\omega)$ and $\delta H^{02}(\omega)$ from the proton-neutron densities $X(\omega)$ and $Y(\omega)$, as mentioned briefly in Chapter 5.

To calculate $\delta H^{20}(\omega)$ and $\delta H^{02}(\omega)$ we need the energy-dependent perturbed densities $\delta\rho(\omega)$ and $\delta\kappa(\omega)$ and also the perturbed fields $\delta h(\omega)$ and $\delta\Delta(\omega)$. The densities are calculated with the proton-neutron Bogoliubov transformation, which transforms the charge-changing block of the generalized density into the single-particle basis:

$$\delta\mathcal{R}^{(pn)}(t) = \mathbb{W}^{(p)}\,\delta\mathbb{R}^{(pn)}(t)\,\mathbb{W}^{(n)\dagger}. \tag{C.18}$$

Inserting our ansatz (C.15) for $X(t)$ yields corresponding equations for the density and the pairing tensor:

$$\delta\rho_{pn}(t) = \delta\rho_{pn}(\omega)e^{-i\omega t} + \delta\rho_{np}^*(\omega)e^{i\omega t}, \tag{C.19a}$$

$$\delta\kappa_{pn}(t) = \delta\kappa_{pn}^{(+)}(\omega)e^{-i\omega t} + \delta\kappa_{pn}^{(-)}(\omega)e^{i\omega t}. \tag{C.19b}$$

The matrices $\delta\rho_{pn}(\omega)$ and $\delta\rho_{np}(\omega)$ are independent of one another, as are $\delta\kappa_{\pi\nu}^{(\pm)}(\omega)$, and the two matrices $\delta\kappa^{(\pm)}(\omega)$ must each be antisymmetric (see, e.g., Ref. [98]). The energy-dependent perturbed densities are

calculated with the matrices U, V, $X(\omega)$, and $Y(\omega)$:

$$\delta\rho_{pn}(\omega) = U_p X(\omega) V_n^T - V_p^* Y(\omega) U_n^\dagger, \tag{C.20a}$$

$$\delta\rho_{np}(\omega) = V_n^* Y^T(\omega) U_p^\dagger - U_n X^T(\omega) V_p^T, \tag{C.20b}$$

$$\delta\kappa_{pn}^{(+)}(\omega) = U_p X(\omega) U_n^T - V_p^* Y(\omega) V_n^\dagger, \tag{C.20c}$$

$$\delta\kappa_{pn}^{(-)}(\omega) = U_p Y(\omega) U_n^T - V_p^* X^*(\omega) V_n^\dagger. \tag{C.20d}$$

Because there are no proton-neutron-mixed contributions to the ground state energy, and since charge-changing Skyrme mean fields are proportional to the charge-changing densities [61], we can write write

$$\delta h_{pn}(t) = \delta h_{pn}(\omega) e^{-i\omega t} + \delta h_{np}^*(\omega) e^{i\omega t},$$
$$\delta\Delta_{pn}(t) = \delta\Delta_{pn}^{(+)}(\omega) e^{-i\omega t} + \delta\Delta_{pn}^{(-)}(\omega) e^{i\omega t}, \tag{C.21}$$

i.e., $\delta h(t)$ and $\delta\Delta(t)$ are linear in $\delta\rho(t)$ and $\delta\kappa(t)$, respectively. These fields form the charge-changing Hamiltonian matrix $\delta\mathcal{H}^{(pn)}(t)$, which can finally be converted back to the quasiparticle basis with $\mathbb{W}$. The resulting anti-diagonal blocks of the Hamiltonian matrix in the quasiparticle basis are

$$\delta H_{\pi\nu}^{20}(\omega) = U_p^\dagger \delta h_{pn}(\omega) V_n^* + U_p^\dagger \delta\Delta_{pn}^{(+)}(\omega) U_n^* - V_p^\dagger \delta\Delta_{pn}^{(-)*}(\omega) V_n^* - V_p^\dagger [\delta h_{np}(\omega)]^T U_n^*, \tag{C.22a}$$

$$\delta H_{\pi\nu}^{02}(\omega) = -V_p^T \delta h_{pn}(\omega) U_n - V_p^T \delta\Delta_{pn}^{(+)}(\omega) V_n + U_p^T \delta\Delta_{pn}^{(-)*}(\omega) U_n + U_p^T [\delta h_{np}(\omega)]^T V_n. \tag{C.22b}$$

In this way we obtain new values of the mean-field matrix elements; they subsequently feed back into $X(\omega)$ and $Y(\omega)$ via the pnFAM equations.

Section C.2:   Modifications of the pnFAM equations for odd nuclei

Differences between the pnFAM equations for even-even and odd nuclei result from the introduction of a statistical ensemble described with the density operator $\hat\rho^{\text{EFA}}$ (6.4). This ensemble is responsible for the lack of projectivity of the generalized density, $\mathbb{R}^2 \neq \mathbb{R}$, caused by non-zero quasiparticle occupation probabilities in the ensemble.

In the previous section, we found an ansatz for the perturbed generalized density $\delta\mathbb{R}(t)$ by considering the evolution in time of the HFB ground state: $|\phi\rangle \to \exp(i\eta A(t))|\phi\rangle$. The corresponding action for a system described by a density operator is to evolve $\hat\rho$ with time [129],

$$\hat\rho(t) = U(t)\hat\rho_0 U^\dagger(t) \approx (1 + i\eta S(t))\hat\rho_0(1 - i\eta S(t)) \approx \hat\rho_0 + i\eta[S(t), \hat\rho_0], \tag{C.23}$$

where $S(t)$ is a Hermitian operator (like $A(t)$ in the even-even case (C.10)). The proton-neutron perturbed density $\delta\mathbb{R}^{(pn)}(t)$ still has the form (C.7), but now the matrices $P_{\pi\nu}(t)$ and $X_{\pi\nu}(t)$ are calculated as traces in Fock space [129], e.g.,

$$P_{\pi\nu}(t) = \frac{\text{Tr}\{\delta\hat{\rho}(t)\alpha_\nu^\dagger\alpha_\pi\}}{\text{Tr}\,\hat{\rho}} = \frac{1}{\text{Tr}\,\hat{\rho}_0}i\,\text{Tr}\{[\hat{S}(t),\,\hat{\rho}_0]\alpha_\nu^\dagger\alpha_\pi\}. \tag{C.24}$$

With the cyclic invariance of the trace [114, 129] we find that neither $P_{\pi\nu}(t)$ nor $X_{\pi\nu}(t)$ vanish,

$$P_{\pi\nu}(t) = i(f_\nu - f_\pi)S_{\pi\nu}^{11}(t), \tag{C.25a}$$

$$X_{\pi\nu}(t) = i(1 - f_\nu - f_\pi)S_{\pi\nu}^{20}(t), \tag{C.25b}$$

so the proton-neutron perturbed density $\delta\mathbb{R}^{(pn)}(t)$ is represented by the matrix (6.9):

$$\delta\mathbb{R}^{(pn)}(t) = \begin{pmatrix} P_{\pi\nu}(t) & X_{\pi\nu}(t) \\ -X_{\pi\nu}^*(t) & -P_{\pi\nu}^*(t) \end{pmatrix}. \tag{6.9}$$

The form of $\mathbb{R}_0^{\text{EFA}}$ (6.7) introduces additional factors in the commutator (5.22). The perturbed mean field and the external field are multiplied by combinations of the factors f_μ defined in Chapter 6:

$$[\delta\mathbb{H}(t) + \mathbb{F}(t),\,\mathbb{R}_0^{\text{EFA}}]^{(pn)} = \begin{pmatrix} (f_\nu - f_\pi)(F_{\pi\nu}^{11}(t) + \delta H_{\pi\nu}^{11}(t)) & (1 - f_\nu - f_\pi)(F_{\pi\nu}^{20}(t) + \delta H_{\pi\nu}^{20}(t)) \\ (1 - f_\nu - f_\pi)(F_{\pi\nu}^{20*}(t) + \delta H_{\pi\nu}^{20*}(t)) & (f_\nu - f_\pi)(F_{\pi\nu}^{11*}(t) + \delta H_{\pi\nu}^{11*}(t)) \end{pmatrix}, \tag{C.26}$$

and we use the same matrix descriptions of $\mathbb{F}(t)$ and $\delta\mathbb{H}(t)$ as in the even-even pnFAM (Eqs. (C.4) and (C.8)). The resulting time-dependent pnFAM equations, generalized to odd nuclei in the equal-filling approximation, are Eqs. (6.10):

$$i\dot{X}_{\pi\nu}(t) = (E_\pi + E_\nu)X_{\pi\nu}(t) + (1 - f_\nu - f_\pi)(F_{\pi\nu}^{20}(t) + \delta H_{\pi\nu}^{20}(t)), \tag{C.27a}$$

$$i\dot{P}_{\pi\nu}(t) = (E_\pi - E_\nu)P_{\pi\nu}(t) + (f_\nu - f_\pi)(F_{\pi\nu}^{11}(t) + \delta H_{\pi\nu}^{11}(t)). \tag{C.27b}$$

By introducing the ansatzes (6.11)

$$\delta R_{\pi\nu}^{11}(t) = P_{\pi\nu}(\omega)e^{-i\omega t} + Q_{\pi\nu}^*(\omega)e^{i\omega t}, \tag{C.28a}$$

$$\delta R_{\pi\nu}^{20}(t) = X_{\pi\nu}(\omega)e^{-i\omega t} + Y_{\pi\nu}^*(\omega)e^{i\omega t}, \tag{C.28b}$$

as well as

$$\delta H_{\pi\nu}^{11}(t) = \delta H_{\pi\nu}^{11}(\omega)e^{-i\omega t} + \delta H_{\pi\nu}^{\overline{11}*}(\omega)e^{i\omega t}, \tag{C.29a}$$

$$\delta H_{\pi\nu}^{20}(t) = \delta H_{\pi\nu}^{20}(\omega)e^{-i\omega t} + \delta H_{\pi\nu}^{02*}(\omega)e^{i\omega t}, \tag{C.29b}$$

and taking the time derivatives of $P(t)$ $X(t)$, we obtain the energy-dependent pnFAM equations, Eqs. (6.12):

$$X_{\pi\nu}(\omega)[(E_\pi + E_\nu) - \omega] = -(1 - f_\nu - f_\pi)[F_{\pi\nu}^{20} + \delta H_{\pi\nu}^{20}(\omega)], \tag{C.30a}$$

$$Y_{\pi\nu}(\omega)[(E_\pi + E_\nu) + \omega] = -(1 - f_\nu - f_\pi)[F_{\pi\nu}^{02} + \delta H_{\pi\nu}^{02}(\omega)], \tag{C.30b}$$

$$P_{\pi\nu}(\omega)[(E_\pi - E_\nu) - \omega] = -(f_\nu - f_\pi)[F_{\pi\nu}^{11} + \delta H_{\pi\nu}^{11}(\omega)], \tag{C.30c}$$

$$Q_{\pi\nu}(\omega)[(E_\pi - E_\nu) + \omega] = -(f_\nu - f_\pi)[F_{\pi\nu}^{\overline{11}} + \delta H_{\pi\nu}^{\overline{11}}(\omega)]. \tag{C.30d}$$

C.2.1:   The perturbed mean fields $\delta H(\omega)$ in the pnFAM for odd nuclei

We determine the matrices $\delta H(\omega)$ in the pnFAM for odd nuclei in a similar way as in the even-even version. The introduction of the matrices $P(\omega)$ and $Q(\omega)$ has two practical effects, however: the densities $\delta\rho(\omega)$ and $\delta\kappa(\omega)$ now depend on $P(\omega)$ and $Q(\omega)$ via the proton-neutron Bogoliubov transformation, and we must calculate the diagonal (11 and $\overline{11}$) blocks of $\mathbb{F}^{(pn)}$ and $\delta\mathbb{H}^{(pn)}(\omega)$ for the iterative solution of P and Q.

The diagonal blocks of $\mathbb{F}^{(pn)}$ were given in Eq. (C.3), and the pnFAM expressions for the perturbed densities in odd nuclei, corresponding to Eqs. (C.20) and including $P(\omega)$ and $Q(\omega)$, are:

$$\delta\rho_{pn}(\omega) = U_p P(\omega)U_n^\dagger - V_p^* Q(\omega)V_n^T + U_p X(\omega)V_n^T - V_p^* Y(\omega)U_n^\dagger, \tag{C.31a}$$

$$\delta\rho_{np}(\omega) = -V_n^* P^T(\omega)V_p^T + U_n Q^T(\omega)U_p^\dagger - U_n X^T(\omega)V_p^T + V_n^* Y^T(\omega)U_p^\dagger, \tag{C.31b}$$

$$\delta\kappa_{pn}^{(+)} = U_p P(\omega)V_n^\dagger - V_p^* Q(\omega)U^T + U_p X(\omega)U_n^T - V_p^* Y(\omega)V_n^\dagger, \tag{C.31c}$$

$$\delta\kappa_{pn}^{(-)} = -V_p^* P^*(\omega)U_n^T + U_p Q^*(\omega)V_n^\dagger - V_p^* X^*(\omega)V_n^\dagger + U_p Y^*(\omega)U_n^T. \tag{C.31d}$$

Finally, the diagonal blocks of $\delta\mathbb{H}^{(pn)}(\omega)$ are

$$\delta H_{\pi\nu}^{11}(\omega) = U_p^\dagger \delta h_{pn}(\omega)U_n - V_p^\dagger (\delta h_{np}(\omega))^T V_n + U_p^\dagger \delta\Delta_{pn}^{(+)}(\omega)V_n - V_p^\dagger \delta\Delta_{pn}^{(-)*}(\omega)U_n, \tag{C.32a}$$

$$\delta H_{\pi\nu}^{\overline{11}}(\omega) = -V_p^T \delta h_{pn}(\omega)V_n^* + U_p^T (\delta h_{np}(\omega))^T U_n^* - V_p^T \delta\Delta_{pn}^{(+)}(\omega)U_n^* + U_p^T \delta\Delta_{pn}^{(-)*}(\omega)V_n^*. \tag{C.32b}$$

REFERENCES

[1] E. M. Burbidge, G. R. Burbidge, W. A. Fowler, and F. Hoyle, Rev. Mod. Phys. **29**, 547 (1957).

[2] A. G. W. Cameron, Publications of the Astronomical Society of the Pacific **69**, 201 (1957).

[3] J. J. Cowan, F.-K. Thielemann, and J. W. Truran, Physics Reports **208**, 267 (1991).

[4] M. Arnould, S. Goriely, and K. Takahashi, Physics Reports **450**, 97 (2007).

[5] F.-K. Thielemann, A. Arcones, R. Käppeli, M. Liebendörfer, T. Rauscher, C. Winteler, C. Fröhlich, I. Dillmann, T. Fischer, G. Martinez-Pinedo, K. Langanke, K. Farouqi, K.-L. Kratz, I. Panov, and I. Korneev, Progress in Particle and Nuclear Physics **66**, 346 (2011), Particle and Nuclear Astrophysics, International Workshop on Nuclear Physics, 32nd Course.

[6] G. Audi, F. Kondev, M. Wang, B. Pfeiffer, X. Sun, J. Blachot, and M. MacCormick, Chinese Physics C **36**, 1157 (2012).

[7] M. Arnould and S. Goriely, Physics Reports **384**, 1 (2003).

[8] R. K. Wallace and S. E. Woosley, The Astrophysical Journal Supplement Series **45**, 389 (1981).

[9] C. Travaglio, R. Gallino, E. Arnone, J. Cowan, F. Jordan, and C. Sneden, The Astrophysical Journal **601**, 864 (2004).

[10] C. Fröhlich, G. Martínez-Pinedo, M. Liebendörfer, F.-K. Thielemann, E. Bravo, W. R. Hix, K. Langanke, and N. T. Zinner, Phys. Rev. Lett. **96**, 142502 (2006).

[11] J. Pruet, R. D. Hoffman, S. E. Woosley, H.-T. Janka, and R. Buras, The Astrophysical Journal **644**, 1028 (2006).

[12] S. Wanajo, The Astrophysical Journal **647**, 1323 (2006).

[13] C. Sneden, J. J. Cowan, and R. Gallino, Annual Review of Astronomy and Astrophysics **46**, 241 (2008).

[14] S. Bisterzo, C. Travaglio, R. Gallino, M. Wiescher, and F. Käppeler, The Astrophysical Journal **787**, 10 (2014).

[15] F. Käppeler, R. Gallino, S. Bisterzo, and W. Aoki, Rev. Mod. Phys. **83**, 157 (2011).

[16] F. Kaeppeler, H. Beer, K. Wisshak, D. D. Clayton, R. L. Macklin, and R. A. Ward, The Astrophysical Journal **257**, 821 (1982).

[17] C. Arlandini, F. Käppeler, K. Wisshak, R. Gallino, M. Lugaro, M. Busso, and O. Straniero, The Astrophysical Journal **525**, 886 (1999).

[18] R. Surman, J. Engel, J. R. Bennett, and B. S. Meyer, Phys. Rev. Lett. **79**, 1809 (1997).

[19] M. R. Mumpower, G. C. McLaughlin, and R. Surman, The Astrophysical Journal **752**, 117 (2012).

[20] M. R. Mumpower, G. C. McLaughlin, and R. Surman, Phys. Rev. C **85**, 045801 (2012).

[21] S. Wanajo, The Astrophysical Journal Letters **666**, L77 (2007).

[22] H. E. Suess and H. C. Urey, Rev. Mod. Phys. **28**, 53 (1956).

[23] K. Marti and H. D. Zeh, Meteoritics **20**, 311 (1985).

[24] S. Goriely, European Physical Journal A **51**, 22 (2015).

[25] M. Mumpower, R. Surman, D. L. Fang, M. Beard, and A. Aprahamian, Journal of Physics G: Nuclear and Particle Physics **42**, 034027 (2015).

[26] M. Mumpower, R. Surman, and A. Aprahamian, Journal of Physics: Conference Series **599**, 012031 (2015).

[27] M. Mumpower, R. Surman, G. McLaughlin, and A. Aprahamian, Progress in Particle and Nuclear Physics **86**, 86 (2016).

[28] G. J. Wasserburg, M. Busso, and R. Gallino, The Astrophysical Journal Letters **466**, L109 (1996).

[29] J. W. Truran, J. J. Cowan, C. A. Pilachowski, and C. Sneden, Publications of the Astronomical Society of the Pacific **114**, 1293 (2002).

[30] J. J. Cowan and C. Sneden, Nature **440**, 1151 (2006).

[31] A. Arcones and F.-K. Thielemann, Journal of Physics G: Nuclear and Particle Physics **40**, 013201 (2013).

[32] Y.-Z. Qian, P. Vogel, and G. J. Wasserburg, The Astrophysical Journal **494**, 285 (1998).

[33] Y.-Z. Qian and G. Wasserburg, Physics Reports **333–334**, 77 (2000).

[34] Y.-Z. Qian and G. J. Wasserburg, The Astrophysical Journal **559**, 925 (2001), astro-ph/0106085 .

[35] Y.-Z. Qian and G. J. Wasserburg, The Astrophysical Journal **567**, 515 (2002).

[36] Y.-Z. Qian and G. Wasserburg, Physics Reports **442**, 237 (2007), the Hans Bethe Centennial Volume 1906-2006.

[37] Y.-Z. Qian and G. J. Wasserburg, The Astrophysical Journal **687**, 272 (2008).

[38] H. Li, X. Shen, S. Liang, W. Cui, and B. Zhang, Publications of the Astronomical Society of the Pacific **125**, 143 (2013).

[39] C. J. Hansen, F. Montes, and A. Arcones, The Astrophysical Journal **797**, 123 (2014).

[40] H.-T. Janka, F. Hanke, L. Hüdepohl, A. Marek, B. Müller, and M. Obergaulinger, Progress of Theoretical and Experimental Physics **2012** (2012), 10.1093/ptep/pts067.

[41] Y.-Z. Qian, The Astrophysical Journal Letters **534**, L67 (2000).

[42] S. Goriely, J.-L. Sida, J.-F. Lemaître, S. Panebianco, N. Dubray, S. Hilaire, A. Bauswein, and H.-T. Janka, Phys. Rev. Lett. **111**, 242502 (2013).

[43] S. Goriely and G. M. Pinedo, Nuclear Physics A **944**, 158 (2015), special Issue on Superheavy Elements.

[44] J. d. J. Mendoza-Temis, M.-R. Wu, K. Langanke, G. Martínez-Pinedo, A. Bauswein, and H.-T. Janka, Phys. Rev. C **92**, 055805 (2015).

[45] K. Hotokezaka, T. Piran, and M. Paul, Nat Phys , 1042 (2015).

[46] F.-K. Thielemann, Nat Phys **11**, 993 (2015).

[47] A. G. W. Cameron, The Astrophysical Journal **587**, 327 (2003).

[48] N. Nishimura, T. Takiwaki, and F.-K. Thielemann, The Astrophysical Journal **810**, 109 (2015).

[49] S. Shibagaki, T. Kajino, G. J. Mathews, S. Chiba, S. Nishimura, and G. Lorusso, "Relative contributions of the weak, main and fission-recycling r-process," (2015), arXiv:1505.02257 .

[50] B. Wehmeyer, M. Pignatari, and F.-K. Thielemann, Monthly Notices of the Royal Astronomical Society **452**, 1970 (2015).

[51] O. L. Caballero, A. Arcones, I. N. Borzov, K. Langanke, and G. Martinez-Pinedo, "Local and global effects of beta decays on r-process," (2014), arXiv:1405.0210 .

[52] K. Langanke and G. Martínez-Pinedo, Journal of Physics: Conference Series **580**, 012033 (2015).

[53] M. Eichler, A. Arcones, A. Kelic, O. Korobkin, K. Langanke, T. Marketin, G. Martinez-Pinedo, I. Panov, T. Rauscher, S. Rosswog, C. Winteler, N. T. Zinner, and F.-K. Thielemann, The Astrophysical Journal **808**, 30 (2015).

[54] M. Madurga *et al.*, Phys. Rev. Lett. **109**, 112501 (2012).

[55] P. Möller, B. Pfeiffer, and K.-L. Kratz, Phys. Rev. C **67**, 055802 (2003).

[56] R. H. Cyburt, A. M. Amthor, R. Ferguson, Z. Meisel, K. Smith, S. Warren, A. Heger, R. D. Hoffman, T. Rauscher, A. Sakharuk, H. Schatz, F. K. Thielemann, and M. Wiescher, The Astrophysical Journal Supplement Series **189**, 240 (2010).

[57] H. Klapdor, J. Metzinger, and T. Oda, Atomic Data and Nuclear Data Tables **31**, 81 (1984).

[58] T. Marketin, L. Huther, and G. Martínez-Pinedo, "Large scale evaluation of beta-decay rates of r-process nuclei with the inclusion of first-forbidden transitions," (2015), arXiv:1507.07442 .

[59] T. Marketin, L. Huther, and G. Martínez-Pinedo, AIP Conference Proceedings **1681**, 050009 (2015).

[60] M. T. Mustonen and J. Engel, Phys. Rev. C **93**, 014304 (2016).

[61] M. T. Mustonen, T. Shafer, Z. Zenginerler, and J. Engel, Phys. Rev. C **90**, 024308 (2014).

[62] T. Shafer, J. Engel, C. Fröhlich, G. C. McLaughlin, M. Mumpower, and R. Surman, (in preparation).

[63] H. Schopper, *Weak Interactions and Nuclear Beta Decay* (North-Holland Pub. Co., 1966).

[64] K. S. Krane, *Introductory Nuclear Physics* (Wiley, 1987).

[65] H. Behrens and W. Bühring, *Electron Radial Wave Functions and Nuclear Beta-decay (The International Series of Monographs on Physics)* (Oxford University Press, 1982).

[66] K. Olive and P. D. Group, Chinese Physics C **38**, 090001 (2014).

[67] J.-L. Basdevant, J. Rich, and M. Spiro, *Fundamentals in Nuclear Physics: From Nuclear Structure to Cosmology (Advanced Texts in Physics S)* (Springer, 2005).

[68] R. Nave, "Relativistic Momentum," `http://hyperphysics.phy-astr.gsu.edu/hbase/relativ/relmom.html#c1` (2015), accessed October 18, 2015.

[69] J. D. Jackson, *Classical Electrodynamics*, 3rd ed. (John Wiley & Sons, Inc., 1999).

[70] I. N. Borzov, Phys. Rev. C **67**, 025802 (2003).

[71] J. C. Hardy and I. S. Towner, Phys. Rev. C **71**, 055501 (2005).

[72] P. Ring and P. Schuck, *The Nuclear Many-Body Problem (Theoretical and Mathematical Physics)* (Springer, 2005).

[73] R. F. Casten, *Nuclear Structure from a Simple Perspective (Oxford Studies in Nuclear Physics)* (Oxford University Press, 2001).

[74] A. Bohr and B. R. Mottelson, *Nuclear Structure, Volume II: Nuclear Deformations* (W. A. Benjamin, 1975).

[75] J. M. Eisenberg, *Nuclear Theory, Vol. 1: Nuclear Models* (American Elsevier, 1975).

[76] A. Bohr and B. R. Mottelson, *Nuclear Structure* (World Scientific Pub Co Inc, 1998).

[77] M. Stoitsov, J. Dobaczewski, W. Nazarewicz, and P. Ring, Computer Physics Communications **167**, 43 (2005).

[78] M. Stoitsov, N. Schunck, M. Kortelainen, N. Michel, H. Nam, E. Olsen, J. Sarich, and S. Wild, Computer Physics Communications **184**, 1592 (2013).

[79] K. Gottfried and T.-M. Yan, *Quantum Mechanics: Fundamentals (Graduate Texts in Contemporary Physics)* (Springer, 2004).

[80] J. Krumlinde and P. Möller, Nuclear Physics A **417**, 419 (1984).

[81] D. Gambacurta, M. Grasso, and J. Engel, Phys. Rev. C **92**, 034303 (2015).

[82] P. Hohenberg and W. Kohn, Phys. Rev. **136**, B864 (1964).

[83] W. Kohn and L. J. Sham, Phys. Rev. **140**, A1133 (1965).

[84] C. Fiolhais, F. Nogueira, and M. A. L. Marques, eds., *A Primer in Density Functional Theory*, Lecture Notes in Physics (Springer-Verlag, 2003).

[85] J. Engel, Phys. Rev. C **75**, 014306 (2007).

[86] M. Bender, P.-H. Heenen, and P.-G. Reinhard, Rev. Mod. Phys. **75**, 121 (2003).

[87] J. Dobaczewski and J. Dudek, Acta Phys. Pol. B **27** (1996).

[88] E. Perlińska, S. G. Rohoziński, J. Dobaczewski, and W. Nazarewicz, Phys. Rev. C **69**, 014316 (2004).

[89] M. Bender, J. Dobaczewski, J. Engel, and W. Nazarewicz, Phys. Rev. C **65**, 054322 (2002).

[90] A. Messiah, *Quantum Mechanics, Vol. 2* (Halsted Pr, 1963).

[91] T. H. R. Skyrme, Philosophical Magazine **1**, 1043 (1956).

[92] T. Skyrme, Nuclear Physics **9**, 615 (1958-1959).

[93] S. Fayans, S. Tolokonnikov, E. Trykov, and D. Zawischa, Nuclear Physics A **676**, 49 (2000).

[94] E. Runge and E. K. U. Gross, Phys. Rev. Lett. **52**, 997 (1984).

[95] J.-P. Blaizot and G. Ripka, *Quantum Theory of Finite Systems* (The MIT Press, 1985).

[96] P. Avogadro and T. Nakatsukasa, Phys. Rev. C **87**, 014331 (2013).

[97] T. Nakatsukasa, T. Inakura, and K. Yabana, Phys. Rev. C **76**, 024318 (2007).

[98] P. Avogadro and T. Nakatsukasa, Phys. Rev. C **84**, 014314 (2011).

[99] M. Bender, "QRPA matrix elements in an energy functional formalism," (1999), unpublished.

[100] M. Bender, "A generalized Skyrme interaction," (2002), unpublished.

[101] A. Bulgac, Phys. Rev. C **65**, 051305 (2002).

[102] L. N. Oliveira, E. K. U. Gross, and W. Kohn, Phys. Rev. Lett. **60**, 2430 (1988).

[103] S. Kurth, M. Marques, M. Lüders, and E. K. U. Gross, Phys. Rev. Lett. **83**, 2628 (1999).

[104] M. Kortelainen, "Some notes about time-reversal operator, HFB in axial symmetry, etc." (2011), unpublished.

[105] T. Nikšić, N. Kralj, T. Tutiš, D. Vretenar, and P. Ring, Phys. Rev. C **88**, 044327 (2013).

[106] M. Kortelainen, "Fam and $L \neq 0$ multipoles (incomplete working notes)," (2012), unpublished.

[107] M. T. Mustonen, "Notes on the finite amplitude method," (2014), unpublished.

[108] D. J. Rowe, *Nuclear Collective Motion* (World Scientific, River Edge, SG, 2010).

[109] N. Hinohara, M. Kortelainen, and W. Nazarewicz, Phys. Rev. C **87**, 064309 (2013).

[110] N. Hinohara, M. Kortelainen, W. Nazarewicz, and E. Olsen, Phys. Rev. C **91**, 044323 (2015).

[111] J. Suhonen, Nuclear Physics A **563**, 205 (1993).

[112] S. Perez-Martin and L. M. Robledo, Phys. Rev. C **78**, 014304 (2008).

[113] N. Schunck, J. Dobaczewski, J. McDonnell, W. Satuła, J. Sheikh, A. Staszczak, M. Stoitsov, and P. Toivanen, Computer Physics Communications **183**, 166 (2012).

[114] S. Perez-Martin and L. M. Robledo, Phys. Rev. C **76**, 064314 (2007).

[115] N. Schunck, J. Dobaczewski, J. McDonnell, J. Moré, W. Nazarewicz, J. Sarich, and M. V. Stoitsov, Phys. Rev. C **81**, 024316 (2010).

[116] D. Tarpanov, J. Toivanen, J. Dobaczewski, and B. G. Carlsson, Phys. Rev. C **89**, 014307 (2014).

[117] E. Lipparini and S. Stringari, Annals of Physics **173**, 411 (1987).

[118] E. Lipparini and S. Stringari, Physics Reports **175**, 103 (1989).

[119] N. Chamel, Phys. Rev. C **82**, 061307 (2010).

[120] J. A. H. Sr. and R. A. Sorensen, Nuclear Physics A **98**, 542 (1967).

[121] K. Muto, E. Bender, and H. V. Klapdor, Zeitschrift fur Physik A Hadrons and Nuclei **333**, 125 (1989).

[122] P. Möller and J. Randrup, Nuclear Physics A **514**, 1 (1990).

[123] K. Muto, E. Bender, T. Oda, and H. V. Klapdor-Kleingrothaus, Zeitschrift fur Physik A Hadrons and Nuclei **341**, 407 (1992).

[124] P. Sarriguren, E. Moya de Guerra, and A. Escuderos, Phys. Rev. C **64**, 064306 (2001).

[125] P. Sarriguren, Phys. Rev. C **91**, 044304 (2015).

[126] J. M. Boillos and P. Sarriguren, Phys. Rev. C **91**, 034311 (2015).

[127] S. Stringari, E. Lipparini, G. Orlandini, M. Traini, and R. Leonardi, Nuclear Physics A **309**, 177 (1978).

[128] A. L. Goodman, Nuclear Physics A **352**, 30 (1981).

[129] H. Sommermann, Annals of Physics **151**, 163 (1983).

[130] J. L. Egido and P. Ring, Journal of Physics G: Nuclear and Particle Physics **19**, 1 (1993).

[131] P. Ring, L. Robledo, J. Egido, and M. Faber, Nuclear Physics A **419**, 261 (1984).

[132] D. Vautherin and N. Mau, Nuclear Physics A **422**, 140 (1984).

[133] F. Alasia, O. Civitarese, and M. Reboiro, Phys. Rev. C **39**, 1012 (1989).

[134] P. Chomaz, D. Vautherin, and N. V. Mau, Physics Letters B **242**, 313 (1990).

[135] K. Hagino and F. Minato, Phys. Rev. C **80**, 047301 (2009).

[136] Y. Niu, N. Paar, D. Vretenar, and J. Meng, Physics Letters B **681**, 315 (2009).

[137] Y. F. Niu, N. Paar, D. Vretenar, and J. Meng, Journal of Physics: Conference Series **312**, 042017 (2011).

[138] F. Minato and K. Hagino, Phys. Rev. C **80**, 065808 (2009).

[139] N. Paar, G. Colò, E. Khan, and D. Vretenar, Phys. Rev. C **80**, 055801 (2009).

[140] M. Mumpower, J. Cass, G. Passucci, R. Surman, and A. Aprahamian, AIP Advances **4**, 041009 (2014).

[141] R. Surman, M. Mumpower, R. Sinclair, K. L. Jones, W. R. Hix, and G. C. McLaughlin, AIP Advances **4**, 041008 (2014).

[142] X. Roca-Maza, G. Colò, and H. Sagawa, Phys. Rev. C **86**, 031306 (2012).

[143] X. Roca-Maza, G. Colò, and H. Sagawa, Physica Scripta **2013**, 014011 (2013).

[144] M. Kortelainen, T. Lesinski, J. Moré, W. Nazarewicz, J. Sarich, N. Schunck, M. V. Stoitsov, and S. Wild, Phys. Rev. C **82**, 024313 (2010).

[145] P.-G. Reinhard, D. J. Dean, W. Nazarewicz, J. Dobaczewski, J. A. Maruhn, and M. R. Strayer, Phys. Rev. C **60**, 014316 (1999).

[146] P. Klüpfel, P.-G. Reinhard, T. J. Bürvenich, and J. A. Maruhn, Phys. Rev. C **79**, 034310 (2009).

[147] E. Chabanat, P. Bonche, P. Haensel, J. Meyer, and R. Schaeffer, Nuclear Physics A **635**, 231 (1998).

[148] J. D. McDonnell, private communication.

[149] M. Kortelainen, J. McDonnell, W. Nazarewicz, P.-G. Reinhard, J. Sarich, N. Schunck, M. V. Stoitsov, and S. M. Wild, Phys. Rev. C **85**, 024304 (2012).

[150] J. Engel, M. Bender, J. Dobaczewski, W. Nazarewicz, and R. Surman, Phys. Rev. C **60**, 014302 (1999).

[151] S. Fracasso and G. Colò, Phys. Rev. C **76**, 044307 (2007).

[152] M. Kortelainen, J. McDonnell, W. Nazarewicz, E. Olsen, P.-G. Reinhard, J. Sarich, N. Schunck, S. M. Wild, D. Davesne, J. Erler, and A. Pastore, Phys. Rev. C **89**, 054314 (2014).

[153] E. T. Balbuena, *Hartree-Fock-Bogoliubov Calculations for Nuclei Far from Stability*, Ph.D. thesis, Vanderbilt University, Nashville, TN (2003).

[154] J. Dobaczewski, P. Magierski, W. Nazarewicz, W. Satuła, and Z. Szymański, Phys. Rev. C **63**, 024308 (2001).

[155] W. Satuła, J. Dobaczewski, and W. Nazarewicz, Phys. Rev. Lett. **81**, 3599 (1998).

[156] G. Audi, M. Wang, A. Wapstra, F. Kondev, M. MacCormick, X. Xu, and B. Pfeiffer, Chinese Physics C **36**, 1287 (2012).

[157] M. Wang, G. Audi, A. Wapstra, F. Kondev, M. MacCormick, X. Xu, and B. Pfeiffer, Chinese Physics C **36**, 1603 (2012).

[158] G. Audi and A. Wapstra, Nuclear Physics A **595**, 409 (1995).

[159] M. V. Stoitsov, J. Dobaczewski, W. Nazarewicz, S. Pittel, and D. J. Dean, Phys. Rev. C **68**, 054312 (2003).

[160] P. Möller, J. Nix, and K.-L. Kratz, Atomic Data and Nuclear Data Tables **66**, 131 (1997).

[161] J. Suhonen, in *From Nucleons to Nucleus*, Theoretical and Mathematical Physics (Springer Berlin Heidelberg, 2007) pp. 157–204.

[162] Y. Engel, D. Brink, K. Goeke, S. Krieger, and D. Vautherin, Nuclear Physics A **249**, 215 (1975).

[163] H. Akimune, I. Daito, Y. Fujita, M. Fujiwara, M. B. Greenfield, M. N. Harakeh, T. Inomata, J. Jänecke, K. Katori, S. Nakayama, H. Sakai, Y. Sakemi, M. Tanaka, and M. Yosoi, Phys. Rev. C **52**, 604 (1995).

[164] C. J. Guess, T. Adachi, H. Akimune, A. Algora, S. M. Austin, D. Bazin, B. A. Brown, C. Caesar, J. M. Deaven, H. Ejiri, E. Estevez, D. Fang, A. Faessler, D. Frekers, H. Fujita, Y. Fujita, M. Fujiwara, G. F. Grinyer, M. N. Harakeh, K. Hatanaka, C. Herlitzius, K. Hirota, G. W. Hitt, D. Ishikawa, H. Matsubara, R. Meharchand, F. Molina, H. Okamura, H. J. Ong, G. Perdikakis, V. Rodin, B. Rubio, Y. Shimbara, G. Süsoy, T. Suzuki, A. Tamii, J. H. Thies, C. Tur, N. Verhanovitz, M. Yosoi, J. Yurkon, R. G. T. Zegers, and J. Zenihiro, Phys. Rev. C **83**, 064318 (2011).

[165] J. K. Tuli, "Nuclear Wallet Cards, National Nuclear Data Center," (accessed August 11, 2014).

[166] C. Gaarde, J. Rapaport, T. Taddeucci, C. Goodman, C. Foster, D. Bainum, C. Goulding, M. Greenfield, D. Hören, and E. Sugarbaker, Nuclear Physics A **369**, 258 (1981).

[167] Q. Zhi, E. Caurier, J. J. Cuenca-García, K. Langanke, G. Martínez-Pinedo, and K. Sieja, Phys. Rev. C **87**, 025803 (2013).

[168] "Evaluated Nuclear Structure Data File, April 16, 2014," `http://www.nndc.bnl.gov/ensarchivals/`.

[169] Z. Y. Xu, S. Nishimura, G. Lorusso, F. Browne, P. Doornenbal, G. Gey, H.-S. Jung, Z. Li, M. Niikura, P.-A. Söderström, T. Sumikama, J. Taprogge, Z. Vajta, H. Watanabe, J. Wu, A. Yagi, K. Yoshinaga, H. Baba, S. Franchoo, T. Isobe, P. R. John, I. Kojouharov, S. Kubono, N. Kurz, I. Matea, K. Matsui, D. Mengoni, P. Morfouace, D. R. Napoli, F. Naqvi, H. Nishibata, A. Odahara, E. Şahin, H. Sakurai, H. Schaffner, I. G. Stefan, D. Suzuki, R. Taniuchi, and V. Werner, Phys. Rev. Lett. **113**, 032505 (2014).

[170] T. Munson, J. Sarich, S. M. Wild, S. Benson, and L. Curfman McInnes, *TAO 3.6 Users Manual*, Technical Memorandum ANL/MCS-TM-322 (Argonne National Laboratory, Argonne, Illinois, 2015).

[171] C. Gaarde, J. Larsen, M. Harakeh, S. van der Werf, M. Igarashi, and A. Müller-Arnke, Nuclear Physics A **334**, 248 (1980).

[172] G. Colò, N. Van Giai, P. F. Bortignon, and R. A. Broglia, Phys. Rev. C **50**, 1496 (1994).

[173] J. D. Walecka, in *Muon Physics*, Vol. 2, edited by V. W. Hughes and C. S. Wu (Academic Press, 1975) Chap. 5, pp. 113–218.

[174] E. J. Konopinski, *The Theory of Beta Radioactivity*, edited by N. F. Mott, E. C. Bullard, and D. H. Wilkinson, The International Series of Monographs on Physics (Oxford University Press, 1966).

[175] P. J. Mohr, B. N. Taylor, and D. B. Newell, Rev. Mod. Phys. **84**, 1527 (2012).